SANDIA REPORT

SAND2005-1196
Unlimited Release
Printed April 2005

Development of Models and Online Diagnostic Monitors of the High-Temperature Corrosion of Refractories in Oxy/Fuel Glass Furnaces

Final Project Report

Mark D. Allendorf
Robert H. Nilson
Steven F. Rice
Stewart K. Griffiths
Peter M. Walsh
Nancy Yang
Benjamin Bugeat
M. Usman Ghani
Amul Gupta
Ovidiu Marin
George Pecoraro
Karl E. Spear
Ed Wolfe
Mariano Velez

Prepared by
Sandia National Laboratories
Albuquerque, New Mexico 87185 and Livermore, California 94550

Sandia is a multiprogram laboratory operated by Sandia Corporation,
a Lockheed Martin Company, for the United States Department of Energy's
National Nuclear Security Administration under Contract DE-AC04-94AL85000.

Sandia National Laboratories

Issued by Sandia National Laboratories, operated for the United States Department of Energy by Sandia Corporation.

Available to DOE and DOE contractors from

U.S. Department of Energy
Office of Scientific and Technical Information
P.O. Box 62
Oak Ridge, TN 37831

Telephone: (865)576-8401
Facsimile: (865)576-5728
E-Mail: reports@adonis.osti.gov
Online ordering: http://www.doe.gov/bridge

Available to the public from

U.S. Department of Commerce
National Technical Information Service
5285 Port Royal Rd
Springfield, VA 22161

Telephone: (800)553-6847
Facsimile: (703)605-6900
E-Mail: orders@ntis.fedworld.gov
Online order: http://www.ntis.gov/help/ordermethods.asp?loc=7-4-0#online

SAND2005-1196
Unlimited Release
Printed February 2005

Development of Models and Online Diagnostic Monitors of the High-Temperature Corrosion of Refractories in Oxy/Fuel Glass Furnaces

Final Project Report

Mark D. Allendorf
Robert H. Nilson
Steven F. Rice
Stewart K. Griffiths
Peter M. Walsh*
Nancy Yang
Sandia National Laboratories

Karl E. Spear†
Pennsylvania State University

Mariano Velez‡
University of Missouri, Rolla

Benjamin Bugeat
Ovidiu Marin
M. Usman Ghani
American Air Liquide

Amul Gupta
Monofrax, Inc.

Ed Wolfe
ANH Refractories

George Pecoraro†
PPG Industries, Inc.

Abstract

This report summarizes the results of a five-year effort to understand the mechanisms and develop models that predict the corrosion of refractories in oxygen-fuel glass-melting furnaces. Thermodynamic data for the Si-O-(Na or K) and Al-O-(Na or K) systems are reported, allowing equilibrium calculations to be performed to evaluate corrosion of silica- and alumina-based refractories under typical furnace operating conditions. A detailed analysis of processes contributing to corrosion is also presented. Using this analysis, a model of the corrosion process was developed and used to predict corrosion rates in an actual industrial glass furnace. The rate-limiting process is most likely the transport of NaOH(gas) through the mass-transport boundary layer from the furnace atmosphere to the crown surface. Corrosion rates predicted on this basis are in better agreement with observation than those produced by any other mechanism, although the absolute values are highly sensitive to the crown temperature and the NaOH(gas) concentration at equilibrium and at the edge of the boundary layer. Finally, the project explored the development of excimer laser induced fragmentation (ELIF) fluorescence spectroscopy for the detection of gas-phase alkali hydroxides (e.g., NaOH) that are predicted to be the key species causing accelerated corrosion in these furnaces. The development of ELIF and the construction of field-portable instrumentation for glass furnace applications are reported and the method is shown to be effective in industrial settings.

Acknowledgments

The authors wish to thank R. D. Moore and J. Neufeld (Gallo Glass Co., Modesto, CA) for generously providing detailed information concerning operating conditions and the design of the Tank 1 oxy-fuel furnace and Amul Gupta (Monofrax Inc., Falconer, NY) for conducting detailed laboratory corrosion tests and analysis. For their financial support, we are grateful to: the U.S. Dept. of Energy (DOE) Office of Industrial Technologies Program Glass Industry of the Future Team; American Air Liquide, BOC Gases, PPG Industries Inc., Praxair Inc., Techneglas, and Visteon Automotive Systems; and the DOE Environmental Management Science Program funded by the Office of Environmental Management's Office of Science and Technology, and administered jointly with the Office of Energy Research under contract DE-AC05-96OR22464 with Lockheed Martin Energy Research Corporation.

Table of Contents

Executive Summary

This report documents the results of work performed on a project entitled "Development of Models and Online Diagnostic Monitors of the High-Temperature Corrosion of Refractories in Oxy/Fuel Glass Furnaces." The project was funded by the U.S. Department of Energy (DOE), with industrial cost share, through the Industrial Technologies Program Industries of the Future (IOF) program. Partner institutions involved included PPG Industries, Inc., American Air Liquide, Visteon, Techneglass, BOC Gases, and Sandia National Laboratories.

The objectives of the project were to develop a better understanding of the mechanisms of enhanced refractory corrosion in oxy/fuel glass furnaces and to develop models to predict corrosion rates, identify operating regimes that minimize corrosion, and to define the attributes of improved refractories. Finally, lack of measurements of gas-phase hydroxides such as NaOH and KOH, which are key species in the corrosion of low-density silica, motivated a detailed investigation of a laser-based method to quantify the concentration of these species in furnace atmospheres. The project succeeded in all three areas, providing 1) a database of thermodynamic information essential to modeling refractory corrosion in glass furnaces; 2) a detailed analysis of the phenomena contributing to corrosion and a determination of the rate-limiting step; 3) an analytical model that predicts corrosion rates that are generally in good agreement with field observations; and 4) a first-generation diagnostic method for the detection of NaOH and KOH that was field tested in several glass-melting facilities.

The results of these efforts were made available to industry in the following ways. First, detailed reports of the research were provided on a quarterly basis to all project partners, who represent major glass manufacturers, the primary gas suppliers to the industry, refractory suppliers, and two key universities engaged in gas-related research. All results were shared freely with these partners. Second, per the requirements of the DOE sponsor, we presented a summary of the results at the annual program review, which was attended by a broad cross section of the industry. Third, thermodynamic data are available to the industry free of charge at the following web site: http://www.ca.sandia.gov/HiTempThermo/. Fourth, results of all phases of the project are described in peer-reviewed journals, portions of which are included in this report. Finally, a computer model that predicts silica corrosion rates is available by contacting the corresponding author of this report.*

We believe that the body of knowledge obtained in this project is the most comprehensive investigation of the corrosion phenomena to date and as such provides the information necessary for its inclusion in large computational fluid dynamics codes used to model glass furnaces, a number of which have been developed or are in use by gas suppliers and glass manufacturers. Furthermore, the thermodynamic data, in conjunction with additional data already available on the above web site, are provided in a format compatible with commercial equilibrium codes (in particular, ChemSage and FactSage), allowing refractory suppliers to assess the stability of their materials under furnace conditions without resorting to complex and expensive experiments.

* Mark Allendorf: mdallen@sandia.gov

CHAPTER 1

INTRODUCTION

Conventional glass-melting furnaces typically are constructed with a lining of silica refractory brick (Figure 1-1). Silica is particularly advantageous because it is inexpensive, low density (simplifying furnace construction), and has low thermal expansion. However, silica is susceptible to attack by alkali vapors that volatilize from the glass, and by airborne batch particles. In air-fired furnaces, the roof or "crown" typically lasts about ten years. Since the early 1990s when melting furnaces began to be converted to oxy-fuel technology, in which combustion air is replaced with pure oxygen, substantially higher silica corrosion rates have been observed, shortening furnace crown life by as much as a factor of two to three. Corrosion rates for crown refractories as high as 20 cm in a six-month period have been observed in some cases. In addition, the products of corrosion—solids or liquids—can fall or drip into the glass reservoir, introducing defects into the glass that reduce yields [Ref. 4 in Chap. 2] (Figures 1-2 and 1-3).

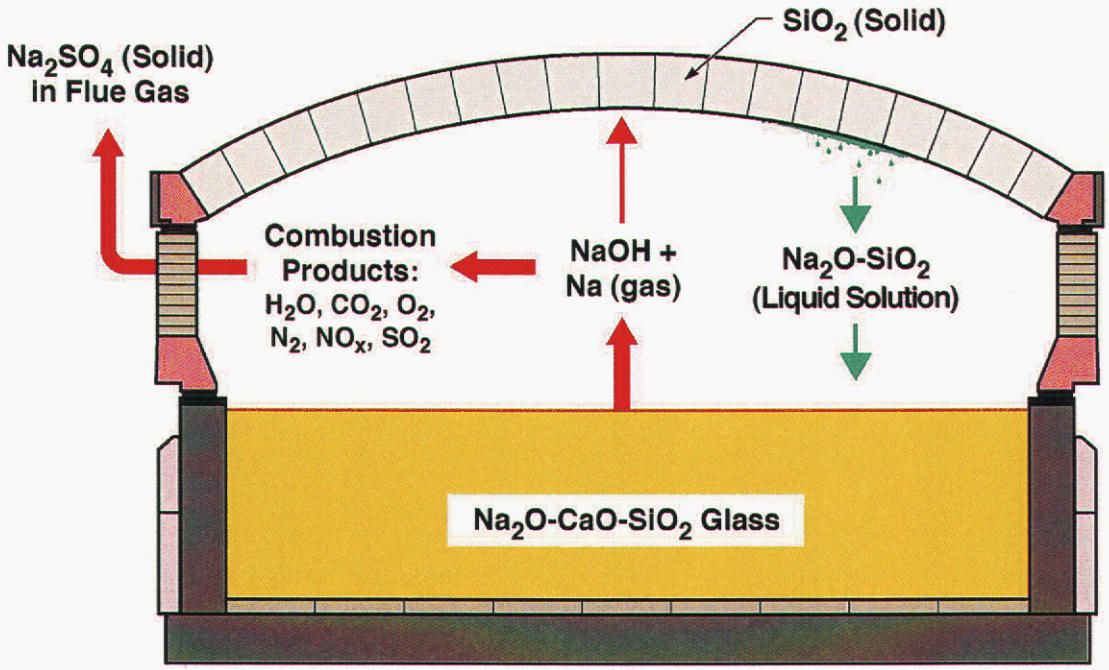

Figure 1-1. Schematic of the corrosion of silica crown refractory in an oxygen-fuel-fired glass melting furnace.

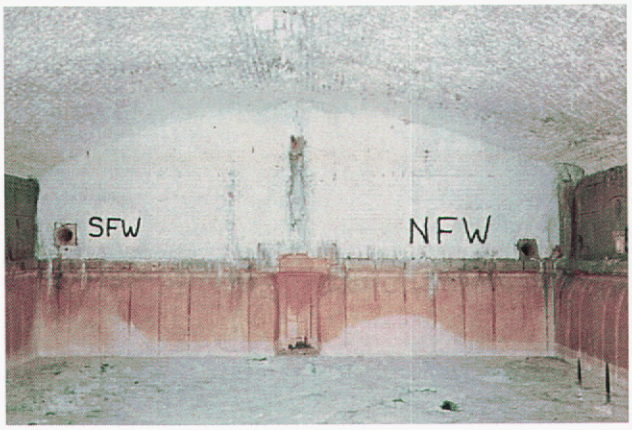

Figure 1-2. Interior of an oxygen-fuel float-glass furnace after just prior to a rebuild. The crown surface is covered with white material shown to be a sodium-silicate glass by off-line analysis.

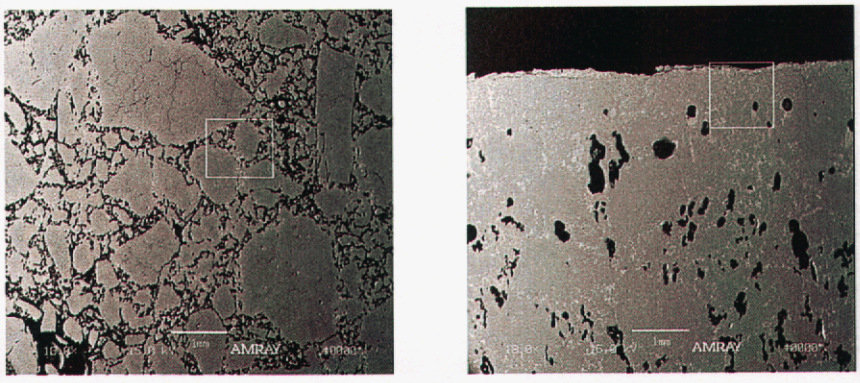

Figure 1-3. Monofrax oxy/fuel corrosion tests and post-mortem analysis show penetration by sodium. Dark areas represent pores surrounding the silica grains. Left: Unused low-density silica brick. Right: Sample exposed to ~600 ppm NaOH for 75 hours at 1610 °C.

Melting furnaces represent major capital investments for glass manufacturers. Rebuilding a float-glass furnace costs an estimated $10 million, including the costs of lost production. Due to high reconstruction costs and product quality concerns, there is considerable interest in understanding the mechanisms controlling corrosion so that either furnace conditions could be adjusted to reduce corrosion to acceptable rates, or alternative refractory materials that are more inert could be identified. Since oxy/fuel-fired glass furnaces have only been in use since 1991, there was limited prior research directed toward understanding and solving the problems of refractory corrosion. Few systematic investigations had been published describing corrosion mechanisms, and only simplified models had been developed to predict corrosion rates. While investigators speculated on the probable causes, no detailed description of the mechanisms of refractory corrosion was available in 1997 when the U.S. Department of Energy Industrial Technologies Program (DOE/ITP)[†] solicited proposals to address this issue.

[†] Then known as the Office of Industrial Technologies.

In September 1998 a multi-institution team led by PPG Industries and Sandia National Laboratories was awarded funding by DOE/ITP for a five-year effort to systematically investigate key aspects of refractory corrosion by measuring corrosion rates under controlled atmospheres, identifying mechanisms through characterization of samples taken from full-scale furnaces, determining transport properties through the refractory, and obtaining refractory temperatures and gas-phase species concentrations.

The project was conceived following a glass industry roadmapping workshop sponsored by DOE/ITP the previous year. In addition to funding from DOE, the project received financial support from PPG Industries, Visteon, Techneglass, American Air Liquide, BOC Gases, and Praxair. The research team consisted of:

Sandia National Laboratories

Dr. Mark Allendorf – principal investigator, Sandia team; Chemistry
Dr. Stewart Griffiths – Modeling
Mr. Russ Hanush – Diagnostics
Dr. Robert Nilson – Modeling
Dr. Steven Rice – Diagnostics
Dr. Nancy Yang – Electron microscopy

PPG Industries, Inc.

Dr. George Pecoraro –principal investigator, industry team; furnace-gas analysis

American Air Liquide

Dr. Ovidiu Marin – Furnace modeling using computational fluid dynamics
Dr. Benjamin Bugeat
Dr. Usman Ghani

Monofrax, Inc.

Dr. Amul Gupta – Corrosion testing; post-mortem analysis

NARCO/Harbison-Walker

Mr. Ed Wolfe – post-mortem analysis

Pennsylvania State University

Prof. Karl Spear – Thermodynamic calculations

University of Missouri, Rolla

Prof. Robert Moore – Corrosion testing
Prof. Mariano Velez – Corrosion testing

Prior to this project, limited investigations into refractory corrosion indicated that many factors beyond the chemical stability of the refractory determined corrosion rates in oxy/fuel furnaces.[‡] Thus, a comprehensive, generic understanding of the impact of each factor on the corrosion rate was needed before satisfactory long-term solutions could be developed for specific furnaces and environments. Such an understanding is a necessary precursor to the development of satisfactory long-term solutions for specific furnaces and environments. Differences in furnace design, operating conditions, and glass composition necessitate the development of individualized solutions. Given inputs such as crown temperature, refractory properties, and gas-phase composition, unique solutions for individual furnaces can then be obtained.

Thus, the primary objective of this project was to achieve a comprehensive understanding of the impact of the various factors on the corrosion rate of refractories in oxy/fuel furnaces. The project exploited the combined power of computer simulation and detailed materials characterization to construct analytical and computational models that could predict corrosion rates as a function of furnace conditions. Using these models, key factors in the corrosion process were identified, making it possible to identify furnace conditions and/or refractory compositions that correspond to reduced corrosion rates.

To accomplish this object, project efforts were focused on the following tasks:

Task 1. Characterization of corrosion processes – In this activity, the factors controlling the rate of refractory corrosion in glass furnaces were identified through a combination of experiments in controlled laboratory environments and characterization of corroded samples using sophisticated analytical techniques.

Task 2. Corrosion modeling - The goal of this project task was to develop, validate, and exercise one or more models that can predict corrosion rates as a function of refractory properties (chemical and structural) and furnace conditions. To validate model predictions, comparisons will be made with corrosion rates measured both in the laboratory and in realistic production environments. Models will then be used to identify furnace operating regimes prone to high corrosion rates and suggest refractory compositions and attributes (permeability, pore size, etc.) that may be more resistant to chemical attack.

Task 3. Online monitors for gas-phase alkali detection – The objective of this task was to explore the potential of laser-based detection methods for online process monitoring of gas-phase alkali concentrations (particularly NaOH and KOH) since this information will be essential to developing strategies for minimizing corrosion. These techniques would allow nearly instantaneous monitoring of the effects of process variables on alkali concentrations, which could significantly shorten the time required to optimize a given surface, as well as provide knowledge of the day-to-day variability of this quantity.

The research conducted through this project resulted in a number of published articles, which are included as chapters in this report:

[‡] See the Chapter 4 references.

Chapters 2 and 3 focus on the use of thermodynamic calculations to predict the stability of silica- (Chap. 2) and alumina-based (Chap. 3) refractories in air-fuel and oxy-fuel glass furnace environments. Equilibrium is generally considered a reasonable description of the chemical processes occurring on refractory surfaces because of the high temperatures involved (up to 1600 °C). Thus, thermodynamic calculations were used to predict the identity and concentration of gas-phase species in the atmosphere adjacent to the refractory and the products (solid, liquid, or gas) of corrosion. Chapter 2 contains the results of the equilibrium calculations for the Na_2O-SiO_2 and K_2O-SiO_2 systems, indicating that the principal product of the corrosion of SiO_2 refractories by gas-phase NaOH and KOH is a molten glass containing variable amounts of sodium or potassium.

Alumina-based ceramics, fused cast alumina-zirconia-silica, and fused mullite provide alternatives to silica refractories. However, these materials are also subject to varying degrees of corrosion in oxy/fuel environments. In Chapter 3, the high-temperature corrosion of Al_2O_3 refractories by MOH(g) (M = Na, K) found in the combustion atmospheres of typical air- and oxygen-fired glass-melting furnaces is examined using thermodynamic equilibrium calculations. The calculations, using newly generated data for sodium- and potassium-containing alumina phases, indicate that alumina is quite stable with respect to corrosion by MOH(g) under typical conditions in glass-melting furnaces. Problems associated with formation of liquid corrosion products, such as runoff of corrosion products into the melt and presumably, unacceptably high corrosion rates (as is the case for silica), should not be a problem for crowns constructed of either α- or β(Na)-alumina used in oxy-fuel melting furnaces. The negative aspects of using alumina refractories instead of silica is that they are heavier—requiring special construction for glass-melting furnaces—and more expensive.

Chapter 4 presents the first comprehensive analysis of the transport and chemical mechanisms that are potentially active in the corrosion of porous refractories used to line the crowns of glass-melting furnaces. While the work focuses on low-density silica refractories, the results can be extended to any refractory, assuming that a thermodynamic model is available to describe the chemical reaction between a gas-phase reactant, such as NaOH or KOH, and the refractory surface. Analytical models were used to evaluate the importance of four potential rate-limiting processes: 1) gas-phase transport of NaOH to the crown surface; 2) diffusion of sodium-containing reactants through a liquid product layer that forms on the brick face; 3) gas-phase diffusion of NaOH into refractory pores; and 4) chemical-kinetic limitations at the silica grain surface. Predictions were compared with reported corrosion rates and product compositions previously determined by post-mortem analysis of refractory samples. Researchers conclude that corrosion occurs largely by reaction and removal of material from the exposed brick face, rather than by transport of reactants into the porous bricks.

Chapter 5 summarizes the results of efforts to develop an online diagnostic technique for monitoring the sodium content in a glass melt tank atmosphere. The method is based on excimer laser-induced fluorescence (ELIF), a version of photofragmentation fluorescence (PFF) that uses the high-energy ultraviolet light from an excimer laser. Researchers report the development of a measurement method and the design and implementation of an apparatus that can measure the concentration of NaOH in the vapor phase of an oxygen-fuel glass furnace in nearly real-time. Until recently, direct quantitative measurements of sodium levels have been limited to extractive sampling methods followed by laboratory analysis. ELIF fluorescence spectroscopy permits the measurement of volatilized NaOH in high-temperature environments in less than one second.

CHAPTER 2[†]

THERMODYNAMIC ANALYSIS OF SILICA REFRACTORY CORROSION IN GLASS-MELTING FURNACES[†]

Abstract

Corrosion of refractory silica brick used to line the roof or "crown" of many-glass-melting furnaces is a serious problem in furnaces using oxygen-fuel rather than air-fuel mixtures. In this work, we report equilibrium calculations that support a corrosion mechanism in which alkali hydroxide gas (NaOH or KOH), produced by reaction of water vapor in the combustion gas with the molten glass, reacts with the silica brick in the furnace crown to produce an alkali silicate liquid with a composition that depends on the temperature of the crown. Our reported calculations predict the variable-composition liquid-solution corrosion product phase as a function of key furnace variables. Critical thermodynamic data needed for the liquid corrosion product-were generated using a modified associate species solution model and critical analysis of thermochemical information found in the literature for the Na_2O-SiO_2 and K_2O-SiO_2 systems. Excellent agreement with reported Na_2O-SiO_2 and K_2O-SiO_2 phase diagrams and with experimentally measured activities for Na_2O and K_2O is achieved. The results of our current calculations are for temperatures between 1273 and 1973 K (1000–1700 °C) under either air-fired or oxy-fired conditions, and are used to define a "critical temperature," above which corrosion is not expected to occur for a given NaOH(g) or KOH(g) partial pressure.

Introduction

The high cost of rebuilding refractory brick furnaces is driving organized efforts to determine the factors controlling corrosion, so that either furnace conditions can be adjusted to reduce corrosion to acceptable rates, or alternative refractory materials that are more inert can be identified. The former solution is preferable since silica brick is attractive because of its low density (which simplifies furnace construction), low thermal conductivity, and low cost.

A major component of many glasses is sodium oxide (Na_2O), which in the presence of combustion-generated water vapor forms gas-phase sodium hydroxide (NaOH). Some glasses, such as those used to make television tubes and lead "crystal" tableware, also contain high concentrations of potassium oxide (K_2O), which reacts with water vapor to form potassium hydroxide (KOH). Reaction of these hydroxide gases with the silica brick in the furnace crown to produce an alkali silicate liquid is assumed to be the corrosion mechanism (Figure 2-1), based on post-mortem analysis of refractory samples.[2,3] Experimental concentrations of NaOH(g) in oxy-fuel furnaces are reported to be as much three to four times higher than in air-fired furnaces[2] Both temperature[4] and gas velocity[5] also appear to play important roles. Since the temperatures

---

[†] This chapter was originally published as M. D. Allendorf, K. E. Spear "Thermodynamic Analysis of Refractory Corrosion in Glass Melting Furnaces," *J. Electrochem. Soc.*, **148**, B59 (2001) and was edited for this report.

of the silica refractory are typically quite high, ranging from more than 1600 °C at the surface exposed to the furnace to above 1100 °C on the exterior side of an insulated crown, equilibrium represents a reasonable description of the chemical behavior of the corrosion processes. Thus, thermodynamic calculations that predict equilibrium chemical compositions can play a useful role by identifying energetically stable species and by predicting the limiting extent of corrosion and corrosion products.

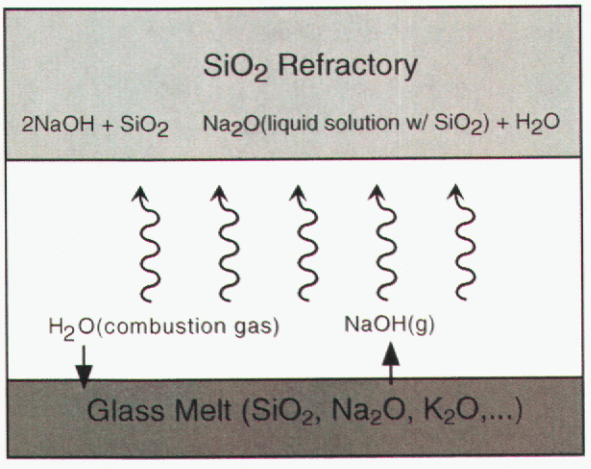

Figure 2-1. Schematic of the chemical processes involved in the corrosion of silica refractory by NaOH(g).

Previous investigators have used calculations of equilibria in the Na_2O-SiO_2[4,6,7] and K_2O-SiO_2[6] systems to identify gas-phase species present in furnace atmospheres and to examine the dependence of the SiO_2 corrosion by alkali hydroxides on refractory temperature, NaOH(g) concentration, and water vapor concentration. However, these calculations did not consider the formation of any variable-composition liquid-silicate phases. As a result, there may be systematic errors in the conclusions deduced from these previous results.

The accuracy of a thermodynamic calculation depends, of course, on the quality and completeness of the data employed. Unfortunately, the M_2O-SiO_2 systems are quite complex and very high deviations from Raoult's law are observed with the use of typical liquid solution models. Methods that attempt to model non-ideal solution behavior are needed to determine accurate thermodynamic functions for the low-melting glass that are the typical products of silica corrosion by alkali-containing species. The thermodynamics of the sodium oxide/silica system have been extensively studied due to their importance in a variety of fields; two recent investigations by Wu *et al.*[8] and Zaitsev *et al.*[9] provide the latest experimental data for these systems as well as a review of the relevant literature. Wu *et al.* fit the Na_2O-SiO_2 and K_2O-SiO_2 phase diagrams using their "quasi-chemical" model of the liquid phase to obtain the activities of Na_2O and K_2O in melts with SiO_2; the results are in good agreement with experiment. Zaitsev *et al.* used Knudsen effusion mass spectrometry to determine Na_2O and SiO_2 activities in the melt as a function of composition and temperature, as well as thermodynamic functions for the Na_2O-SiO_2 melt and of solid silicates at high-temperature. These investigators also provide a thorough comparison of their results with the available data in the literature for this system.

In this chapter, we discuss the use of a modified associate species model[10] to describe the thermodynamic functions for the liquid phases in the Na_2O-SiO_2 and K_2O-SiO_2 systems. We then use these data to calculate the equilibrium between silica and typical air- and oxy-fuel-fired glass-melting atmospheres. These are the first calculations to assess the impact of the formation of sodium- or potassium-silicate glasses on the corrosion of silica. The corrosion results reported here include: (a) the temperature dependence of gas-phase alkali-containing species concentrations in equilibrium with a liquid corrosion product and crystalline SiO_2; (b) the composition of the corrosion products and their temperature dependence; and (c) the predicted refractory temperature and MOH furnace concentration regimes in which corrosion of silica is expected to occur. Finally, we use these results to suggest mechanisms that may be active in the corrosion process. A preliminary report of our work on the corrosion of silica refractories by sodium-containing species was given in a proceedings volume.[11] However, a more thorough analysis and listing of the thermodynamic data for the Na_2O-SiO_2 system, including the liquid Na_2O-SiO_2 phase, and refined predictive results for the silica refractory corrosion are reported in this chapter.

Corrosion Mechanisms, Thermodynamic Data, and Modeling Approach

Corrosion reactions. Previous calculations[6,11] as well as those reported here show that NaOH(g) and KOH(g) are the most abundant gaseous species containing alkali metals at equilibrium between combustion atmospheres and sodium- or potassium-containing glass melts. Therefore, we assume in these calculations that MOH(g) is the key alkali-containing species participating in the corrosion of silica. Its formation can be described by the following chemical reaction:

$$M_2O(\text{in glass melt}) + H_2O(\text{g, combustion gas}) \leftrightarrow 2MOH(g),\ M = Na \text{ or } K \qquad (2\text{-}1)$$

At the surface of the refractory, a second reaction occurs to form a silica-rich liquid solution in which M_2O is dissolved:

$$2MOH(\text{gas}) \leftrightarrow M_2O(\text{dissolved in liquid } SiO_2) + H_2O(\text{g, combustion gas}) \qquad (2\text{-}2)$$

The liquid SiO_2 solution in Reaction 2-2 is in equilibrium with crystalline SiO_2 (cristobalite above ~1470 °C). This liquid solution composition is fixed by the temperature of the liquid – SiO_2(crystalline) equilibrium shown at high temperatures in the SiO_2-rich regions of the binary M_2O-SiO_2 phase diagrams discussed below. The fixed composition at a given temperature translates to a fixed activity of M_2O in the liquid solution at this temperature. Since the partial pressure of water is determined by the furnace atmosphere (mostly the combustion equilibria), and $K_{eq}(2)$ is a constant at a given temperature, only one partial pressure of MOH(g) can exist in equilibrium with the silica refractory and its liquid corrosion product at the temperature of the refractory surface. If the partial pressure of MOH(g) produced by Reaction 2-1 is smaller than the equilibrium value for 2-2, no corrosion will occur; conversely if the partial pressure of MOH (g) from Reaction 2-1 is larger than that at equilibrium for Reaction 2-2, this latter reaction is driven to the right and corrosion occurs. Therefore, to model the above corrosion reactions at equilibrium requires knowledge of the partial pressure of H_2O (g) (p_{H2O}) in the combustion atmosphere and the activity of M_2O (a_{M2O}) as a function of temperature and composition in the SiO_2-rich liquid that is in equilibrium with crystalline SiO_2. The equilibrium constants K_{eq} for Reactions 2-1 and 2-2 as a function of temperature are also needed, but note that $K_{eq}(1) = [1/K_{eq}(2)]$.

Computational approach to equilibrium modeling of the furnace-gas/refractory interaction. Although the equilibrium temperature of the combustion gases could be predicted by performing an equilibrium calculation under the constraints of constant enthalpy and pressure, the adiabatic flame temperature thus obtained is not an accurate reflection of the true furnace-gas temperature. This is due to the fact that heat losses in the furnace, which are difficult to predict, play a critical role in determining the actual temperature of the combustion gases. Consequently, we performed our calculations under the constraints of constant temperature and pressure. A range of temperatures was used (1200–2000 K) that could be encountered by the refractory. All calculations were performed for a total pressure of 1 bar. Recall that, while temperatures at the refractory surface may be quite high (~1900 K), large temperature gradients, amounting to hundreds of degrees over a distance of roughly 30 cm, can exist within the silica brick (see Introduction). Since these refractories are porous (~20–25% is typical), combustion gases can permeate the brick and encounter substantially lower temperatures. The partial pressure of H_2O in the combustion gas, p_{H2O}, which plays a key role in the corrosion process (Reactions 2-1 and 2-2), is thus (primarily) determined by the input fuel/oxygen ratio used in the calculations. The input compositions used are given in Table 2-1.

Table 2-1. Typical input conditions for equilibrium calculations.
P(total) = 1 bar, T = 1200 – 2000 K (927–1727 °C)

	$n(CH_4)^a$	$n(O_2)^a$	$N(N_2)^a$	$n(M_2O)^{a,c}$	$a(SiO_2)^b$
Calculation of p_{H2O}					
air-fired fuel mixture	1.00	2.05	8.2	--	--
oxy-fired fuel mixture	1.00	2.05	--	--	--
Corrosion predictions					
air-fired fuel mixture	1.00	2.05	8.2	0.1	1.0
oxy-fired fuel mixture	1.00	2.05	--	0.1	1.0

[a] Moles.
[b] Activity of SiO_2(crystalline) was fixed at unity.
[c] M = Na or K.

Thermodynamic data. To be able to predict the corrosion of crystalline silica, reliable high-temperature thermodynamic and phase-equilibria data are required for all critical species and phases in the M_2O–SiO_2–H_2O system. These data are available for most of the combustion gases involved, although the range in reported values for the heat of formation for NaOH is relatively large, as is discussed below. Table 2-2 provides a listing of major species used in the calculations, and their sources of thermodynamic data. Tabulated data for liquid-phase corrosion products are lacking, so these values were determined as part of an assessment and optimization of the values for all liquid and crystalline phases in the M_2O-SiO_2 binary systems. The computer program ChemSage™[12,13] was the primary tool used for developing an assessed, internally consistent thermodynamic database for the Na_2O-SiO_2 and K_2O-SiO_2 systems, and for performing subsequent calculations of the high-temperature corrosion reactions between MOH(g) and SiO_2(s). The following paragraphs describe our analysis of the available data for this system and the choices made for the values used in the equilibrium calculations described later in the paper.

Table 2-2. Major species used in calculations and sources of thermodynamic data.

Gas-phase[a]					
N_2	N_2O	NO	NO_2	O_2	H_2
H	OH	H_2O	CH_4	CO	CO_2
NH_3	HCN	SiO_2	SiO		
Na	NaOH[b]	K	KOH		
Liquid phase[c]					
Na_2O(l)	(2/5)Na_4SiO_4	(2/3)Na_2SiO_3	(1/2)$Na_2Si_2O_5$	Si_2O_4	
K_2O(l)	(2/3)K_2SiO_3	(1/2)$K_2Si_2O_5$	(1/3)$K_2Si_4O_9$		
Solid phases[c]					
SiO_2(cristobalite)	SiO_2(tridymite)	SiO_2 (quartz)			
Na_2O	Na_4SiO_4	$Na_6Si_2O_7$	Na_2SiO_3	$Na_2Si_2O_5$	$Na_6Si_8O_{19}$
K_2O	K_2SiO_3	$K_2Si_2O_5$	$K_2Si_4O_9$		

[a] A total of 75 species were initially used in these calculations. The major source of their thermodynamic data was *SGTE* (Ref. 12) except as noted.

[b] Thermodynamic data from *JANAF* (Ref. 13).

[c] The source of thermodynamic data for the listed liquid and solid species was assessments of the type described in Ref. 10; values for these species are listed in Table 2-4. A total of 15 fixed composition solid phases were initially included in our datafile, but only the above phases were of importance for the present study.

The required thermodynamic data for most gas-phase species were obtained from the assessed SGTE database.[14] However, the $\Delta H^\circ_{f,298}$ value for NaOH(g) in this database (-185.649 kJ/mol) is quite different from that found in the *JANAF Thermochemical Tables* (-197.757 kJ/mol),[15] although the corresponding values of the entropy (S°_{298}) from the two sources are quite similar (228.589 and 228.443 J/mol-K, respectively). The $\Delta H^\circ_{f,298}$ and S°_{298} values for the solid, NaOH(s), from the two sources are essentially the same. Thus, the 12 kJ/mol difference in the $\Delta H^\circ_{f,298}$ values for the vapor species appears to be the only major uncertainty in the sodium hydroxide data used in our calculations. Communications with the Russian group responsible for the IVANTHERMO database (Gorokhov *et al.*)[16] revealed that their experimental mass-spectrometric measurements of NaOH vapor pressures yield a $\Delta H^\circ_{f,298}$ of -189.7 ± 4 kJ/mol. The IVANTHERMO Database[17] has assessed this value to be -191.0 ± 8 kJ/mol. Both of these values lie between the SGTE and JANAF values. In the calculations described here, we use the *JANAF* value for $\Delta H^\circ_{f,298}$(NaOH,g). However, the effect of the difference in the SGTE and *JANAF* values in predicting the critical boundary lines that separate corrosive from non-corrosive conditions for air-fired and oxygen-fired furnaces is included and discussed later in Figure 2-9.

The thermodynamic data for the binary Na_2O-SiO_2 and K_2O-SiO_2 systems, including their liquid phases, were assessed and optimized by performing a "CALPHAD-type thermodynamic fitting" of the binary equilibrium phase diagrams for these systems. As described previously,[10] this procedure provides a means of testing and generating a set of self-consistent thermodynamic information for a system, including the generation of thermodynamic data for the oxide liquid phase. Data for the phase diagrams such as phase formation, melting points, eutectic compositions, and liquidus curves were obtained from various sources (primarily from *Phase Diagrams for Ceramists*,[18] Wu *et al.*,[8] and Zaitsev *et al.*[9]; the latter two papers provide an extensive critical assessment of the available data). Experimental activity data for M_2O(l) in the M_2O-SiO_2 liquid phases for M = Na[8,9,19-23] and M = K[8,24-26] are available from a wide range of sources and will be compared with calculated values in the results section of this paper.

Accurate values of the thermodynamic data for liquid-oxide solutions are of critical importance to our thermodynamic description of the M_2O-containing liquid corrosion product. To obtain these values, we described the liquid using a modified associate species model that has been previously discussed.[10] This model uses intermediate "liquid chemical species" with their corresponding thermodynamic data to represent the negative free-energy terms caused by nonideal mixing of the end-member components in a system. For example, in the Na_2O-SiO_2 binary system, the liquid is composed of "liquid species" Na_2O, (2/5)Na_4SiO_4, (2/3)Na_2SiO_3, (1/2)$Na_2Si_2O_5$, and Si_2O_4. Table 2-2 provides a complete listing of associate species used in the current calculations. To provide equal weighting to all liquid associate species, each species contains a total of two non-oxygen atoms in its formula. While these liquid species may not exist as chemical entities that can be isolated and characterized, they can accurately represent the negative interaction energies that occur between M_2O and SiO_2 at specific compositions in this liquid oxide solution. Positive interactions (repulsion terms ultimately leading to phase separation in solutions) cannot be modeled using the standard associate species model. Instead, we use positive interaction parameters between pairs of associate species that compositionally bound the region of phase separation (immiscibility gap).[10] In the two chemical systems of interest in this paper, these respective pairs of species are (1/2)$Na_2Si_2O_5$ and Si_2O_4, and (1/3)$K_2Si_4O_9$ and Si_2O_4. A composition-dependent regular solution constant is used in representing the excess free energy. The excess free energy equations and constants for these two interactions are given in Table 2-3. These equations accurately model the liquid thermodynamics in the composition region in which a metastable immiscibility gap has been reported for glass phases in these systems (see the lower right portions of the phase diagrams in Figures 2-2 and 2-4). The thermodynamic data for the system was optimized to achieve the best overall agreement with the most accurate experimental information reported for: (a) each phase; (b) the phase diagram; and (c) experimentally measured activities for Na_2O and K_2O dissolved in liquid silica.

Table 2-3. Excess free energy equations representing the positive interaction terms between pairs of liquid associate species in liquid solutions. A Redlich-Kister expansion of a regular solution constant is used.

$Na_2Si_2O_5(1/2)$ - $Si_2O_4(l)$	$\Delta G^{exs} = X\,(1\text{-}X)\,\{10{,}000 - 11{,}400(1\text{-}2X)\}$ (J/mol of liquid species)
$K_2Si_4O_9(1/3)$ - $Si_2O_4(l)$	$\Delta G^{exs} = X\,(1\text{-}X)\,\{14{,}000 - 3{,}800(1\text{-}2X)\}$ (J/mol of liquid species)

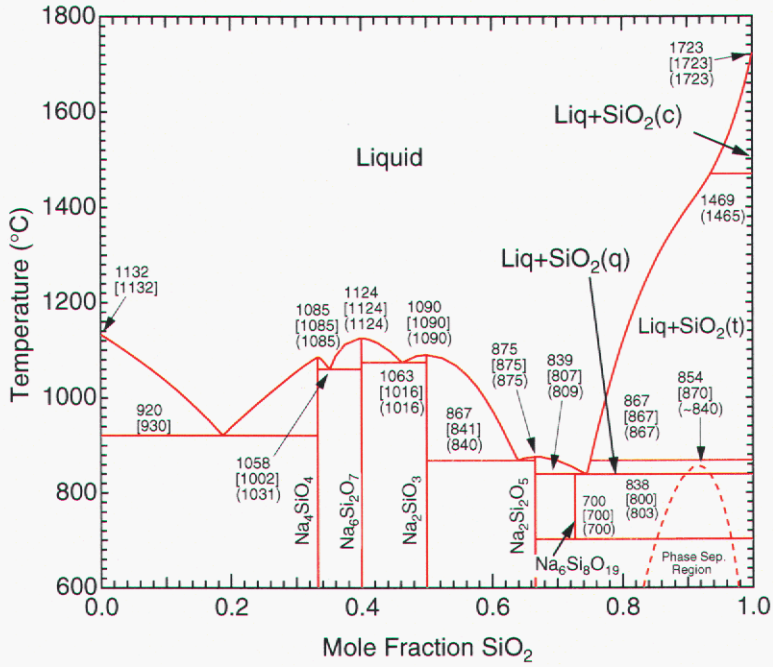

Figure 2-2. Calculated phase diagram for the Na_2O-SiO_2 system. Current temperatures are shown, along with previously reported values in parentheses (ref. 7) and brackets (ref. 8).

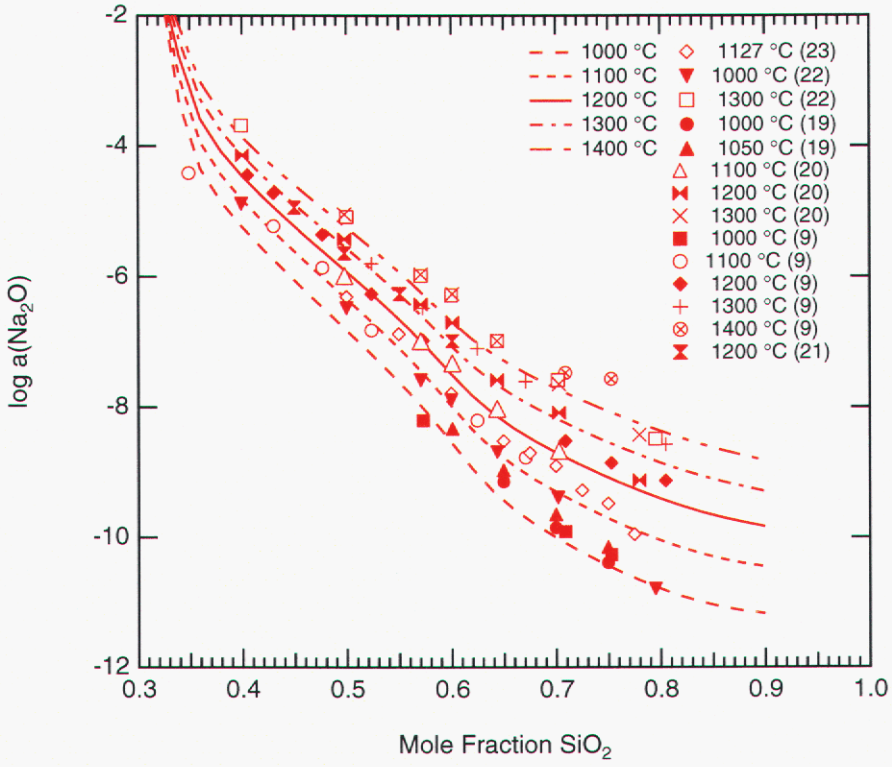

Figure 2-3. Calculated and measured (ref. 7,8,18-22) Na_2O activities in Na_2O-SiO_2 liquid (glass) solutions.

The set of thermodynamic data we used for all condensed species and the important gas-phase species in the Na_2O-SiO_2 and K_2O-SiO_2 systems are listed in Table 2-4. The data in this table are in a form directly usable by ChemSage, and were used to calculate the phase diagrams shown in Figures 2-2 and 2-4*, and the activity plots shown in Figures 2-3 and 2-5. These data include $\Delta H^{\circ}_{f,298}$ and S°_{298} values, along with Cp equations for various temperature ranges, and enthalpies of phase transformations when appropriate. Enthalpies of fusion are not listed separately since these numbers are incorporated in the relative enthalpies of formation of liquid and solid phases. The positive interaction parameters for the pairs of liquid species bounding metastable liquid immiscibility gaps are also given in this table in the form of excess free energies of solution. The agreement with reported information and our calculated diagrams and activities is quite good, as is discussed below.

Table 2-4. Thermodynamic data for important species in Na_2O-SiO_2 and K_2O-SiO_2 systems.

species	$\Delta H^\circ_{f,298}$ (J/mol)	S°_{298} (J/mol-K)	T(K)	$C_p = a + b \cdot T + c \cdot T^2 + d/T^2$ (J/mol-K)			
				a	$b \cdot 10^3$	$c \cdot 10^6$	$d \cdot 10^{-5}$
gases							
Na	107,500	153.716	2700	21.025	-0.384	0.143	-0.134
			4700	61.372	0.445	-0.052	-31.192
NaOH[a]	-197,757	228.443	1500	51.971	2.281	0.778	-3.848
			6000	58.196	1.315	-0.115	-66.087
K	89,000	160.339	2100	21.136	-0.653	0.293	–0.017
			4500	16.475	-0.366	0.709	9.801
KOH	-232,630	236.376	1200	53.038	-0.004	2.094	-4.168
			3200	52.639	4.546	-0.614	-20.879
liquid associates							
Na_2O(l)	-370,284	108.989	1023	55.480	70.210	-30.540	-4.140
	ΔH°_{trans}(1023K) = 1,757		1243	82.563	12.350	0	0
	ΔH°_{trans}(1243K) = 11,924		1405	82.563	12.350	0	0
			3500	104.600	0	0	0
Na_4SiO_4(2/5)	-785,540	117.004	1000	73.036	56.920	-24.436	-18.936
			1393	94.702	10.632	0	-15.624
			3000	112.332	0.752	0	-15.624
Na_2SiO_3(2/3)	-980,800	116.366	1000	84.740	48.060	-20.360	-28.800
			1363	102.795	9.487	0	-26.040
			3000	117.487	1.253	0	-26.040
$Na_2Si_2O_5$(/2)	-1,199,000	113.875	1147	99.370	36.985	-15.270	-41.130
			3000	123.930	1.880	0	-39.060
K_2O(l)	-327,300	129.959	1013	75.947	17.146	0	-5.196
			3000	100.000	0	0	0
K_2SiO_3(2/3)	-997,100	123.100	1249	98.385	12.684	0	-29.984
			3000	114.420	1.253	0	-26.040
$K_2Si_2O_5$(/2)	-1,220,370	117.100	1319	109.604	10.453	0	-42.018
			3000	121.630	1.880	0	-39.060
$K_2Si_4O_9$(/3)	-1,425,750	106.300	1043	120.822	8.222	0	-54.052
			3000	128.840	2.507	0	-52.080
Si_2O_4(l)	-1,793,592	101.658	1996	143.260	3.760	0	-78.120
			3000	171.544	0	0	0

Table 2-4 (cont.): Thermodynamic data for important species in Na_2O-SiO_2 and K_2O-SiO_2 systems.

species	$\Delta H^\circ_{f,298}$ (J/mol)	S°_{298} (J/mol-K)	T(K)	$C_p = a + b \cdot T + c \cdot T^2 + d/T^2$ (J/mol-K)			
				a	$b \cdot 10^3$	$c \cdot 10^6$	$d \cdot 10^{-5}$
crystalline solids							
Na_2O	-417,982	75.040	1023	55.480	70.210	-30.540	-4.140
	-417,982[b]	*75.061*[b]					
	$\Delta H^\circ_{trans(1023K)}$ = 1,757		1243	82.563	12.350	0	0
	$\Delta H^\circ_{trans(1243K)}$ = 11,924		2500	82.563	12.350	0	0
Na_4SiO_4	-2,095,630	195.811	1000	182.590	142.300	-61.080	-47.340
	-2,101,297	*195.811*	1393	236.756	26.580	0	-39.060
			3000	280.830	1.880	0	-39.060
$Na_6Si_2O_7$	-3,676,200	317.000	1000	309.700	214.390	-91.620	-90.540
	-3,596,080	*360.826*	1363	390.949	40.810	0	-78.120
			3000	457.060	3.760	0	-78.120
Na_2SiO_3	-1,555,500	119.000	1000	127.110	72.090	-30.540	-43.200
	-1,558,601	*113.846*	1363	154.193	14.230	0	-39.060
			3000	176.230	1.880	0	-39.060
$Na_2Si_2O_5$	-2,475,200	165.000	1147	198.740	73.970	-30.540	-82.260
	-2,470,340	*164.055*	3000	247.860	3.760	0	-78.120
$Na_6Si_8O_{19}$	-9,241,573	585.000	1147	739.480	225.670	-91.620	-324.900
	-9,167,917	*652.863*	3000	886.84	15.040	0	-312.480
K_2O	-361,700	96.000	1013	75.947	17.1460	0	-5.196
	-361,498	*102.006*	3000	100.000	0	0	0
K_2SiO_3	-1,544,000	146.000	1249	147.577	19.0260	0	-44.976
	-1,560,362	*146.147*	3000	171.630	1.8800	0	-39.060
$K_2Si_2O_5$	-2,509,000	191.000	1319	219.207	20.906	0	-84.036
	-2,522,542	*182.004*	3000	243.260	3.760	0	-78.120
$K_2Si_4O_9$	-4,327,000	282.000	1043	362.467	24.6660	0	-162.156
	-4,338,562	*265.684*	3000	386.520	7.5200	0	-156.240
SiO_2(cris)	-906,377	46.029	1996	71.630	1.880	0	-39.060
	-906,377	*46.029*	3000	85.772	0	0	0
SiO_2(trid)	-907,257	45.524	1996	71.630	1.880	0	-39.060
	-907,045	*45.524*	3000	85.772	0	0	0
SiO_2(quar)	-908,758	44.207	1996	71.630	1.880	0	-39.060
	-908,627	*44.207*	3000	85.772	0	0	0

[a] Data from JANAF Tables,[15] see text for discussion of uncertainties in NaOH(g) data.
[b] Values for $\Delta H^\circ_{f,298}$ and S°_{298} in *italics* are from Wu *et al.*[8]

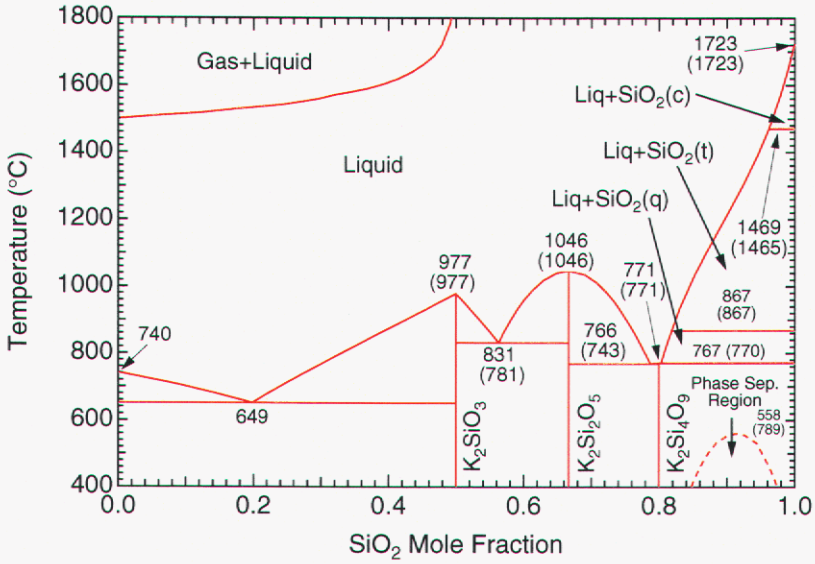

Figure 2-4. Calculated phase diagram for the K_2O-SiO_2 system. Current temperatures are shown, along with previously reported values in parentheses: (ref. 7).

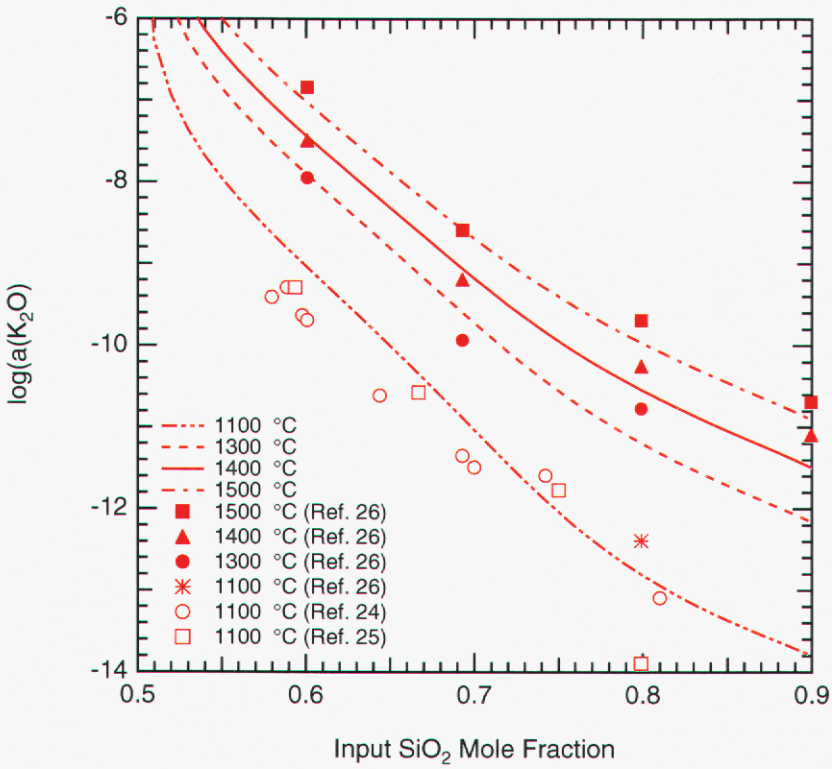

Figure 2-5. Calcuted and measured (ref. 7) K_2O activities in K_2O-SiO_2 liquid (glass) solutions.

Modeling the M_2O-SiO_2 phase diagram and M_2O activities. To model the corrosion of silica refractories, we first determined thermodynamic data given in Table 2-4 for sodium-containing and potassium-containing silica-rich liquid phases that exist in equilibrium with crystalline silica. These liquids are the expected products of silica corrosion by NaOH(g) and KOH(g). We used the above-mentioned modified associate species model to represent the liquid solution thermodynamic behavior. The results of these calculations are shown in the form of a phase diagram for the Na_2O-SiO_2 system[§] in Figure 2-2, and for the K_2O-SiO_2 system[§] in Figure 2-4.

Predicted melting points and eutectic compositions are given in each figure; numbers in parenthesis[8] and square brackets[9] correspond to reported values. The Na_2O-SiO_2 diagram is in good agreement with the experimental and assessed phase diagram for the well-established crystalline phases of Na_4SiO_4, Na_6SiO_7, Na_2SiO_3, $Na_2Si_2O_5$, $Na_6Si_8O_{19}$ and given by Wu *et al.*,[8] and Zaitsev *et al.*[9] The calculated phase diagram for the K_2O-SiO_2 system given in Figure 2-4 agrees well with the critically assessed diagram given by Wu *et al.*[8]

The important portions of these diagrams for this corrosion study are the two-phase regions in which crystalline silica (either cristobalite or tridymite) is in equilibrium with a liquid of composition $[(M_2O)_{1-x}(SiO_2)_x$, where $X(SiO_2) \geq 0.8]$. The thermodynamic data for the SiO_2-rich liquids in the two alkali systems predict the observed metastable liquid phase separations (immiscibilities) that occur for $X(SiO_2) > 0.8$ portion of the diagrams at temperatures below about 855 °C for the Na_2O-SiO_2 system, and at temperatures below about 558 °C for the K_2O-SiO_2 system. Calculated phase transition temperatures for SiO_2(s) using the data in Table 2-3 also agree well with reported values.

As shown in Figures 2-3 and 2-5, our use of the modified associate species model for the liquid phase (glass), and our assessed thermodynamic properties for this phase are in good agreement with measured values of the activities of M_2O (a_{M2O}) dissolved in liquid silica (M = Na or K). Significant scatter exists in the reported values, but this is not unexpected considering the difficulty in making such measurements on well-characterized samples at well-defined temperatures. The combined agreement of our calculated and reported activity values, and our calculated and reported binary phase diagrams for the two M_2O-SiO_2 systems provides a stringent test of the relative accuracy and internal consistency of the sets of thermodynamic data given in Table 2-4.

[§] Temperatures in these figures are given in °C for ease of comparison with the referenced phase diagrams in the literature. Units of K are used in the remainder of the discussion.

Corrosion Analysis, Predictions, and Discussion: Equilibrium predictions of silica corrosion by Na- or K-containing species

The phase diagrams for the Na_2O-SiO_2 and K_2O-SiO_2 systems in Figure 2-2 and 2-4, respectively, reveal that at the temperatures in the glass melting furnaces, crystalline silica in the refractory can react with Na- or K-containing species to produce an equilibrium product consisting of a silica-rich liquid containing dissolved Na_2O or K_2O. Although crystalline alkali silicates are included in the calculations (Table 2-2), none are predicted to form in the temperature range of the glass furnaces. Figure 2-6 shows that the respective Na_2O and K_2O mole fraction (X_{M2O}) in the liquid corrosion product decreases from values greater than 0.15 at 1200 K and lower down to zero at the 1996 K, the melting point of cristobalite. This changing M_2O concentration with temperature in liquids that equilibrate with crystalline SiO_2 has two important consequences for the development of corrosion mechanisms. First, the minimum partial pressures of MOH(g) that can cause corrosion depend on the activity of M_2O in the liquid corrosion product (and thus the composition of this liquid). Second, it is known that increasing M_2O concentrations in the liquid corrosion product reduce the viscosity of alkali silicate melts.[27,28]

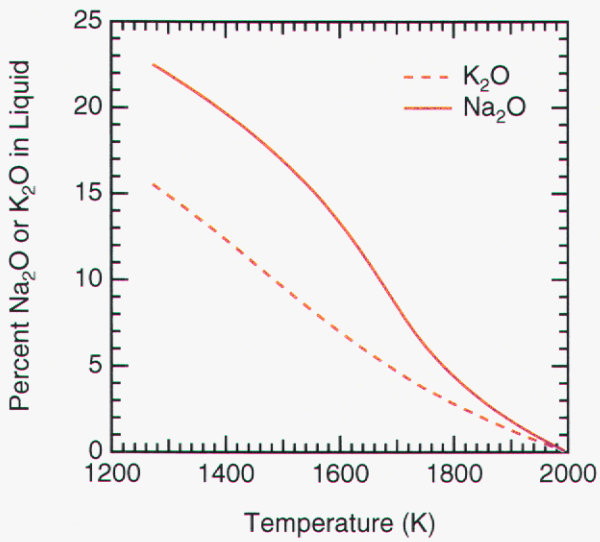

Figure 2-6. Percent Na_2O and percent K_2O in these respective liquid corrosion products as a function of temperature. Crystalling SiO_2 is in equilibrium with these liquids.

Selected results of equilibrium calculations for two typical combustion mixtures (see Table 2-1) are shown in Figures 2-7 through 2-10. The equilibrium gas-phase concentrations shown in Figure 2-7a correspond to the situation when crystalline silica is in equilibrium with a SiO_2-rich liquid phase containing varying amounts of Na_2O or K_2O. Corrosion of the refractory is possible if the equilibrium calculation predicts the formation of a liquid alkali-silicate solution in equilibrium with crystalline silica as described by Reaction 2-2.

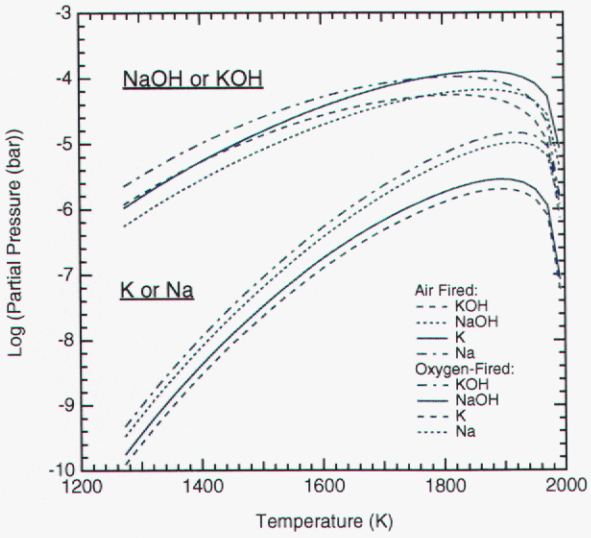

Figure 2-7a. Partial pressures of Na, NaOH, K, and KOH as a function of temperature for air- and oxy-fuel mixtures. The respective equilibrium water pressures produced by these fuel mixtures was 0.18 and 0.65 bar. As shown in Table 2-1, an input O_2/CH_4 fuel ratio of 2.05 was used. The gases were assumed to be in equilibrium with crystalline SiO_2 and a silica-rich liquid containing dissolved M_2O. As discussed in the text, data for NaOH(g) from the *JANAF Tables*[15] were used in these calculations.

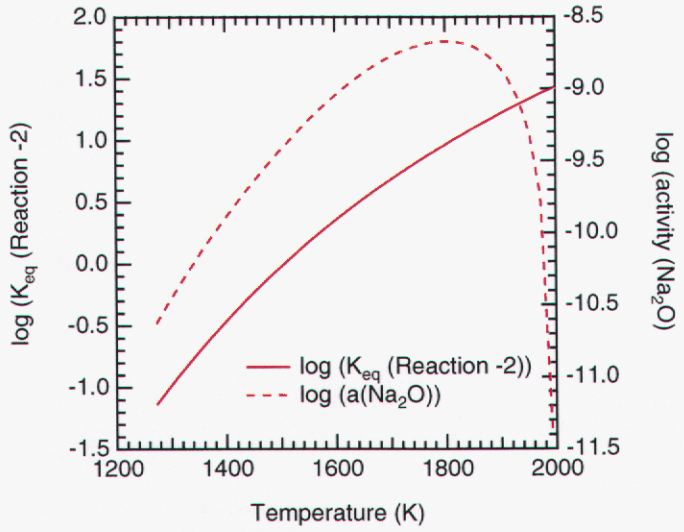

Figure 2-7b. Temperature dependence of the equilibrium constant for Reaction (2-2), with the Na_2O activity in the liquid phase.

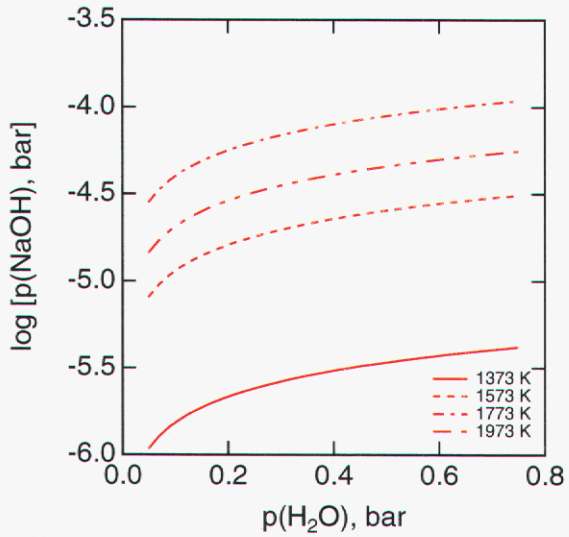

Figure 2-8. Partial pressure of NaOH as a function of H_2O partial pressure for temperatures of 1373, 1573, 1773, 1973 K (1100, 1300, 1500, 1700 °C). The gases were assumed to be in equilibrium with crystalline SiO_2 and a silica-rich liquid containing dissolved M_2O. JANAF data[15] for NaOH(g) were used.

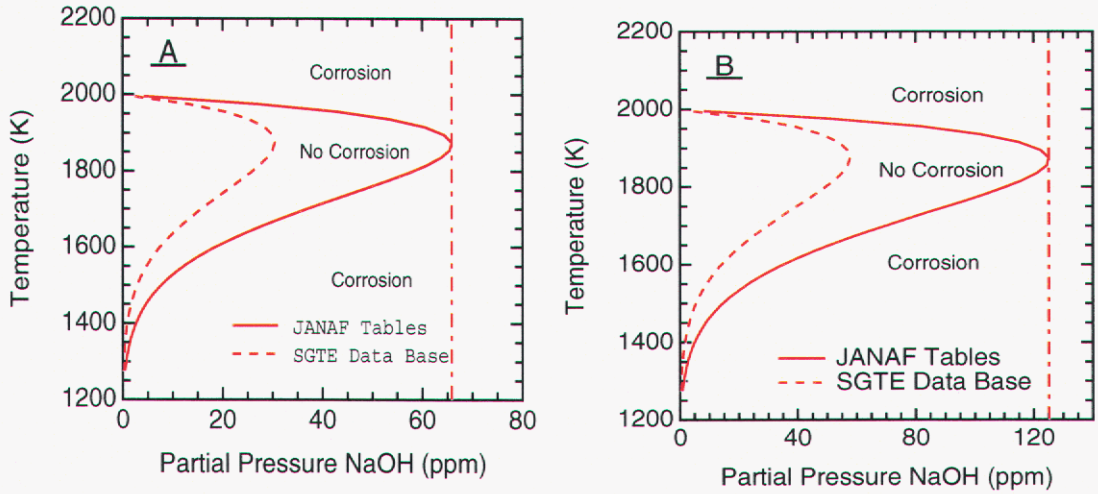

Figure 2-9. Zones of corrosion as a function of gas-phase partial pressure of NaOH, as defined by $T_{critical}$ (see text). (A): air-fired conditions; (B): oxy-fired conditions. Note the horizontal scales on the two plots are not the same. Data for NaOH(g) from the *JANAF Tables*[15] were used to calculate the solid curves; the dashed lines were calculated curves from using NaOH(g) data from the *SGTE database*[14] (see text). The differences in the two curves indicates the uncertainty in the zone of corrosion caused by the uncertainty in NaOH(g) thermodynamic data. The labels "Corrosion" and "No Corrosion" apply only to the solid curves. The vertical dash-dot line indicates the partial pressure of NaOH(g) above which corrosion occurs at all temperatures.

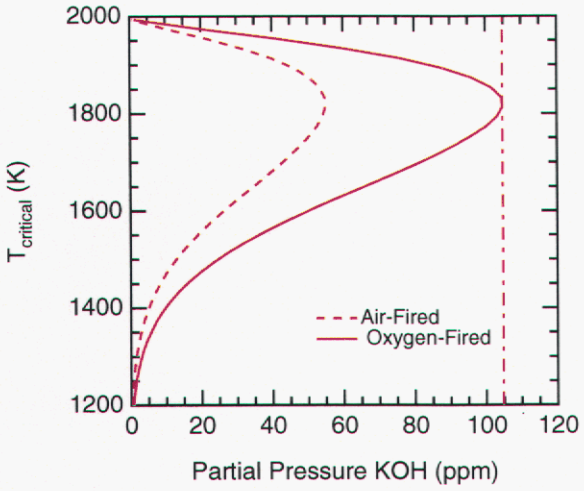

Figure 2-10. Zones of corrosion as a function of gas-phase partial pressure of KOH, as defined by $T_{critical}$ (see text) for air- and oxygen-fired melting conditions. The vertical dash-dot line indicates the partial pressure of KOH(g) above which corrosion occurs at all temperatures.

Figure 2-7a yields two important results. First, NaOH(g) is the dominant sodium-containing species and KOH(g) is the dominant potassium-containing species in the gas, significantly exceeding their respective atom concentration at all temperatures. Reaction 2-3 shows how the alkali metal atom partial pressures depend not only on the M_2O activities in the glass, but also on the $O_2(g)$ partial pressures:

$$(1/2)M_2O(glass) = M(g) + (1/4)O_2(g) \qquad (2\text{-}3)$$

The variations of oxygen pressure in a glass melting furnace atmosphere are not great enough to ever cause the M(g) equilibrium partial pressures to exceed those of MOH(g) species.

The predicted equilibrium concentrations of MOH(g) are always about a factor of two higher in oxy-fired furnace atmospheres than those predicted for air-fired furnace atmospheres. This is in qualitative agreement with reports that experimental concentrations of NaOH(g) in oxy-fuel furnaces are as much three to four times higher than in air-fired furnaces,[2] but suggests that other factors may be at work as well. The equilibrium prediction is simply a result of the differences in $H_2O(g)$ partial pressures in these two atmospheres [e.g., at 1873K oxy-fired $P(H_2O) = 0.654$ bar and air-fired $P(H_2O) = 0.177$ bar]. From Reaction 2-1 or 2-2, it is seen that the gaseous ratio

$$MOH_{oxy}/MOH_{air} = (H_2O_{oxy}/H_2O_{air})^{0.5} = (0.654/0.177)^{0.5} = 1.92 \qquad (2\text{-}4)$$

Maximum MOH(g) equilibrium partial pressures occur at ~1873 K for these two systems. This results from a combination of two competing effects. The decreasing concentration (activity) of $Na_2O(l)$ in the liquid corrosion product with increasing temperature (Figure 2-7b, dashed line) ultimately causes the NaOH(g) concentration to decrease at higher temperatures. Counteracting this effect, however, and leading to the maximum in the NaOH(g) concentration, is the increase with temperature in the equilibrium constant for the reaction $Na_2O(l) + H_2O(g) \leftrightarrow 2NaOH(g)$ (Figure 2-7b, solid line). This maximum has some interesting consequences with regard to the regions in which corrosion is predicted to occur; this is discussed in more detail below.

In addition to predicting the concentrations of sodium-containing gas-phase species, the calculations indicate that, over the 1200–2000 K temperature range of interest, p_{H2O} is practically constant: 65.6 to 65.2% for oxy-fired, and 17.8 to 17.6% for air-fired fuel mixtures. This occurs because the combustion products of CH_4 and O_2 are primarily CO_2 and H_2O in this temperature range. It would thus be realistic to assume a fixed value of p_{H2O} at all temperatures of interest.

It should also be pointed out that, under actual furnace conditions, p_{H2O} may actually be lower than the values used here. This can be caused by the dilution of the combustion gases by gases such as CO_2, which evolves from the glass melt due to the decomposition of carbonate starting materials, or by the use of auxiliary oxy-fuel burners in air-fired furnaces. We do not directly account for these dilution effects since their values depend on the mixture of raw materials used to produce the glass. However, calculation of p_{NaOH} as a function of p_{H2O} (Figure 2-8) shows that, even with relatively wide variations in p_{H2O}, the partial pressure of NaOH(g) at a given temperature does not vary greatly. For example, increasing p_{H2O} from 0.51 bar to 0.75 bar at 1773 K results in only a 22% increase in p_{NaOH}.

We note here that the refractory temperature in actual glass-melting furnaces is routinely much higher than lower temperature limits shown in Figures 2-6 through 2-10 for the typically insulated crown.[29] Temperatures as low as 650 K can occur when the cold side of the crown is not insulated, but equilibrium calculations will almost certainly be of little use at such low temperatures since the approach to equilibrium is so slow.

The curves in Figure 2-9 show that, for a given p_{NaOH}, there are temperature regions in which corrosion will occur and where it will not occur. In general, corrosion occurs (i.e., a liquid sodium silicate phase forms) in the region of conditions to the right of each curve. For example, if the p_{NaOH} in the combustion atmosphere is higher than that in equilibrium with crystalline silica and the liquid sodium silicate phase (the boundary line in Figure 2-9), then corrosion can occur. The lower branch of the curves in Figure 2-9 thus defines a "critical temperature," above which corrosion does not occur for a given p_{NaOH} in the combustion atmosphere. This concept was introduced previously by Faber and Verheijn.[3,7] Above the lower branch of the solid curve, corrosion will not occur since p_{NaOH} is below the equilibrium value. These results are again consistent with the observations in actual furnaces, which show that insulating the cold side of the crown refractory, and thus increasing the temperature of the hot face, slows the rate of corrosion.[29]

It is important to note that our calculated p_{NaOH} corresponding to the critical temperatures determined by Faber and Verheijn[7] are considerably lower than the input p_{NaOH} values they used. In their work, Faber and Verheijn treated NaOH(g) as a reactant, using input concentrations of 60 ppm under air-fired conditions and 220 ppm under oxy-fired conditions. They also considered only the formation of crystalline sodium silicates (or their congruent melts) as corrosion products. These assumptions lead to critical temperatures of 1593 K for air-fired and 1681 K for oxy-fired furnaces. In contrast, our calculations, which include formation of a liquid corrosion product in equilibrium with SiO_2, yield 17.9 ppm and 63.5 ppm, at 1593 K and 1681 K, respectively. Thus, our results suggest that the NaOH(g) concentration above which corrosion will occur at a given temperature is significantly lower than was previously predicted. The differences between our critical temperatures and those of Faber and Verheijn are largely due to the inclusion of the liquid corrosion phase, although the thermodynamic data for NaOH(g) and several condensed-phase species are not identical between the two investigations (Ref. 6 uses the SGTE database exclusively; exceptions to this for our study are given in Table 2-2).

Interestingly, the results in Figure 2-9 suggest that, if sufficiently high temperatures are reached (i.e., above the upper branch of the curves), corrosion should resume, since the NaOH concentration will again exceed the equilibrium value. This is a direct consequence of the fact that there is a maximum in the p_{NaOH} vs. temperature curve (Figure 2-7a). Practically speaking, the amount of corrosion might be very small at these temperatures, since the calculations reveal that the amount of Na_2O in the liquid corrosion product decreases as temperature increases (Figures 2-2 and 2-6), leading to more viscous liquids that could pose a transport limitation to the reaction. At concentrations above ~66 ppm (air-fired) or ~125 ppm (oxy-fired), corrosion can occur at all temperatures since p_{NaOH} is always above the liquid-SiO_2(crystalline) equilibrium value.

The two curves in Figure 2-9 show that the region in which corrosion occurs shifts to higher p_{NaOH} at a given temperature as one shifts from an air-fired to an oxy-fired furnace; i.e., as the concentration of water vapor in the furnace atmosphere increases. However, this result can be misleading if one does not take into account the fact that air-fired combustion atmospheres contain lower concentrations of NaOH(g) than oxy-fired atmospheres because of the higher water concentrations in the oxy-fired furnaces.

Finally, Figure 2-9 shows the effect of the difference in the SGTE[14] and *JANAF*[15] thermodynamic values for NaOH(g) in predicting the critical boundary lines that separate corrosive from non-corrosive conditions for air-fired and oxygen-fired furnaces. This figure provides a measure of the uncertainty in quantitative numbers produced by our calculations. However, the general conclusions and explanations of the observed corrosion behavior are not dependent on the formation enthalpies of NaOH(g).

The equilibrium behavior of K_2O and Na_2O are expected to be qualitatively the same based on their similar chemical nature and this is borne out by the calculations reported here. Data for the K_2O-SiO_2 system are shown in Figures 2-6, 2-7a, and 2-10, the first two of which also include the predictions for the Na_2O-SiO_2 system for direct comparison.

Figure 2-7a displays the predicted equilibrium partial pressures of KOH and K as a function of temperature. Like the Na_2O-SiO_2 system, the hydroxide is the potassium-containing species in highest concentration in the gas phase, followed by potassium atoms; no other gas-phase potassium-containing species are present in significant concentrations. The maximum p_{KOH} of ~104 ppm under oxy-fuel conditions and ~55 ppm under air-fuel conditions is slightly lower than p_{NaOH} and is shifted to slightly lower temperatures (1823 K for KOH vs. 1873 K for NaOH). The partial pressure of KOH is close to that of NaOH, regardless of whether air or oxygen is used. These results suggest that silica stability in atmospheres containing KOH should be similar to that in atmospheres containing comparable amounts of NaOH.

Implications for "Ratholing" in Refractory Joints

These results suggest a mechanism that could be responsible for the phenomenon known as "ratholing," in which large voids form in the interior of the crown refractories.[29] These voids are typically connected to the hot face of the refractory via a narrow channel. The initial formation of the channel may be caused by relatively slow corrosion, perhaps along a joint or originating at a defect of some kind. After reaching relatively cooler regions in the interior of the refractory, however, corrosion may accelerate since there is a stronger thermodynamic driving force at lower temperatures. This driving force results from two factors: first, lower temperatures lead to lower equilibrium p_{NaOH} (Figure 2-7a). Second, lower temperatures also favor liquid corrosion products containing higher concentrations of sodium (Figure 2-6). As a result, if the p_{NaOH} in the channel at some point in the interior of the refractory exceeds the equilibrium value, the excess NaOH will react with the refractory to form more of the liquid-phase corrosion product, which will then reduce p_{NaOH} and increase the fraction of Na_2O in the liquid phase. As mentioned previously, increasing the concentration of sodium in the liquid phase reduces its viscosity.[27,28] Hence, liquid products formed at cooler temperatures may be more prone to flow back out the original entrance channel than more viscous ones formed at higher temperatures. This constant removal of reaction product could maintain a condition in which fresh refractory is continuously exposed to gas-phase NaOH, leading to continued corrosion and thus, the opening of an interior void.

This mechanism, if true, confirms strategies currently used by the industry to avoid ratholing; namely, (a) insulating the back (cool) side of the refractory to minimize the temperature gradient and (b) taking great care to avoid openings in joints through which corrosive gases can travel to cooler portions of the refractory.

Thermodynamics of the $SiO_2/Na_2O/CaO$ System

CaO is used in silica-based refractories as a binder to provide structural integrity. Recently, some short-duration experiments in an oxygen-fuel glass furnace indicate that removing some or all of this calcium can reduce the rate of corrosion.[30] Since thermodynamic data for the $SiO_2/Na_2O/CaO$ system are now available** it is possible to evaluate the causes of this effect from a thermodynamic point of view. Equilibrium calculations were thus performed for a typical oxygen-fuel mixture ($O_2/CH_4 = 2.05$; 0.1 mol Na_2O; activity of SiO_2(cristobalite) fixed at 1.0). The CaO/Na_2O ratio was varied from 0 to 1.0, using temperatures expected for the crown hot face. The results are shown in Figure 2-11.

** (see the web site at www.ca.sandia.gov/HiTempThermo/)

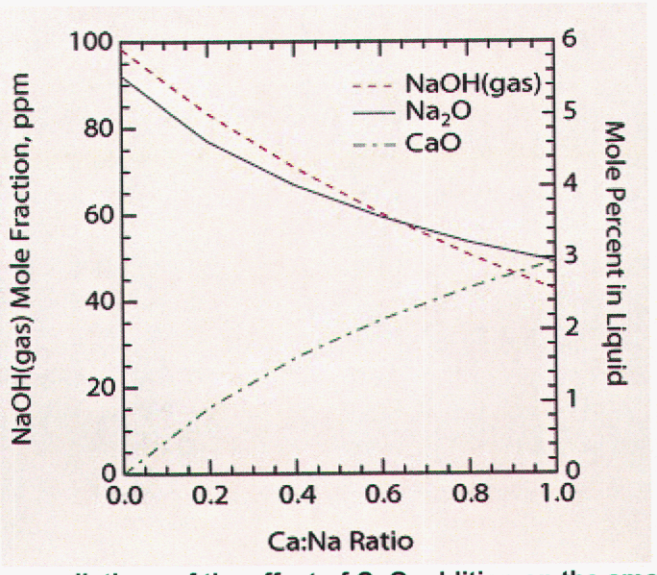

Figure 2-11. Equilibrium predictions of the effect of CaO addition on the amount of NaOH(gas) and the concentration of Na_2O that can dissolve in liquid SiO_2 that is in equilibrium with crystalline SiO_2.

The results suggest two reasons why the presence of CaO in the refractory could increase corrosion rates. First, CaO addition decreases the partial pressure of NaOH(gas) that can be in equilibrium with the liquid corrosion product and crystalline silica. As will be seen below, this increases the corrosion rate by increasing the magnitude of the concentration gradient between the ambient NaOH(gas) in the furnace and that at the surface of the refractory. Second, the concentration of Na_2O that can dissolve in the liquid corrosion product decreases, which accelerates corrosion since less Na_2O is required to form a liquid corrosion product (see Equation 4-4 below). Both factors support arguments presented below that corrosion occurs primarily at the front (hot) face of the refractory.

Summary and Conclusions

The results of equilibrium calculations for the Na_2O-SiO_2 and K_2O-SiO_2 systems are reported and indicate that the principal product of the corrosion of SiO_2 refractories by gas-phase NaOH and KOH is a molten glass containing variable amounts of sodium or potassium. The amount of alkali in this product increases with decreasing temperature of the refractory. Since increasing alkali concentrations in the molten corrosion product correlate with decreasing viscosity, the results suggest that higher refractory temperatures could inhibit corrosion by promoting the formation of products that are less prone to flow away from the surface. This result confirms anecdotal evidence available from the glass-manufacturing industry. The calculations also indicate that a critical temperature exists at a given alkali hydroxide partial pressure above which corrosion is not thermodynamically favored to occur, since the equilibrium hydroxide vapor pressure is higher than that existing in the furnace atmosphere. Together, these results suggest a mechanism whereby temperature gradients across the refractory crown of a glass-melting furnace could lead to formation of interior voids in the refractory (also known as "ratholing").

References

[1] Pecoraro, G. A.; Marra, J. C.; Wenzel, J. T., (ed.), *Corrosion of Materials by Molten Glass*, American Ceramic Society, Westerville, 1996.

[2] Boillet, J.; Paskocimas, C. A.; Leite, E. R.; Longo, E.; Varela, J. A.; Kobayashi, W. T.; Snyder, W. J. in G. A. Pecoraro, J. C. Marra and J. T. Wenzel (ed.), *Corrosion of Materials by Molten Glass, Ceramic Trans. Vol 78*, American Ceramic Society, Westerville, 1996, p. 217.

[3] Faber, A. J.; Verheijen, O. S., *Ceram. Eng. Sci. Proc.*, **18** (1997), 109.

[4] Slade, S. J. in G. A. Pecoraro, J. C. Marra and J. T. Wenzel (ed.), *Corrosion of Materials by Molten Glass*, American Ceramic Society, Westerville, 1996, p. 195.

[5] Wu, K. T.; Kobayashi, H. in G. A. Pecoraro, J. C. Marra and J. T. Wenzel (ed.), *Corrosion of Materials by Molten Glass*, American Ceramic Society, Westerville, 1996, p. 205.

[6] Godard, H. T.; Kotacska, L. H.; Wosinski, J. F.; Winder, S. M.; Gupta, A.; Selkregg, K. R.; Gould, S., *Ceram. Eng. Sci. Proc.*, **18** (1997), 181.

[7] Faber, A. J.; Verheijen, I. O. S. "Report NCNG-project: Reduction of Refractory Corrosion-Phase 1," TNO Institute of Applied Physics HAM-RPT-96396, 1996.

[8] Wu, P.; Eriksson, G.; Pelton, A. D., *J. Am. Ceram. Soc.*, **76** (1993), 2059.

[9] Zaitsev, A. I.; Shelkova, N. E.; Lyakishev, N. P.; Mogutnov, B. M., *Phy. Chem. Chem. Phys.*, **1** (1999), 1899.

[10] Spear, K. E.; Besmann, T. M.; Beahm, E. C., *MRS Bull.*, **24** (1999), 37.

[11] Spear, K. E.; Allendorf, M. D. in *The Per Kofstad Memorial Symposium on High Temperature Materials Chemistry*, The Electrochemical Society Proceedings Series, Honolulu, 1999, p. 439.

[12] Eriksson, G.; Hack, K., *Met. Trans. B*, **21B** (1990), 1013.

[13] "ChemSage™ 4.1," GTT Technologies, Herzogonrath, Germany 1998.

[14] Eriksson, G.; Hack, K. "SGTE Pure Substance Database, 1996 Version," produced by the Scientific Group Thermodata Europe and obtained through GTT Technologies (see Ref. 13).

[15] Chase Jr., M. J., *J. Phys. Chem. Ref. Data, Monograph 9*, (1998), 1 {NIST-JANAF Thermodynamic Tables, 4th Ed.}.

[16] Gorokhov, L. N.; Emelyanov, A. M., *Russ. J. Phys. Chem.*, **70** (1996), 1003.

[17] Gurvich, L. V.; Bergman, G. A.; Gorokhov, L. N., *J. Phys. Chem. Ref. Data*, **25** (1996), 1211.

[18] *Phase Diagrams for Ceramists*, Vols. 1-12, The American Ceramic Society, Westerville, OH, 1964-1996.

[19] Neudorf, D. A.; Elliott, J. F., *Met. Trans.*, **11B** (1980), 607; data taken from Ref. 8 in this paper.

[20] Yamaguchi, S.; Imai, A.; Goto, K. S., *Scand. J. Metall.*, **11** (1982), 263; data taken from Ref. 8 in this paper.

[21] Tsukihashi, F.; Sano, N., *Tetsu to Hagane*, **71** (1985), 815; data taken from Ref. 8 in this paper.

[22] Yamaguchi, S.; Imai, A.; Goto, K. S., *J. Jpn. Inst. Metals*, **47** (1983), 736.

[23] Kohsaka, S.; Sato, S.; Yokokawa, T., *J. Chem. Thermo.*, **11** (1979), 547.

[24] Frohberg, M. G.; Caune, E.; Kapoor, M. L., *Arch. Eisenhuttenwes.*, **44** (1973), 585; data taken from Ref. 8 in this paper.

[25] Ravaine, D.; Azandegbe, E.; Souquet, J. L., *Silic. Ind.*, **40** (1975), 333; data taken from Ref. 8 in this paper.

[26] Steiler, J. M., *Comm. Eur. Communities [Rep.] EUR.*, **EUR 8720 Pt. 2** (1982), 21; data taken from Ref. 8 in this paper.

[27] Bockris, J. O. M.; MacKenzie, J. D.; Kitchener, J. A., *Trans. Faraday Soc. (London)*, **51** (1955), 1734.

[28] Bansal, N. P.; Doremus, R. H. *Handbook of Glass Properties*, Academic, Orlando, 1986.

[29] LeBlanc, J., *Ceram. Ind.*, **146** (1996), 27.

[30] J. T. Brown; R. F. Spaulding; D. S. Whittemore; H. E. Wolfe. "New Silica Refractory of Oxy/Fuel Glass Melting" *Int. J. Glass., Proc. XV A.T.I.V. Conf. Parma,* 1999, 120-128, (1999).

This page intentionally left blank.

CHAPTER 3[†]

THERMODYNAMIC ANALYSIS OF ALUMINA REFRACTORY CORROSION BY SODIUM OR POTASSIUM HYDROXIDE IN GLASS-MELTING FURNACES

Abstract

In this paper the high-temperature corrosion of Al_2O_3 refractories by MOH(g) (M = Na, K) found in the combustion atmospheres of typical air- and oxygen-fired glass-melting furnaces is examined using thermodynamic equilibrium calculations. These hydroxide species are considered to be the primary reactive alkali species since their partial pressures are significantly larger than those of M(g), the next most abundant gas-phase alkali-containing species expected in typical furnace atmospheres. Thermochemical simulations show that corrosion of α-alumina by NaOH(g) at typical furnace $p_{NaOH(g)}$ of around 200 ppm under oxy/fuel-fired conditions is unlikely as long as the refractory temperature exceeds 1564 K. For KOH(g) at 200 ppm, the temperature of the refractory must exceed 1515 K to avoid corrosion. Under air-fired conditions, $p_{NaOH(g)}$ is considerably lower (40–80 ppm); at 50 ppm, corrosion is thermodynamically unfavorable at temperatures above 1504 K. For KOH(g) at furnace levels of ~50 ppm, temperatures must be above 1458 K. The paper also presents a re-evaluation of the thermodynamic and phase equilibrium properties of the Na_2O-Al_2O_3 and K_2O-Al_2O_3 binary systems to develop accurate and self-consistent thermodynamic data. The data for MAl_9O_{14} (β-alumina) and $M_2Al_{12}O_{19}$ (β"-alumina) are particularly critical since these phases are likely products of the corrosion of alumina refractories by MOH vapors in glass melting furnaces.

Introduction

Alumina-based ceramics, such as bonded and fused cast aluminas [α-alumina (Al_2O_3), β-alumina (a measured experimental composition of $NaAl_9O_{14}$)[2], and a mixture of α-alumina and β-alumina, which we refer to as α-alumina/β-alumina], fused cast alumina-zirconia-silica (AZS), and fused mullite ($Al_6Si_2O_{13}$) provide alternatives to silica refractories. These materials are also subject to varying degrees of corrosion in oxy/fuel environments, however. While silica refractories react with alkali vapors to form low-melting sodium- or potassium-silicate glassy liquids that can drip from the crown into the molten glass,[3] mixing of these corrosion products with the glass melt is not always a problem since the chemical compositions of the two liquids are similar. In the case of alumina-containing refractories, however, formation of corrosion products that can drip, run, or spill into the glass melt can lead to defects in the final product.[4] Thus, there is a need to develop an understanding of the processes leading to corrosion of these alternative refractories in oxy/fuel furnaces to determine how furnace designs and/or operating conditions can be adjusted to reduce or eliminate corrosion. Thermodynamic calculations (*i.e.*, predictions of chemical compositions based on minimization of the Gibbs free energy) can play a useful role by identifying energetically stable species and predicting the extent of corrosion and formation of products. The high temperatures at crown surfaces (> 1850 K in some locations)[5] and long reaction times of months to years indicate that equilibrium should be a valid approximation to the chemistry.

[†] This chapter was originally published as K. E. Spear, M. D. Allendorf "Thermodynamic Analysis of Alumina Refractory Corrosion by sodium or potassium hydroxide in glass melting furnaces," *J. Electrochem. Soc.*, **149**, B551-B559, 2002 and was edited for this report.

To perform such calculations, however, it is critical to develop internally consistent thermodynamic properties for all phases in these systems, including liquids, since liquid corrosion products can be a factor in refractory corrosion in glass furnaces. With a complete set of data for each system, equilibrium calculations can be used to assess the potential importance of all possible product phases in the corrosion process.

Corrosion of alumina by sodium has been of interest for some time due to its use in low-pressure sodium discharge lamp envelopes,[6,7] composites,[8,9] and structural ceramics. Using various qualitative and semi-quantitative methods, the stability of alumina-containing refractories in glass-melting environments has been evaluated.[4] In general, β-alumina and α-alumina/β-alumina perform better than most other refractories in high-alkali environments. β-alumina is also of interest as a sodium-ion-conducting solid electrolyte, and thus its thermodynamic stability is of importance to this application as well.[10] Equilibrium calculations used to predict the stability of alumina refractories are reported in two studies;[4,11] however, it is unclear if internally consistent thermodynamic data were used. The results suggest that both α-alumina and α-alumina/β-alumina should be stable under typical oxy-fuel melting conditions and that alumina is more resistant to alkali attack than silica.

Earlier reports of thermodynamic properties (such as heats of formation, entropies, heat capacities, heats of transition, and activities) and phase diagrams for both the Na_2O-Al_2O_3 and K_2O-Al_2O_3 systems are summarized and critically evaluated by Eriksson *et al.*[12] The Na_2O-Al_2O_3 phase equilibria data also were evaluated thoroughly by Roth. [13] Thermodynamic data, primarily heats of formation and M_2O activities, for crystalline phases in the M_2O-Al_2O_3 (M = Na, K) systems are reported by several investigators. Specific reports and reviews are given for Na_2O activity measurements in α-β alumina two-phase compositions,[2,10,14-16] and for K_2O activity measurements in similar composition regions. [14,17,18]

The optimized phase diagrams published by Eriksson *et al.*[12] for the Na_2O- and K_2O-Al_2O_3 systems do not extend to M_2O mole fractions less than 0.5, but these authors have generated thermodynamic information for the liquid phases in the alumina-rich part of the diagrams. These compositions include the sodium- or potassium-containing liquid products that can form when either pure α-alumina or β-alumina reacts with alkali vapors. Eriksson *et al.* [12] used quasi-chemical model parameters to represent nonideal interactions in these liquid phases. However, these parameters are not easily adapted to the modified associate species model we are using for liquid solution phases.[3]

In this paper, we present a re-evaluation of the thermodynamic properties of the M_2O-Al_2O_3 binary systems (M = Na or K) to determine self-consistent sets of accurate thermodynamic information. The beta-aluminas, MAl_9O_{14} (β-alumina) and $M_2Al_{12}O_{19}$ (β"-alumina), are likely products of the corrosion of α-alumina by MOH vapors present in glass furnaces. Conditions required for reactions of MOH(g) with Al_2O_3 refractories in representative air- and oxygen-fired combustion atmospheres were determined. Our focus is on reactions involving MOH(g) since the hydroxide is the primary alkali-containing gaseous species; M(g) pressures are significantly smaller than the MOH(g) pressures in these furnace atmospheres. In addition to discussing the temperature dependence of MOH(g) and M(g) concentrations, we present graphs for both alkali-containing systems, from which a critical temperature for corrosion can be determined for any MOH(g) partial pressure in the furnace atmosphere between 0 and 1000 ppm. Due to the high liquidus temperatures of > 2150 K in the α-β regions of both the Na_2O-Al_2O_3 and K_2O-Al_2O_3 systems, the formation of low-viscosity liquids is unlikely under conditions typical of most air- and oxy-fuel glass melting furnaces.

Equilibrium Modeling Approach

To model alumina corrosion at equilibrium, one needs to know the partial pressure of $H_2O(g)$ (p_{H2O}), the activities of M_2O (a_{M2O}) as a function of temperature and composition, and the temperature-dependent equilibrium constants K_{eq} for all phase regions in the M_2O-Al_2O_3 systems. Thus, thermodynamic data such as heats of formation, entropies, heat capacities, heats of transition, and activities are needed for all gaseous and condensed species in the systems, including the crystalline and liquid phases that may be formed by the corrosion process. The required information for most gas-phase species was obtained from the assessed SGTE database.[19] However, the $\Delta H^{\circ}_{f,298}$ value for NaOH(g) in this database (-185.649 kJ/ mol) is quite different from that found in the *JANAF Thermochemical Tables* (-197.757 kJ/mol).[20] The corresponding values of the entropy (S°_{298}) from these two sources are quite similar, however, being 228.589 and 228.443 J/mol-K, respectively. The $\Delta H^{\circ}_{f,298}$ and S°_{298} values for solid NaOH(s) from the two sources are also essentially the same. Thus, the 12 kJ/mol difference in the $\Delta H^{\circ}_{f,298}$ values for NaOH(g) appears to be the only major uncertainty in the sodium hydroxide data used in our calculations. In the calculations described here, we chose to use the *JANAF* value for $\Delta H^{\circ}_{f,298}$(NaOH,g), for reasons that are discussed in detail in Chapter 1.[3]

Tabulated thermodynamic properties for liquid-phase corrosion products are lacking, so these values were determined along with an assessment and optimization of the values for crystalline phases in both the Na_2O-Al_2O_3 and K_2O-Al_2O_3 binary systems. The computer program ChemSage™[21] was our primary tool for developing an assessed, internally consistent thermodynamic database for these two M_2O-Al_2O_3 systems and for performing subsequent calculations of the high-temperature corrosion reactions between their MOH(g) vapors and Al_2O_3(s). The following paragraphs describe our analysis of available thermochemical information for these systems and our choices for the values used in the equilibrium calculations described later in this paper.

In developing self-consistent sets of thermodynamic properties for each system, we modeled the thermodynamic stabilities of M_2O-containing liquid-oxide solutions using a modified associate species approach described previously.[22] The negative free-energy terms caused by nonideal mixing of end-member liquid components in a system are contained in the formation energies of the liquid associate species in this model. For the two systems examined in this chapter, only ideal mixing of associate liquid species was needed to model the two respective liquid phases; no non-ideal solution parameters were needed. In both M_2O-Al_2O_3 binary systems, we modeled the liquid by using four "liquid associate species" of M_2O(l), $MAlO_2$(l), (1/3)$M_2Al_4O_7$(l), and Al_2O_3(l). To provide equal weighting of liquid species, the composition of each liquid associate has a total of 2 non-oxygen atoms in its formula. While these four liquid species may not exist as chemical entities that can be isolated and characterized, their formation energies and the ideal solutions comprised of them accurately represent the negative interaction energies that occur between M_2O and Al_2O_3 in these two alkali liquid oxide solutions. The ternary Na_2O-K_2O-Al_2O_3 is not examined in this paper.

The thermodynamic data for the binary M_2O-Al_2O_3 systems were assessed and optimized by performing a manual thermodynamic fitting of the binary equilibrium phase diagram for the two alkali-containing systems (see Ref. 12, 13, 23 and the references cited therein for the latest phase diagram data). Results were also compared with published thermodynamic activity values and assessments for the systems (see Refs. 2, 10, 12, 14–20). This procedure provides a means of testing and generating a set of self-consistent thermodynamic information for the systems, including data for the oxide liquid phases.[3,22] Using the resulting thermodynamic properties, we calculated the equilibrium compositions of the two systems using input conditions typical of air- and oxy-fuel glass melting furnaces. Input parameters used to perform the equilibrium calculations are given in Table 3-1. These conditions were chosen so that either crystalline α- or β-alumina is always present, as indicated in the last column of Table 3-1, which ensures the existence of the chosen crystalline alumina refractory at equilibrium. All calculations were performed at a pressure of 1 bar. The major species included in the various calculations are given in Table 3-2, which also includes the source for the thermodynamic data in each case. Table 3-3 gives thermodynamic data for important species used in the calculations in the Na_2O-Al_2O_3 and K_2O-Al_2O_3 systems.

Table 3-1. Typical input conditions for equilibrium calculations.
P(total) = 1 bar, T = 1173 K–2373 K (900–2100 °C)

	$n(CH_4)^a$	$n(O_2)^a$	$n(N_2)^a$	$n(M_2O)^{a,c}$	a(refractory)[b]
Calculation of p_{H2O}					
Air-fired	1.00	2.05	8.2	--	--
Oxygen-fired	1.00	2.05	--	--	--
Corrosion predictions					
Air-fired	1.00	2.05	8.2	0.1	1.0 (α)
Oxygen-fired	1.00	2.05	--	0.1	1.0 (α)
Air-fired	1.00	2.05	8.2	0.1	1.0 (β)
Oxygen-fired	1.00	2.05	--	0.1	1.0 (β)

[a] Moles. [b]Activity of either αAl_2O_3 or βalumina was fixed at unity. [c] M = Na or K.

Table 3-2. Major species used in calculations and sources of thermodynamic data.

Gas-Phase [a]				
N_2	H_2O	CH_4	O_2	NO
H_2	OH	CO_2	NO_2	N_2O
H	CO	HCN	NH_3	
Na	NaOH[b]	K	KOH	
Liquid Phase [c]				
Na_2O(l)	$NaAlO_2$(l)	(1/3)$Na_2Al_4O_7$(l)	Al_2O_3(l)	
K_2O(l)	$KAlO_2$(l)	(1/3)$K_2Al_4O_7$(l)		
Solid Phase [d]				
Na_2O	$NaAlO_2$	$Na_2Al_{12}O_{19}$ (β")	$NaAl_9O_{14}$ (β)	Al_2O_3(α)
K_2O	$KAlO_2$	$K_2Al_{12}O_{19}$ (β")	KAl_9O_{14} (β)	
Na_2CO_3	K_2CO_3			

[a] A total of 75 gaseous species were initially used in these calculations. The major source of these data was *SGTE* (Ref. 19) except as noted. [b] *JANAF* (Ref. 20). [c] The set of liquid associate species was developed in the current studies.[d] Additional fixed-composition nitride and carbide phases were initially used in these calculations, but were always at very low activities. The source of liquid and solid phase thermodynamic data is our current assessment of the type described in Ref. 22, using initial thermodynamics values from the literature (Ref. 2, 10, 12, 14–20).

Table 3-3. Thermodynamic data for important species in Na_2O-Al_2O_3 and K_2O-Al_2O_3 systems.

species	$\Delta H^o_{f,298}$ (J/mol)	S^o_{298} (J/mol-K)	T(K)	$Cp = a + bT + cT^2 + d/T^2$ (J/mol-K) a	$b10^3$	$c10^6$	$d10^{-5}$
gases							
Na	107,500	153.716	2700	21.025	-0.384	0.143	-0.134
			5500	13.002	1.375	0.199	208.714
NaOH[a]	-197,322	228.443	1500	51.971	2.281	0.778	-3.848
			6000	58.196	1.315	-0.115	-66.087
K	89,000	160.339	2100	21.136	-0.653	0.293	–0.172
			4500	16.475	-0.366	0.709	98.005
KOH	-232,630	236.376	1200	53.038	-0.004	2.094	-4.168
			3200	52.639	4.546	-0.614	-20.879
liquid associates							
Na_2O(l)	-370,284	108.988	1023	55.480	70.210	-30.540	-4.140
	ΔH^o_{trans}(1023K) = 1,757		1243	82.563	12.350	0	0
	ΔH^o_{trans}(1243K) = 11,924		1405	82.563	12.350	0	0
			3500	104.600	0	0	0
$NaAlO_2$(l)	-1,000,000	107.000	1000	86.485	40.295	-15.270	-20.625
			1923	100.027	11.365	0	-18.555
			3000	148.532	0	0	0
$Na_2Al_4O_7$(1/3)	-1,234,000	95.000	1000	96.820	30.323	-10.180	-26.120
			1923	105.848	11.037	0	-24.740
			3000	163.176	0	0	0
K_2O(l)	-327,300	129.958	1013	75.947	17.146	0	-5.916
			3000	100.000	0	0	0
$KAlO_2$(l)	-1,040,000	114.250	1000	96.719	13.763	0	-15.597
			2533	111.045	5.190	0	-18.555
			3000	148.532	0	0	0
$K_2Al_4O_7$(1/3)	-1,210,000	102.000	1000	103.642	12.635	0	-22.770
			2533	108.745	6.920	0	-24.740
			3000	161.643	0	0	0
Al_2O_3(l)	-1,564,604	98.679	2327	117.490	10.380	0	-37.110
			4000	192.464	0	0	0

Table 3-3 (cont.): Thermodynamic data for important species in Na_2O-Al_2O_3 and K_2O-Al_2O_3 systems.

species	$\Delta H^\circ_{f,298}$ (J/mol)	S°_{298} (J/mol-K)	T(K)	Cp = a + bT + cT^2 + d/T^2 (J/mol-K) a	$b10^3$	$c10^6$	$d10^{-5}$
crystalline solids							
Na_2O	-417,982	75.040	1023	55.480	70.210	-30.540	-4.140
	–417,982[b]	*75.061*[b]					
	ΔH°_{trans}(1023K) = 1,757		1243	82.563	12.350	0	0
	ΔH°_{trans}(1243K) = 11,924		1405	82.563	12.350	0	0
			3500	104.600	0	0	0
$NaAlO_2$	-1,111,000	64.500	1000	86.485	40.295	-15.270	-20.625
	-1,119,572	*65.321*	1923	100.027	11.365	0	-18.555
			3000	148.532	0	0	0
$Na_2Al_{12}O_{19}$	-10,685,000	369.750	1000	760.420	132.490	-30.540	-226.800
	-10,702,896	*358.119*	2000	787.503	74.630	0	-222.660
			3000	1259.384	0	0	0
$NaAl_9O_{14}$	-7,873,000	262.000	1000	556.445	81.800	-15.270	-169.065
	-7,873,369	*258.876*	2273	569.985	52.900	0	-166.995
			3000	918.390	0	0	0
K_2O	-361,700	96.000	1013	75.947	17.146	0	-5.916
	-361,498	*102.006*	3000	100.000	0	0	0
$KAlO_2$	-1,144,000	74.500	1000	96.719	13.763	0	-15.597
	-1,145,224	*81.159*	2533	108.745	5.190	0	-18.555
			3000	146.232	0	0	0
$K_2Al_{12}O_{19}$	-10,740,000	386.000	1000	780.887	79.426	0	-216.744
	-10,788,495	*374.908*	2200	804.940	62.280	0	-222.660
			3000	1254.784	0	0	0
KAl_9O_{14}	-7,900,000	268.000	1000	566.679	55.283	0	-164.037
	-7,916,168	*267.271*	2193	578.705	46.710	0	-166.995
			3000	916.088	0	0	0
Al_2O_3	-1,675,692	50.940	2327	117.490	10.380	0	-37.110
	-1,675,700	*50.820*	4000	192.464	0	0	0

[a] Data from Ref. 20 see text for discussion of uncertainties in NaOH(g) data.
[b] Values for $\Delta H^\circ_{f,298}$ and S°_{298} in *italics* are from Eriksson *et al.*[19]

Results

Na_2O-Al_2O_3 phase diagram and Na_2O activities. The calculated phase diagram resulting from our assessed dataset is shown in Figure 3-1a for the Na_2O-Al_2O_3 system. This diagram is generally in good agreement with the assessed diagrams given by Roth[13] and Eriksson *et al.* [12] except for a slight difference in the melting temperature for $NaAl_9O_{14}$, for which there is little experimental information. The thermodynamic stability of the liquid is changed very little by the differences. In Figure 3-1b, we also compare our calculated Na_2O activities for the α-Al_2O_3 – β-$NaAl_9O_{14}$ two-phase region with the more recent values reported in the literature (see Refs. 2, 10, 14, 15). Nafe[10], Petric and Chatillon[15], and Jacobs *et al* [2] also show graphs including other reported activity values along with their own respective measurements. Except for the high temperature mass spectrometric vapor pressure measurements of Petric and Chatillon, all other activity measurements were made using lower temperature solid-state electrolyte galvanic cells.

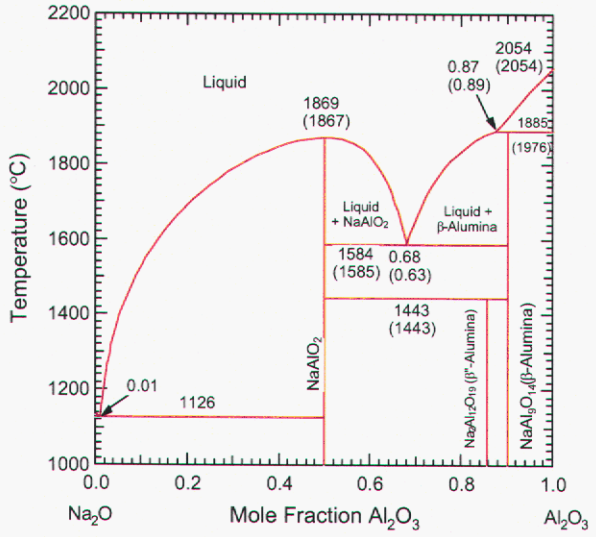

Figure 3-1a. Calculated phase diagram for the Na_2O-Al_2O_3 system. Note that temperatures in are given in °C for ease of comparison with published phase diagrams; most temperatures in this article are given in K. Current temperatures are shown, along with previously reported values in parentheses: Ref. 12, Eriksson et al.

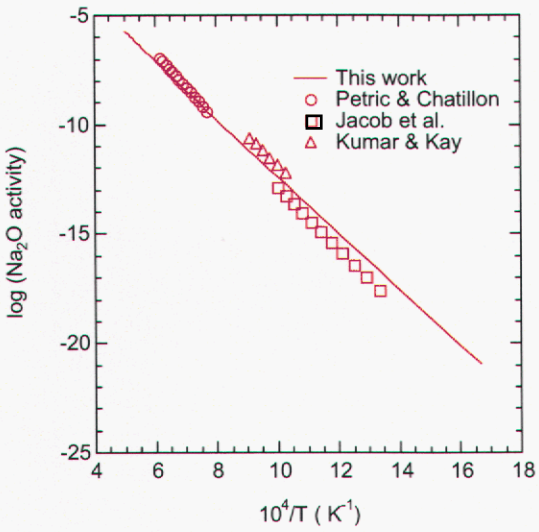

Figure 3-1b. Calculated *ln* a(Na_2O) vs. $10^4/T$ in the α-alumina/β-alumina two-phase region in the Na_2O-Al_2O_3 system.

K_2O-Al_2O_3 phase diagram and K_2O activities. Our calculated phase diagram for the K_2O-Al_2O_3 system is shown in Figure 3-2a, and is also in good agreement with the assessed diagram given by Eriksson *et al.*,[12] except for a slight difference in the melting temperature of KAl_9O_{14}, for which there is little experimental information. The thermodynamic stability of the liquid is changed very little by the differences. As discussed by Eriksson *et al.* [12], the very existence of the β"-alumina ($K_2Al_{12}O_{19}$) is uncertain, let alone its peritectoid decomposition temperature. Eriksson *et al.*[12] show the β-phase melting by a peritectic reaction at 1920 °C to give α-alumina and liquid (mole fraction $X(Al_2O_3) = 0.75$). In contrast, our calculated diagram has a congruently melting β-phase at 1989 °C and an α-alumina/β-alumina eutectic at 1984 °C, as shown in Figure 3-2a.

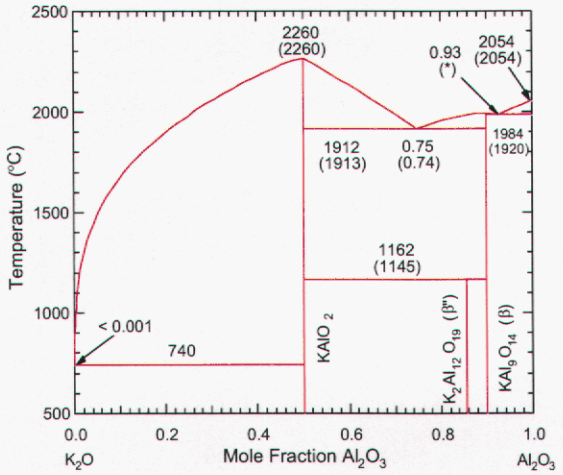

Figure 3-2a. Calculated phase diagram for the K_2O-Al_2O_3 system. The 1 bar gas phase that can occur at temperatures above ~1500 °C at the K_2O boundary of this diagram is not shown. Note that temperatures are given in °C for ease of comparison with published phase diagrams; most temperatures in this article are given in K. Current temperatures are shown, along with previously reported values in parentheses: Ref. 12, Eriksson et al. * For explanation of melting in the α-alumina/β-alumina two-phase region, see Results section of text.

We also compared our calculated K_2O activities for the α-Al_2O_3 – β-KAl_9O_{14} two-phase region with those reported in the literature (see Refs. 14, 17, 18); the results are shown in Figure 3-2b. Possible reasons for the high values of Kumar and Kay[14] have been thoroughly discussed by Kale and Jacob.[17] The reported experimental studies in this system all involved solid-state electrochemical cells.

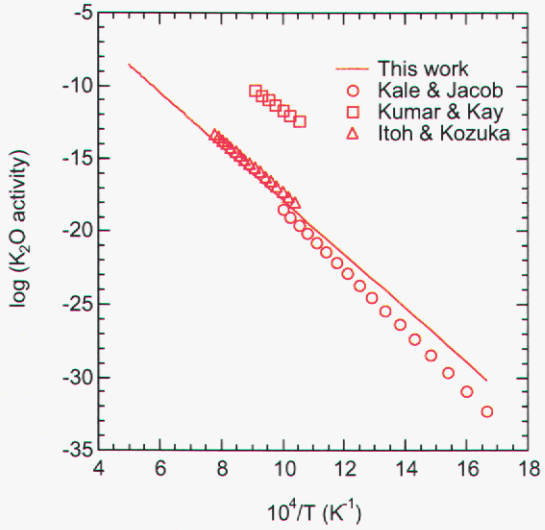

Figure 3-2b. Calculated *ln* a(K_2O) vs. 10^4/T in the α-alumina/β-alumina two-phase region in the K_2O-Al_2O_3 system.

The phase diagrams in Figures 3-1a and 3-2a clearly show why alumina-based ceramics are more resistant to corrosion by NaOH or KOH than silica.[3] In contrast with silica corrosion, the formation of liquid-phase products relatively rich in M_2O can only occur at very high temperatures in the M_2O-Al_2O_3 systems. Such products are not present until the temperature reaches 1857 K (1584 °C) for the sodium case, and 2185 K (1912 °C) for the potassium case, where β- alumina reacts to form a liquid. In the Na_2O-SiO_2 system, liquids can form at temperatures as low as 1090 K.[3] Pure α-alumina in contact with MOH(g) cannot form a liquid until the temperature reaches 2158 K for M = Na, or 2257 K for M = K.

Corrosion Modeling Approach. We now discuss the chemical reactions involved in the corrosion of α- and β-alumina by NaOH and KOH. Equilibrium calculations by ourselves and others[3,24,25] show that NaOH(g) is the most abundant sodium-containing gas when the combustion atmosphere equilibrates with sodium-containing glass melts. This is also true for KOH(g) in glass melts containing potassium. Therefore, we assume that NaOH(g) is the key sodium-containing species participating in the corrosion of alumina, and that KOH(g) is the key potassium-containing species involved. The formation of these hydroxides can be described by the following generic chemical reaction, where M = Na or K:

$$M_2O(\text{in glass melt}) + H_2O(g, \text{combustion gas}) \leftrightarrow 2\ MOH(g) \qquad (3\text{-}1)$$

At the surface of the refractory, the MOH can then react to form several products, as is evident from the phase diagrams in Figures 3-1a and 3-2a. The activity of condensed M_2O in the glass, $a(M_2O)$, is determined by the temperature and composition of the glass melt. The p_{H2O} value expected in the combustion atmosphere of an air-fired furnace is fixed by the fuel/air ratio at ~0.18 bar (in the calculations reported here, p_{H2O} was calculated from the fuel/oxidizer ratios given in Table 3-1). Anecdotal reports indicate that the resulting NaOH(g) pressure is ~$4x10^{-5}$ – $8x10^{-5}$ bar (40–80 ppm) for typical soda-lime-silica glass melting. The corresponding values for oxy-fired furnaces are ~0.65 bar for the fixed partial pressure of H_2O(g) and ~$1x10^{-4}$ –$2.5x10^{-4}$ bar (100–250 ppm) for NaOH(g); these results are consistent with NaOH measurements by Walsh *et al.* based on atomic-sodium absorption spectroscopy.[26] For purposes of illustration in the remainder of the paper, we will use 50 ppm as a representative p_{NaOH} for air-fired furnaces and 200 ppm for oxy-fired furnaces. We note, however, that NaOH(g) partial pressures are expected to vary from furnace to furnace. Thus, the thermodynamic potential for corrosion in a specific combustion environment can be evaluated from plots of the equilibrium NaOH(g) pressure given below.

For corrosion of alumina by NaOH(g) to occur, the phase diagram in Figure 3-1a shows that several reactions are possible. First, if NaOH(g) reacts with α-alumina, crystalline β-alumina can form at T ≤ 2158 K (1885 °C; Reaction 3-2a). At T > 2158 K, the NaOH(g) would react to form an alumina-rich liquid solution (Reaction 3-3a).

$$T < 2158\ K: \quad 2\ NaOH(g) + 9\ Al_2O_3 \leftrightarrow 2\ NaAl_9O_{14} + H_2O(g, \text{combustion gas}) \qquad (3\text{-}2a)$$

$$T > 2158\ K: \quad 2\ NaOH(g) \leftrightarrow Na_2O(\text{in } Al_2O_3\text{-rich liquid}) + H_2O(g, \text{combustion gas}) \qquad (3\text{-}3a)$$

Since the equilibrium value of p_{H2O} in a melting furnace is fixed by the fuel/oxidizer ratio, the p_{NaOH} in equilibrium with both α-alumina refractory and a corrosion product (Reactions (3-2a) or (3-3a)) is fixed at one value for a given temperature and partial pressure of water. Similarly, for Reaction (3-3a) under these conditions, the composition of the Al_2O_3-rich liquid corrosion product is also determined. If the combustion atmosphere has a larger p_{NaOH} than the equilibrium value for Reaction (3-2a), then this reaction proceeds to the right and β-alumina ($NaAl_9O_{14}$) can form. Likewise, if the combustion atmosphere has a larger p_{NaOH} than the equilibrium value for Reaction (3-3a), then this reaction proceeds to the right and an Al_2O_3-rich liquid can form.

Second, NaOH(g) can react with β-alumina. At temperatures above 1857 K (1584 °C; the eutectic point between $NaAlO_2$ and β-alumina) and Al_2O_3 mole fractions $0.68 < X_{Al2O3} < 0.9$, formation of liquid products can occur, with the liquid being in local equilibrium with β-alumina. NaOH(g) can also react with β-alumina to form β"-alumina at T < 1716 K (1443 °C; Reaction 3-4a), or $NaAlO_2$ at temperatures between 1716 and 1857K (1443 °C and 1584° C; Reaction 3-4a').

$$4\ NaAl_9O_{14} + 2\ NaOH(g) \leftrightarrow 3\ Na_2Al_{12}O_{19} + H_2O(g) \qquad (3\text{-}4a)$$

$$NaAl_9O_{14} + 8\ NaOH(g) \leftrightarrow 9\ NaAlO_2 + 4\ H_2O(g) \qquad (3\text{-}4a')$$

Similar arguments also hold for the case of potassium in glass melting furnaces. The K_2O-Al_2O_3 phase diagram in Figure 3-2a shows that if K_2O reacts with α-alumina, crystalline β-alumina in this system can form at T ≤ 2257 K (1984 °C; Reaction 3-2b). At T > 2257 K, the K_2O would react to form an alumina-rich liquid solution (Reaction 3-3b).

$$T < 2257\ K: \quad 2\ KOH(g) + 9\ Al_2O_3 \leftrightarrow 2\ KAl_9O_{14} + H_2O(g,\ combustion\ gas) \qquad (3\text{-}2b)$$

$$T > 2257\ K: \quad 2\ KOH(g) \leftrightarrow K_2O(in\ Al_2O_3\text{-}rich\ liquid) + H_2O(g,\ combustion\ gas) \qquad (3\text{-}3b)$$

Reactions (3-2b) and (3-3b) have only one equilibrium value for p_{KOH} at a given temperature and partial pressure of water if α-alumina is present at equilibrium. For Reaction (3-3b) under these conditions, the composition of the Al_2O_3-rich liquid is also determined. If the combustion atmosphere has a larger p_{KOH} than the equilibrium value for Reaction (3-2b), then this reaction proceeds to the right and β-alumina can form. Similarly, if the combustion atmosphere has a larger p_{KOH} than the equilibrium value for Reaction (3-3b), then this reaction proceeds to the right and an Al_2O_3-rich liquid can form.

At temperatures above 2185 K (1912 °C; the eutectic point between $KAlO_2$ and β-alumina) and $0.75 < X_{Al2O3} < 0.9$, liquid formation can also occur with the liquid being in local equilibrium with β-alumina. Finally, KOH(g) can react with β-alumina to form β"-alumina at T < 1435 K (1162 °C; Reaction 3-4b), or $KAlO_2$ at temperatures between 1435 and 2185 K (Reaction 3-4b').

$$4\ KAl_9O_{14} + 2\ KOH(g) \leftrightarrow 3\ K_2Al_{12}O_{19} + H_2O(g) \qquad (3\text{-}4b)$$

$$KAl_9O_{14} + 8\ KOH(g) \leftrightarrow 9\ KAlO_2 + 4\ H_2O(g) \qquad (3\text{-}4b')$$

The MOH(g) pressures required for Reactions (3-4) to occur can also drive the following reaction with the $CO_2(g)$ in the combustion environment:

$$2\ MOH(g) + CO_2(g) \leftrightarrow M_2CO_3 + H_2O(g) \qquad (3\text{-}5)$$

The partial pressures of all the gaseous species in Reaction (3-5) are fixed by the temperature and respective compositions of the input fuel/oxidizer ratio and the glass system being melted. Also, in the burning of natural gas by the reaction

$$CH_4(g) + 2\ O_2(g) \leftrightarrow CO_2(g) + 2\ H_2O(g) \qquad (3\text{-}6)$$

it is seen that the H_2O:CO_2 ratio is 2:1, independent of whether the source of oxygen is air or pure oxygen. Thus, the MOH(g) partial pressure in the furnace atmosphere is the variable that determines if Reaction (3-5) is thermodynamically favorable. Whether or not the alkali carbonate condensed phase can form is determined by the equilibrium constant of Reaction (3-5), its competition with Reactions (3-4), and the partial pressures in the furnace atmosphere. Note, however, that the temperatures required for carbonate formation to occur (< 1380 K) are not likely to be encountered by refractories in glass-melting furnaces. Thus, the potential for carbonate formation, while required for a complete thermodynamic treatment, should have no significant impact on alumina corrosion.

Equilibrium predictions of alumina corrosion regimes. The conditions in glass-melting furnace atmospheres that could lead to corrosion of α- or β-alumina refractories can be determined by performing fixed-temperature equilibrium calculations, using input compositions and a range of temperatures representative of the furnace combustion atmosphere (Table 3-1). Selected results from such calculations for the α-alumina – β-alumina two-phase regions of the Na_2O-Al_2O_3 and K_2O-Al_2O_3 systems are shown in Figures 3-3a and 3-3b, which display the partial pressures of MOH(g) and M(g) (p_{MOH} and p_M). These are the partial pressures that exist when the gas is in equilibrium with a condensed mixture containing both α– and β-alumina phases. Similar plots are given in Figures 3-4a and 3-4b for the β-alumina/M_2O-rich phase.

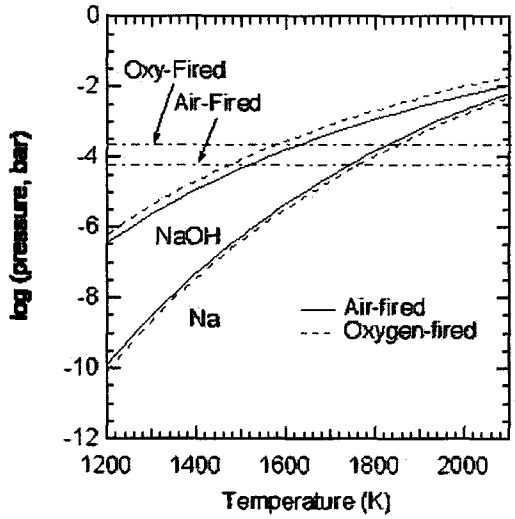

Figure 3-3a. NaOH(g) (upper curves) and Na(g) (lower curves) partial pressures in equilibrium with the α-alumina/β-alumina two-phase region as a function of temperature. The horizontal lines correspond to the example cases for air-fired (50 ppm, *log* P(bar) = -4.30) and oxy-fired (200 ppm, *log* P(bar) = -3.70) furnaces.

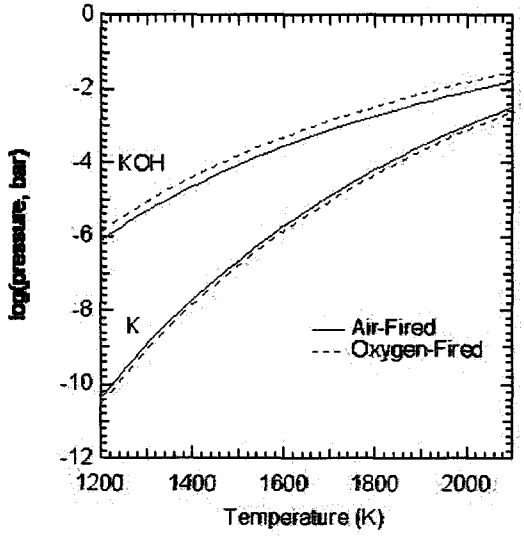

Figure 3-3b. KOH(g) and K(g) partial pressures in equilibrium with the α-alumina/β-alumina two-phase region as a function of temperature.

Several general observations for both the sodium and potassium systems can be made from the results in Figures 3-3 and 3-4. First, in their α-alumina/β-alumina two-phase regions (Figures 3-3a and 3-3b), the partial pressure of MOH(g) always exceeds that of M(g) by a substantial factor under all conditions, confirming that MOH(g) is indeed the equilibrium species that should be of concern in corrosion. Second, the predicted equilibrium MOH(g) partial pressures are always about a factor of two higher in oxy-fired furnace atmospheres than those predicted for air-fired furnaces, which, as discussed previously,[3] is simply a result of the differences in $H_2O(g)$ partial pressures in these two atmospheres (for example, at 1873 K oxy-fired $p_{H2O} = 0.654$ bar and air-fired $p_{H2O} = 0.177$ bar). From Reaction (3-1) or (3-2), it is seen that the gaseous ratio

$$MOH_{oxy}/MOH_{air} = (H_2O_{oxy}/H_2O_{air})^{1/2} = (0.654/0.177)^{1/2} = 1.92 \qquad (3\text{-}7)$$

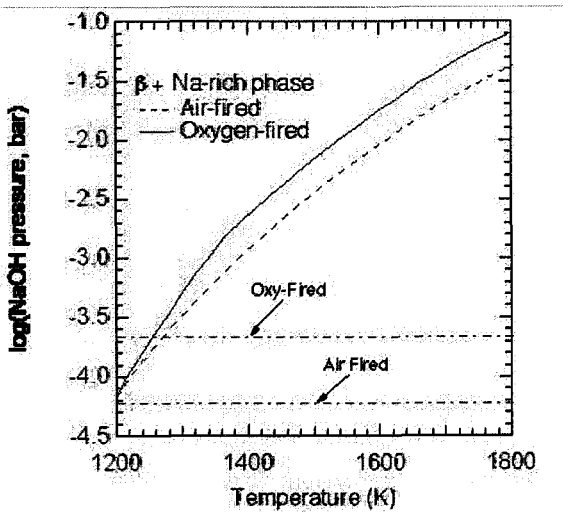

Figure 3-4a. NaOH(g) partial pressures in equilibrium with the β-alumina/Na-rich phase two-phase system as a function of temperature. See text for further description of Na-containing phases as a function of temperature. The horizontal lines correspond to p_{NaOH} example cases for air-fired (50 ppm, *log* P(bar) = -4.30) and oxy-fired (200 ppm, *log* P(bar) = -3.70) furnaces.

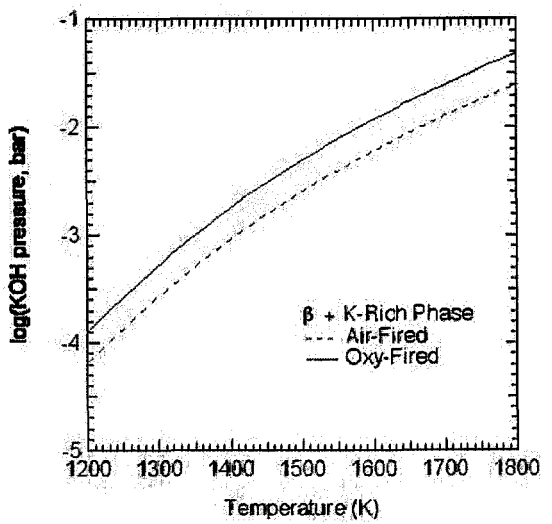

Figure 3-4b. KOH(g) partial pressures in equilibrium with the β-alumina/K-rich phase two-phase system as a function of temperature. See text for further description of K-containing phases as a function of temperature.

Finally, Figures 3-3a and 3-3b show that the concentration of both MOH and M gaseous species increases continuously with temperature up to at least 2100 K. This is quite different from the situation that exists in the M_2O-SiO_2 equilibria, in which there is a maximum in these concentrations at ~1873 K in the Na_2O-SiO_2 system,[3,24] and ~1800 K for the K_2O-SiO_2 system.[3] These temperature maxima are a result of the changing composition of the liquid corrosion product in equilibrium with crystalline SiO_2, which decreases in M_2O concentration with increasing temperature until no M_2O is present in the liquid at the melting point of SiO_2(cristobalite). As will be seen below, the fact that p_{MOH} and p_M increase continuously to very high temperatures in the alumina systems has consequences for the corrosion behavior of alumina refractories. Note that the points where the NaOH vapor-pressure curves intersect the horizontal lines in Figures 3-3a and 3-4a (representing values of p_{NaOH} in the combustion atmosphere) indicate the lowest temperature at which the equilibrium vapor pressure exceeds that in the furnace. This leads to the concept of a critical temperature (see below), above which no corrosion can occur. Thus, the predicted equilibrium NaOH(g) concentrations in these figures represent a lower limit for furnace concentrations that can result in corrosion.

Figures 3-3a and 3-3b can be used to identify regions of chemical stability when alumina is exposed to combustion environments representative of glass furnaces. In the case of NaOH(g), Figure 3-3a indicates that α-alumina should be stable in air-fired furnaces at T > 1504 K and in oxy-fired furnaces at T > 1564 K, since their respective equilibrium p_{NaOH} for the α–β two-phase system is higher than that found in air- (~50 ppm, or $5x10^{-5}$ bar) and oxy-fired (~200 ppm, or $2x10^{-4}$ bar) furnace atmospheres. For similar KOH(g) concentrations in a furnace atmosphere, α-alumina should also be stable at temperatures (Figure 3-3b) T > 1458 K for air-fired furnaces and T > 1515 K for oxy-fired furnaces.

In contrast, ceramics containing sodium β-alumina should decompose to α-alumina and NaOH(g) at T > 1504 K (air-fired) and T > 1564 K (oxy-fired), since the equilibrium p_{NaOH} exceeds that in the furnace; this phenomenon has been observed.[4] Ceramics containing potassium β-alumina could decompose to α-alumina and KOH(g) when the equilibrium p_{KOH} exceeds the values in the furnace; for furnace KOH(g) pressures of ~50 ppm for air-fired and ~200 ppm for oxy-fired, the respective temperatures are T > 1458 K (air-fired) and T > 1515 K (oxy-fired).

The β-alumina/M_2O-rich-phase equilibrium is somewhat more complex than the α-alumina/β-alumina equilibrium, since the M_2O-rich product phases in equilibrium with β-alumina depend on temperature. With increasing temperature, the possible product phase changes from β"-alumina to $MAlO_2$(s) to liquid. Figures 3-4a and 3-4b) show the p_{MOH} results for two-phase systems when MOH(g) reacts with β-alumina. The nature of these products is indicated by the possible chemical reactions discussed in the previous section. The M_2O-rich product phase in equilibrium with β-alumina in the Na_2O-Al_2O_3 system is Na_2CO_3(s) T < 1220 K (air-fired) or T < ~1380 K (oxy-fired). The difference in these two temperatures is the result of the difference in the assumed p_{NaOH} in the respective combustion atmospheres for air-fired and oxy-fired systems (50 ppm versus 200 ppm p_{NaOH}). At higher temperatures up to 1716 K (1443 °C, the β" peritectoid temperature), β"-alumina forms rather than Na_2CO_3. At even higher temperatures, up to 1857 K (1584 °C, the eutectic temperature), β"-alumina is unstable and $NaAlO_2$ forms. Finally, at temperatures between 1857 K and 2158 K (1584 °C–1885 °C), a sodium-rich (compared to β-alumina) liquid phase forms in equilibrium with β-alumina.

As is shown in Figure 3-4a for all temperatures > 1260 the NaOH(g) pressures required to produce these sodium-rich products are much higher than those present in a glass-melting furnace, so such products are not predicted to form under these conditions.

The M_2O-rich product phases in equilibrium with β-alumina in the K_2O-Al_2O_3 system do not include K_2CO_3(s) for the temperatures >1200 depicted in Figure 3-4b. At temperatures above 1200 K, the potassium β"-alumina forms rather than K_2CO_3 up to 1435 K (1162 °C, the β" peritectoid temperature) in both air- and oxy-fired environments. At higher temperatures up to 2185 K (1912 °C, the eutectic temperature), the potassium β"-alumina is unstable and $KAlO_2$ forms. Finally, at temperatures between 2185 K and 2262 K (1912 °C–989 °C), a potassium-containing liquid phase forms in equilibrium with β-alumina. As is shown in Figure 3-4b for all temperature > 1260, the KOH(g) pressures required to produce these potassium-rich products are >200ppm (*log* P(bar) > -3.70), the value estimated for p_{NaOH} in oxy-fired glass-melting furnaces. Thus, if KOH(g) levels are comparable to those of NaOH(g), K_2O-rich corrosion products are not predicted to form in these furnace environments.

Figure 3-4a indicates that the NaOH(g) concentration in equilibrium with the β-alumina/Na-rich product (liquid, $NaAlO_2$, or β"-alumina) two-phase region is much higher than that in equilibrium with the α-β alumina two-phase region (by a factor of 36 at 1800 K for both air- and oxy-fired conditions; at 1200 K, a factor of 200 for air-fired, and 102 for oxy-fired atmospheres). The difference between the p_{NaOH} ratios at 1200 K for air-fired and oxy-fired conditions is due to the reduction in p_{NaOH} at low temperatures caused by Na_2CO_3 formation in the oxy-fired conditions.

Figure 3-4a also shows that the equilibrium p_{NaOH} is *always* higher than typical furnace concentrations for T > 1250 K (oxy-fired) and T > 1200 K (air-fired), as indicated by the horizontal lines in the figure. Thus, the conversion of β-alumina to β"-alumina or any other Na-rich product phase by NaOH(g) is not thermodynamically feasible, and Reactions (3-4a), (3-4a') and (3-5) should not occur in typical glass melting furnaces. Similarly, Figure 3-4b indicates that the KOH(g) concentration in equilibrium with the β-alumina/K-rich product two-phase system is significantly higher than that in equilibrium with the α-β alumina two-phase system (ranging from a factor of 13 at 1800 K to a factor of 85 at 1200 K for both air- and oxy-fired conditions). Although to our knowledge no KOH(g) furnace concentrations have been reported, Figure 3-4b indicates that the equilibrium p_{KOH} is *always* higher than furnace concentrations of 200 ppm for T > 1240 K (oxy-fired), and of 50 ppm for T > 1200 K (air-fired). Thus, the conversion of β-alumina to β"-alumina or any other K-rich product phase by KOH(g) is probably not thermodynamically feasible either (again assuming that KOH(g) concentrations are comparable to those of NaOH(g)), and thus Reactions (3-4b), (3-4b'), and (3-5) should not occur in glass melting furnaces.

A final important observation is that M_2O-containing liquid alumina phases are not thermodynamically favored under typical furnace operating conditions, as they are when silica is used. Although the phase diagram for the Na_2O-Al_2O_3 system (Figure 3-1a) indicates the possibility of a liquid phase in equilibrium with β-alumina above 1857 K (1584 °C), the values of p_{NaOH} in equilibrium with that two-phase region are always much higher than typically observed under either air- or oxy-fired cases, so that one can safely conclude that these liquids will never form.

The data in Figures 3-3a and 3-3b can be replotted to show temperature as a function of MOH partial pressure to define regions in which corrosion is thermodynamically favored to occur (Figures 3-5a and 3-5b). In general, corrosion occurs (*i.e.*, α- is converted to β-alumina) in the region of conditions below each curve. For example, if the p_{NaOH} in the combustion atmosphere is higher than that in equilibrium with α- and β-alumina, the boundary line in Figure 3-5a, then corrosion can occur. The curves in Figures 3-5a and 3-5b thus define a "critical temperature," ($T_{critical}$) above which corrosion does not occur for a given p_{MOH} in the combustion atmosphere. This concept was introduced previously by Faber and Verheijn[25] and expanded upon by us in subsequent publications.[3,24] Above each curve, corrosion will not occur, since p_{MOH} in the furnace atmosphere is below the equilibrium value for the α-β two-phase region. At NaOH partial pressures representative of oxy-fuel furnaces (~200 ppm), the value of $T_{critical}$ is ~1564 K, Figure 3-5a. Under air-fuel conditions, where the NaOH partial pressure is much lower (~50 ppm), $T_{critical}$ is predicted to be ~1504 K. Note that, since our predicted equilibrium p_{NaOH} are expected to be lower limits for the NaOH(g) partial pressures needed to cause corrosion, our predicted values of $T_{critical}$ are actually upper limits for temperatures at which corrosion can occur at a given p_{NaOH} in the furnace atmosphere. Similar arguments can be made for Figure 3-5b and KOH partial pressures in the furnace atmosphere.

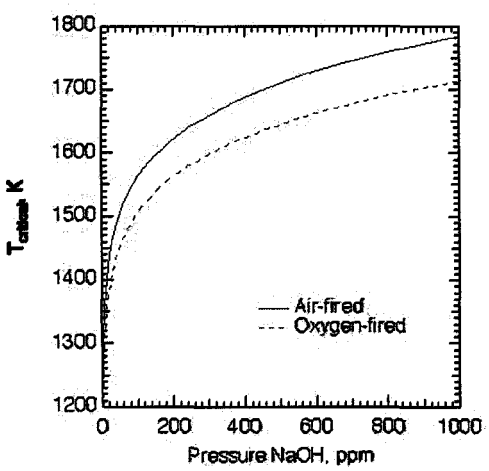

Figure 3-5a. Zones of alumina refractory corrosion by NaOH(g) as defined by $T_{critical}$ (see text) for the α-alumina/β-alumina two-phase region. The NaOH concentrations are given in units of ppm (parts per million at 1 bar) since this is the common measure of most glass manufacturers (we use the conversion of 1 ppm = 1x10^{-6} bar).

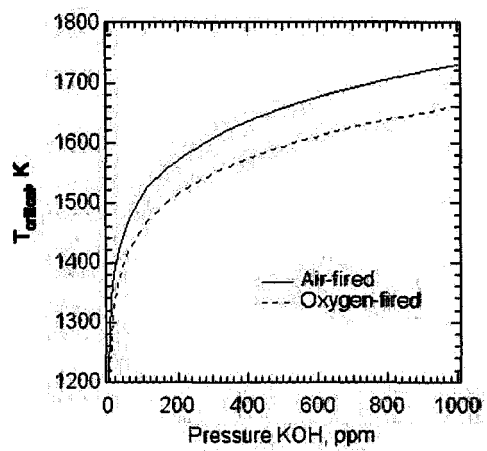

Figure 3-5b. Zones of alumina refractory corrosion by KOH(g) as defined by $T_{critical}$ (see text) for the α-alumina/β-alumina two-phase region. The KOH concentrations are given in units of ppm (parts per million at 1 bar).

The fact that the curves in Figure 3-5 increase continuously with temperature indicates that in the 1200–1800 K temperature range there will always be a temperature above which corrosion will not occur. This contrasts with corrosion of silica refractories, for which, because of a maximum in the p_{MOH} vs. $T_{critical}$ curves occurring at ~1800 K, there exist furnace conditions in which corrosion is always thermodynamically favored. A similar maximum also occurs in the M_2O-Al_2O_3 systems, but only at high temperatures where α-alumina can exist in equilibrium with a liquid phase; between 2158 and 2327 K for the sodium system, and between 2257 and 2327 K for the potassium system. Therefore, a maximum in the p_{MOH} vs. $T_{critical}$ curves for the alumina systems would never be observed under practical glass-melting conditions.

The results presented above suggest that there may be several advantages to using high-purity α-alumina as a crown material. First, $T_{critical}$(oxy) of 1564 K for 200 ppm NaOH(g) in the furnace atmosphere is considerably below the operating temperatures typically used for silica crowns (maximum continuous operating temperatures ~1853–1873 K), indicating that α-alumina should be thermodynamically stable in this temperature regime. Second, replacement of silica with alumina may provide additional flexibility with regard to burner optimization. Burner placement has been shown to affect crown temperatures; placing burners higher on the furnace wall (which may reduce NaOH and KOH volatilization rates) increases crown temperatures in some locations.[5] Since the temperatures at which alumina either melts or forms liquid corrosion products are much higher than 1873 K (Figures 3-1a and 3-1b), it can tolerate placement of burners in locations closer to the crown. Finally, the formation of liquid sodium silicates from the corrosion of silica refractories is much more deleterious to the refractory than the formation of β-alumina from the corrosion of α-alumina. The mechanical properties of corroded alumina refractories are evidently sufficient to inhibit structural damage.[4]

Summary and Conclusions

The thermodynamic calculations reported here, using newly generated data for sodium- and potassium-containing alumina phases, indicate that alumina is quite stable with respect to corrosion by MOH(g) under the conditions typical of glass-melting furnaces. Unlike silica, liquid-phase alkali aluminates are not stable except at very high temperatures and in equilibrium with extremely high MOH(g) partial pressures, indicating that these liquid products will not form. Thus, problems associated with formation of liquid corrosion products, such as run off of corrosion products into the melt and presumably, unacceptably high corrosion rates (as is the case for silica), should not be a problem for crowns constructed of either α- or β(Na)-alumina used in oxy-fuel melting furnaces. The negative aspect of using alumina refractories instead of silica is that they are heavier, so that glass-melting furnaces require special construction. They are also more expensive than silica, raising the capital costs of such furnaces.

References

[1] Corrosion of Materials by Molten Glass; Pecoraro, G. A.; Marra, J. C.; Wenzel, J. T., Eds.; American Ceramic Society: Westerville, 1996; Vol. 78.

[2] Jacob, K. T.; Swaminathan, K.; Sreedharan, O. M. Electrochim. Acta 36, 791 (1991).

[3] Allendorf, M. D.; Spear, K. E. J. Electrochem. Soc. 148, B59-B67 (2001).

[4] Godard, H. T.; Kotacska, L. H.; Wosinski, J. F.; Winder, S. M.; Gupta, A.; Selkregg, K. R.; Gould, S. Ceram. Eng. Sci. Proc. 18, 181 (1997).

[5] Wu, K. T.; Kobayashi, H. Three-dimensional modeling of alkali volatization/crown corrosion in oxy-fired glass furnaces. In Corrosion of Materials by Molten Glass; Pecoraro, G. A., Marra, J. C., Wenzel, J. T., Eds.; American Ceramic Society: Westerville, 1996; Vol. 78; pp 205.

[6] van Hoek, J. A. M.; van Loo, F. J. J.; Metselaar, R. J. Amer. Ceram. Soc. 75, 109-111 and references therein (1992).

[7] Dewith, G.; Vrugt, P. J.; Vandeven, A. J. C. J. Mat. Sci. 20, 1215-1221 (1985).

[8] Sundaram, S. K.; Hsu, J. Y.; Speyer, R. F. J. Amer. Ceram. Soc. 78, 1940-1946 (1995).

[9] Sundaram, S. K.; Hsu, J. Y.; Speyer, R. F. J. Amer. Ceram. Soc. 77, 1613-1623 (1994).

[10] Näfe, H. J. Electrochem. Soc. 143, 943 (1996).

[11] Faber, A. J.; Verheijen, O. S. Ceram. Eng. Sci. Proc. 18, 109 (1997).

[12] Eriksson, G.; Wu, P.; Pelton, A. D. CALPHAD 17, 189 (1993).

[13] Roth, R. S. Adv. Chem. 186, 391 (1980).

[14] Kumar, R. V.; Kay, D. A. R. Metal. Trans. B 16B, 295 (1985).

[15] Petric, A.; Chatillon, C. Determination of Beta Alumina Stability by High Temperature Mass Spectrometry. In Proc. Ninth Int. Conf. High Temp. Mater. Chem.; Spear, K. E., Ed.; The Electrochemical Society Proceedings Series: Pennington, 1997; Vol. 97-39; pp 718.

[16] Barsoum, M. J. Mater. Sci. 25, 4393 (1990).

[17] Kale, G. M.; Jacob, K. T. Met. Trans. B 20B, 687 (1989).

[18] Itoh, M.; Kozuka, Z. J. Amer. Ceram. Soc. 71, C36 (1988).

[19] Eriksson, G.; Hack, K. "SGTE Pure Substance Database, 1996 Version," produced by the Scientific Group Thermodata Europe and obtained through GTT Technologies (see Ref. 21).

[20] Chase Jr., M. J. J. Phys. Chem. Ref. Data, Monograph 9, 1 {NIST-JANAF Thermodynamic Tables, 4th Ed.} (1998).

[21] "ChemSage™ 4.1," GTT Technologies, Herzogonrath, Germany, 1998.

[22] Spear, K. E.; Besmann, T. M.; Beahm, E. C. MRS Bull. 24, 37 (1999).

[23] Phase Diagrams for Ceramists; Vols. 1-12, The American Ceramic Society: Westerville, OH, 1964-1996; Vol. 1-12.

[24] Spear, K. E.; Allendorf, M. D. The Per Kofstad Memorial Symposium on High Temperature Materials Chemistry, The Electrochemical Society Proceedings Series, 1999, vol. 99-38, 439 Honolulu.

[25] Faber, A. J.; Verheijen, I. O. S. "Report NCNG-project: Reduction of Refractory Corrosion-Phase 1," TNO Institute of Applied Physics, 1996.

[26] Buckley, S. G.; Walsh, P. M.; Hahn, D. W.; Gallagher, R. J. Ceram. Eng. Sci. Proc. 21[1], 183 (2000).

CHAPTER 4[†]

ANALYTICAL MODELS FOR HIGH-TEMPERATURE CORROSION OF SILICA REFRACTORIES IN GLASS-MELTING FURNACES

Abstract

To better understand and to quantify the corrosion of refractory silica brick, we utilize analytical models to evaluate the importance of four potential rate-limiting processes: 1) gas-phase transport of NaOH to the crown surface; 2) diffusion of sodium-containing reactants through a liquid product layer that forms on the brick face; 3) gas-phase diffusion of NaOH into refractory pores; and 4) chemical-kinetic limitations at the silica grain surface. Predictions are compared with reported corrosion rates and product compositions previously determined by post-mortem analysis of refractory samples. We conclude that corrosion occurs largely by reaction and removal of material from the exposed brick face, rather than by transport of reactants into the porous bricks. The observed presence of corrosion products deep within the brick pores is shown to be consistent with capillary suction of high-viscosity liquid products from the hot face into the interior. The results further suggest that mechanisms (2) and (3) do not substantially limit the rate of corrosion, but that mechanisms (1) and (4) may both be important. Comparison of measurements with equilibrium predictions of corrosion-product composition indicate that the corrosion reactions are likely to be close to equilibrium at the conditions and lifetimes typical of full-scale furnaces, but that significant departures from equilibrium may occur in short-duration tests. Although computed corrosion rates based on mass transport through a gas boundary layer are somewhat greater than those observed, the results are very sensitive to the gas-phase concentration of NaOH and to the refractory temperature, both of which contain significant uncertainties.

[†] This chapter was originally published as Robert H. Nilson, Stewart K. Griffiths, Nancy Yang, Peter M. Walsh, Mark D. Allendorf Benjamin Bugeat, Ovidiu Marin, K. E. Spear, and G. A. Pecoraro, "Analytical Models for High-Temperature Corrosion of Silica Refractories in Glass-Melting Furnaces," *Glass Sci. Technol.*, **76** (2003), 136 and was edited for this report.

Introduction

Chemically, corrosion of silica occurs when water reacts with components in the glass melt, typically Na_2O or K_2O to produce gas-phase NaOH(g) or KOH, which is then transported to the refractory surface. The hydroxide can react with silica to form a low-melting alkali-silicate product:

$$2MOH(gas) \leftrightarrow M_2O(\text{dissolved in liquid } SiO_2) + H_2O(gas);\ M = Na \text{ or } K \qquad (4\text{-}1)$$

This product can be absorbed into the pores of the refractory or drip and run down the sides of the furnace. The exact process that controls the corrosion rate is unknown. Potential candidates include (Figure 4-1): gas-phase mass-transport of MOH; transport of sodium through the liquid layer to the surface of the refractory; chemical kinetics at the silica surface; and diffusion of NaOH(g) through pores in the refractory, which we will term "in-depth" corrosion.

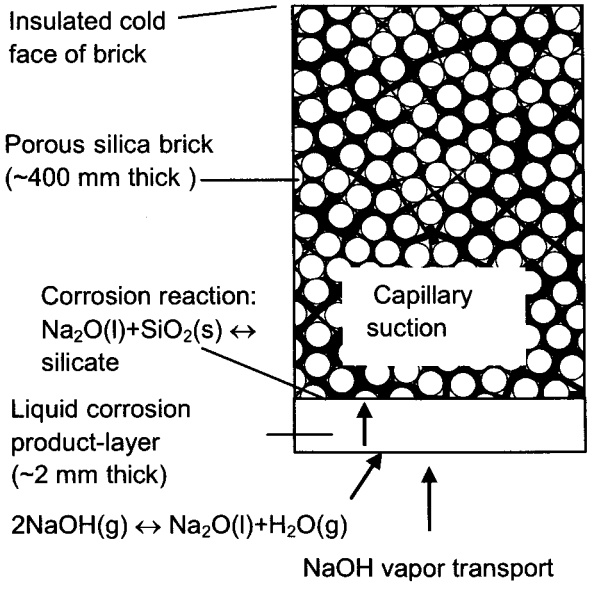

Figure 4-1. Schematic of corrosion process. A thin (~2 mm) layer of liquid reaction product coats brick surface. NaOH(g) vapor is transported to the lower surface of the liquid, releases H_2O to form $Na_2O(l)$ that diffuses through liquid layer to surface of solid SiO_2 grains. Reaction of Na_2O with SiO_2 forms additional silicate liquid that is drawn into the porous brick by capillary suction.

Early investigations going back to at least the early 1960s describe the formation of glassy corrosion products composed of sodium silicates. Work by Reich[1] and others[2, 3] characterized this process in air-fired furnaces and showed that the glassy phase migrates toward the cold end of porous refractory blocks; the importance of temperature gradients in the refractory was noted as well. Two general phenomena were observed in large-scale furnaces: front-face corrosion, in which the surface of the refractory was eroded over time, and so-called "ratholing," in which narrow channels at joints or gaps were invaded by combustion gases, creating wider channels and interior chambers in colder regions of the brick. In air-fired furnaces, the latter was a severe problem until the 1960s, when furnace crowns were insulated, virtually eliminating the problem.[4] Front-face corrosion is sufficiently slow in air-fired furnaces that crown lifetimes of up to ten years can be achieved, which is an acceptable rate of degradation.

The advent of oxy-fuel melting technologies in the late 1980s and early 1990s caused silica corrosion to again become a major concern to the glass industry and lead to efforts to understand and predict corrosion as a function of furnace conditions. The replacement of air with oxygen, although attractive from a number of standpoints,[5] causes crown corrosion rates to increase by as much as a factor of two, reducing furnace lifetimes to five years or less in some cases. Numerous qualitative investigations using sophisticated analytical methods, including works by Paskocimas et al.,[6] Kotacska and Cooper,[7] Boillet et al.,[8, 9] Faber and Verheijen,[10] Godard et al.,[11] and Duvierre et al.,[12] show that many of the features of silica corrosion in air-fired furnaces are also seen under oxy-fuel conditions. For the most part, these investigators reached the same conclusions concerning strategies for reducing corrosion; however, none attempted to quantitatively predict corrosion rates. The accelerated degradation of the refractory front face is the principal symptom, rather than ratholing, as was the case in air-fired furnaces. Qualitatively, the cause of the faster corrosion seems easy to understand: the increased concentration of oxygen in the furnace produces much higher partial pressures of water-vapor (up to) 0.67 for stoichiometric methane/oxygen—0.65 has been observed—vs. 0.18 for an air-fired furnace),[13] leading to higher gas-phase alkali concentrations and thus an accelerated rate of Reaction (4-1).

In spite of these extensive efforts, there have been very few attempts to develop quantitative models that can predict corrosion rates as a function of furnace conditions. Wu and Kobayashi modeled crown corrosion in the mass-transport limit (i.e., assuming that corrosion is limited by the rate of vapor-phase transport of NaOH(g) to the refractory surface), which represents the upper limit for the process.[14] Their model uses computational fluid dynamics (CFD) to simulate the three-dimensional combustion processes and to assess the effects of burner elevation on alkali volatilization. Only relative crown corrosion rates were reported, so it cannot be determined whether the mass-transport limit is in fact close to observed corrosion rates. Most details of the model are not provided, making it difficult to make direct comparisons with other models. Misra et al. developed a similar model, again using CFD calculations to predict velocity and temperature fields in the combustion space over the glass.[15] Simplified chemical reactions were also employed, using empirically estimated rate constants. The results are evidently in quantitative agreement with observation, although no direct comparisons are shown. The authors also point out the need to include thermodynamics of the equilibrium between the combustion gases and liquid-phase corrosion products. While the success of this effort is tantalizing, the lack of specifics again inhibits further development; for example, none of the rate constants used to model the corrosion reactions are reported. Allendorf and Spear recently established thermodynamic data for the variable-composition sodium-silicate products and predicted equilibrium NaOH(g) concentrations for air- and oxy-fired conditions as a function of temperature.[16] These results were used to identify concentration and temperature regimes under which silica corrosion is thermodynamically favorable. Walsh et al. made further use of these data and earlier approximations thereof[17] to calculate corrosion rates limited by gas-phase transport of NaOH in a manner very similar to that used in the present paper.[18, 19] However, none of these investigations allow firm conclusions to be drawn about which of the four processes described above is the rate-controlling step.

Quantitative measurements of furnace conditions critical to model validation, such as refractory temperature, gas-phase alkali concentrations, and actual corrosion rates, are scarce. One of the most thorough investigations is by Faber and Beerkens,[17] who measured NaOH(g) concentrations in several glass furnaces. Concentrations of 50–60 ppm in an air-fired furnace were observed (13 wt. % soda in the glass), 140–200 ppm in an oxy-fired furnace with a comparable soda-lime glass, and 220–260 ppm in an oxy-fired furnace melting soda-lime glass with 16 wt. % soda. Anecdotal NaOH(g)(g) concentrations for oxy-fired furnaces range from 100 ppm to 250 ppm; these results are consistent with measurements by Walsh *et al.* based on atomic-sodium absorption spectroscopy.[20] Faber and Beerkens also exposed refractory test samples to controlled furnace atmospheres and measured Na_2O concentration profiles as a function of temperature and distance from the hot face. They correlated these results with thermodynamic modeling that apparently accounted for the variable-composition liquid corrosion products, although the source of the thermodynamic data for these liquid products is not given, and no conclusions are drawn regarding the rate-limiting process. Finally, Tong et al. reported corrosion rates (as well as gas-phase alkali concentrations).[13] These limited studies emphasize the need for additional measurements of corrosion rates under controlled, or at least well characterized, conditions.

The objective of this work is to use analytical models to predict rates of silica corrosion by NaOH(g) that result from each of the four processes listed above and use these results to determine which is most likely to be the rate-limiting mechanism. We consider only front-face corrosion and do not deal specifically with ratholing, a mechanism for which was suggested in a previous paper.[16] However, some of the phenomena occurring during the formation of rat holes are examined here and could potentially be of value in modeling this process and other types of in-depth corrosion. Model results are compared with three types of data: 1) chemical analysis of silica refractories exposed to corrosive atmospheres in a laboratory furnace; 2) post-mortem analysis (corrosion rates and chemical analysis) of samples taken from a container-glass furnace; and 3) data reported in the literature (see above). Although this paper focuses on silica, the analysis of the various corrosion processes that could occur is applicable to any refractory and can be made quantitative if thermodynamic data are available describing the equilibrium between a gas-phase corrosive species and the refractory of interest. It is also likely that the qualitative conclusions of this analysis can be directly extended to corrosion of silica by KOH(g), whose equilibrium with silica is similar to that of NaOH(g).[16] However, little is known about KOH(g) concentrations or about the presence of potassium-containing corrosion products within silica bricks, so we will not discuss this further.

Phenomenology of Corrosion

Corrosion of silica will occur at the exposed crown surface whenever the gas-phase concentration of NaOH(g) exceeds the value associated with local equilibrium between the gas, the solid SiO_2, and the sodium-containing liquid reaction product (Reaction 4-1).[16] The surface corrosion process thus involves transport of NaOH(g) from the furnace atmosphere to refractory surfaces where these reactants combine to form a sodium silicate product. Since the silica reaction product is a high-viscosity liquid at typical furnace conditions, some of it may be drawn into the pores of the brick by capillary suction or drip from the surface, but at least part of it remains as a thin layer that coats the external surface of the brick. Thus, as illustrated schematically in Figure 4-1, the quasi-steady surface corrosion process may be viewed as a series of distinct steps:

(1) transport of NaOH(g) vapor from the furnace gas to the external surface of the liquid product layer that coats the crown surface.

(2) formation of Na_2O at the external surface of the liquid product layer.

(3) diffusion of Na_2O through the liquid product layer to the SiO_2 surface.

(4) dissolution of silica to form a sodium-rich silicate at the interface between the liquid product and the unreacted silica grains.

(5) transport of liquid reaction product from the reaction surface either by suction into the porous bricks or by dripping or flowing away.

Although the corrosion rate may be limited by any one of the steps enumerated above or any combination thereof, we begin by addressing each of them separately. After first discussing gas-phase transport, Step (1), we briefly address the issue of kinetic limitations in Steps (2) and (4) above by comparing equilibrium calculations with experimental observations of Na_2O content in the silicate corrosion product. This is followed by analysis of the remaining transport processes, diffusion through the liquid product layer and transport of the liquid silicate by capillary suction, Steps (3) and (5) respectively.

Vapor Phase Transport of NaOH(g) to Crown Surface

The recession rate of the brick face, d*l*/d*t*, is equal to the areal reaction rate of SiO_2, $\dot{n}_{SiO_2}$ (moles/m^2/s), divided by the molar density of SiO_2 in the unreacted brick, ρ_l. In addition, the number of moles of SiO_2 eroded by one mole of NaOH(g) is $(1\text{-}x)/x/2$ where x is the mole fraction of Na_2O in the melt and the factor of two accounts for the fact that two moles of NaOH(g) are reacted to form each mole of Na_2O. Thus, the recession rate, d*l*/d*t*, may be written as follows in terms of the reaction rate of the NaOH(g), $\dot{n}_{NaOH}$.

$$\frac{dl}{dt} = \frac{\dot{n}_{SiO_2}}{\rho_{SiO_2}} = \left(\frac{1-x}{2x}\right)\frac{\dot{n}_{NaOH}}{\rho_{SiO_2}} \tag{4-1}$$

In a quasisteady process, the reaction rate of the sodium must be in balance with the transport of NaOH(g) from the furnace gas to the refractory surface. The latter of these may be expressed as the rate of diffusion through a gas boundary layer having a mean thickness, $\delta_g = L/Sh$, where L is the length of the flow path over the surface and Sh is the Sherwood number.

$$\left(\dot{n}_{NaOH}\right)_{reaction} = \left(\dot{n}_{NaOH}\right)_{transport} = \rho_g \Delta X \frac{D}{\delta_g} = \rho_g \Delta X \, Sh \frac{D}{L} \tag{4-2}$$

Here ρ_g is the molar density of the furnace gas, D is the gas-phase diffusivity of the NaOH(g), L is the length scale of the furnace, and ΔX is the difference in NaOH(g) concentration (mole fraction) across the gas phase boundary layer adjacent to the crown face.

$$\Delta X = X_{amb} - X_{g,l} \approx X_{amb} - X_{eq} \tag{4-3}$$

In general, ΔX is the difference between the ambient mole fraction outside the boundary layer, X_{amb}, and that immediately adjacent to the gas-liquid interface, $X_{g,l}$, on the crown surface. Both of these quantities may vary considerably over the crown. If there are no rate limitations imposed by reaction kinetics or by diffusion through the liquid product layer, the NaOH(g) concentration in the gas immediately adjacent to the melt should be equal to the equilibrium concentrations, X_{eq}, displayed in Figure 4-2. Corrosion occurs whenever $X_{amb} > X_{eq}$, and the resulting corrosion rate is proportional to $\Delta X = X_{amb} - X_{eq}$.

$$\frac{dl}{dt} = \frac{\rho_{gas}}{\rho_{SiO_2}} \Delta X \; Sh \frac{D}{L}\left(\frac{1-x}{2x}\right) \tag{4-4}$$

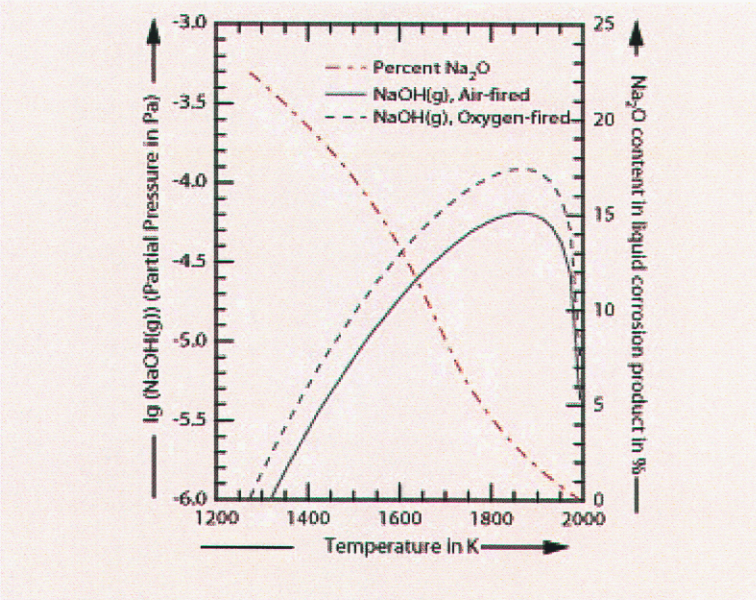

Figure 4-2. Partial pressure of NaOH(g) in equilibrium with silica as a function of temperature under oxy-fuel and air-fuel conditions. In both cases, O_2/CH_4 mole fraction = 2.05 and the total pressure is 1 atm. Also shown is the equilibrium concentration of Na_2O dissolved in the liquid-phase corrosion product as a function of temperature. Data are taken from Allendorf and Spear.[16]

The Sherwood number, Sh, may be interpreted either as a ratio of length scales, L/δ_g, or as the ratio of the actual transport through the boundary layer to that which would occur by diffusion through the length scale, L. Sh is much greater than unity in most applications. Three different models are used to estimate the magnitude of the Sherwood number: (i) laminar flow over a flat surface, (ii) turbulent flow over a flat surface, and (iii) analysis of numerical CFD results (see Appendix A). The well known laminar relation and the Coburn formula for turbulent flow of a gas (Schmidt number near unity) depend on the Reynolds number, Re, as indicated below. [21]

$$Sh_{lam} = 0.66\,\mathrm{Re}^{0.5} \qquad Sh_{turb} = 0.037\,\mathrm{Re}^{0.8} \qquad \mathrm{Re} = \frac{\hat{\rho}_g U L}{\mu_g} \qquad \text{(4-5a,b, c)}$$

Here U is the gas speed adjacent to the surface, μ is the gas viscosity, and $\hat{\rho}_g = \overline{M}\rho_g$ is the mass density based on the mean molecular weight, $\overline{M}$. The third estimate of Sh is derived from CFD contour plots of the gas speed (~1-2 m/s for oxy-fuel) adjacent to the crown as well as corresponding contours of the friction velocity, u^*. The latter quantity is a direct indication of the shear stress, τ, on the adjacent crown surface and is, thus, related to the friction factor, f.

$$u^* = \sqrt{\frac{\tau}{\hat{\rho}_g}} \qquad f = \frac{2\tau}{\hat{\rho}_g U^2} \qquad \text{(4-6a, b)}$$

Further, by the Reynolds analogy between mass and momentum transfer, [21] the friction factor is related to the mass flux, j_D, and mass transfer coefficient, h_D, which are simply related to the Sherwood number and the Schmidt number (Sc is roughly unity for gases) to obtain the needed relationship between the Sherwood number and the U and u^* values from the CFD model.

$$j_D = \frac{f}{2} = \frac{h_D}{U} Sc^{2/3} \qquad Sh = h_D \frac{L}{D} \qquad Sh_{fric} = \left(\frac{u^*}{U}\right)^2 \frac{UL}{D} \qquad \text{(4-7a, b, c)}$$

The gas density, viscosity, and diffusivity appearing in the above formulas are evaluated using the ideal gas law, the Sutherland formula,[22] and a well known approximation derived from the molecular theory of gasses.[23]

$$\rho_g = \frac{P}{RT} \qquad \frac{\mu}{\mu_o} = \left(\frac{T}{T_o}\right)^{1/2} \qquad D = \frac{2.6 \cdot 10^{-22}}{P\sigma_{12}^2} \sqrt{\frac{T^3}{m_{12}}} \qquad \text{(4-8a, b, c)}$$

Here, P and T are the gas pressure and temperature, R is the gas constant, and T_o is the temperature corresponding to the reference value of the viscosity, μ_0. The mean molecular weight and diameter appearing in Equation (4-8c) are respectively computed from those of the diffusing species and the bulk gas mixture as $m_{12} = 2m_1m_2/(m_1 + m_2)$ and $\sigma_{12} = (\sigma_1 + \sigma_2)/2$. Based on the preceding analytical relationships and values of X_{eq} and x displayed earlier in Figure 4-2, the recession rate can now be evaluated for typical furnace conditions.

Figure 4-3 shows computed recession rates versus crown temperature for various NaOH(g) concentrations in an oxy-fuel furnace having an H_2O concentration of 65%. Recession rates indicated by solid lines utilize the turbulent flow estimate of the Sherwood number. Comparative estimates based on laminar flow (dotted) and the CFD friction velocities (chain-dotted) are shown for NaOH(g) concentrations of 50 and 150 ppm. In these and all other cases the analytical results for laminar and turbulent flow differ by less than 30%, mainly because the Reynolds number of about 30,000 is transitional, on the borderline between laminar and turbulent flow. The estimates based on the CFD friction velocities are about twice as great, perhaps because they better reflect the furnace-scale turbulence induced by the burner jets.

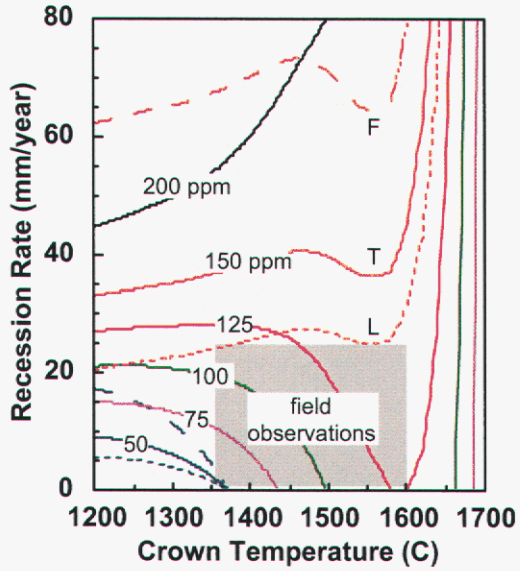

Figure 4-3. Computed recession rates for oxy-fuel combustion. Gas velocity and flow path length are *U*=1.5 m/s and *L*=5 m. Mole fraction of NaOH(g) in furnace gas is taken at 50, 75, 100, 125, 150, and 200 ppm. Solid lines indicate results for turbulent flow (T) model. Dotted and chain-dotted lines shown only for 150 and 50 ppm indicate results for laminar (L) and friction-based (F) models of mass transfer rate. Shaded box represents approximate range of field observations.

The most important conclusion to be drawn from Figure 4-3 is that computed recession rates for large but credible NaOH(g) concentrations of 150–200 ppm are generally greater than those observed in oxygen/fuel furnaces. For example, at a crown temperature of 1550 °C, concentrations of 150–200 ppm produce computed recession rates of 40–100 mm/year (60–150 mm/yr based on CFD friction) as compared with anecdotal observations of about 25 mm/year (although a value much higher than this – 100 mm/yr – has been reported[10]). This rate (25 mm/yr) corresponds to the top of the shaded box at the bottom of the plot; the sides of the box roughly indicate the typical range of crown temperatures, 1350–1650 °C. The computed recession rates would be consistent with these observations if the NaOH(g) concentration is no greater than 125 ppm. One report we are aware of, however, indicates that NaOH(g) concentrations as high as 350–400 ppm can be produced by unfavorable burner orientation in an oxy-fuel furnace.[24] Such large concentrations yield calculated recession rates greatly exceeding even the (presumably atypical) 100 mm/year observed by Faber and Verheijen in a low-temperature area above the batching area.[10]

The gas velocity and length scale used to construct Figure 4-3 are $U = 1.5$ m/s and $L = 5$ based on the CFD results in the Appendix. The ratio of friction velocity to mean velocity is taken at an average value of $u^*/U \sim 0.12$ based on a CFD simulation having a mean speed of ~1 m/s near the crown. That case is typical of low-momentum oxygen/fuel burners, whereas high-momentum oxygen/fuel burners produce mean speeds about twice as large. For both low and high momentum burners the maximum speeds adjacent to the crown are about twice the mean. So it is expected that maximum recession rates would be 40% to 100% greater than the mean values shown in the plot.

The recession rate may either increase or decrease with temperature, depending on the temperature range and the ambient NaOH(g) mole fraction. The increase takes precedence for NaOH(g) concentrations greater than about 150 ppm, as apparent in Figure 4-3. The increase of recession with temperature is a consequence of the decreasing mole fraction of Na_2O(g) in the melt. As seen earlier in Figure 4-2, the equilibrium mole fraction of Na_2O in the corrosion product, x, decreases from about 10% to less than 1%, as the temperature increases from 1200 °C to 1600 °C. Thus, the amount of SiO_2 removed by each mole of NaOH(g) increases by a factor of ten. Accordingly, this liquid phase mole fraction, x, appears in the denominator of the expression for the recession rate in Equation (4-4).

For smaller values of the ambient NaOH(g) concentration, $X < 125$ ppm in Figure 4-3, the recession rate decreases with temperature up to a temperature of about 1600 °C. This results from the increase of the equilibrium gas-phase concentration, X_{eq}, with temperature, as illustrated earlier in Figure 4-2. The increase in X_{eq} helps to reduce the concentration difference $\Delta X = X - X_{eq}$, that drives the diffusive flux of NaOH(g) through the boundary layer to the crown surface. Note that ΔX appears in the numerator of Equation (4-4). However, this downward trend reverses above 1600 °C because the equilibrium vapor phase concentration then decreases with temperature. At high temperatures this increase in ΔX reinforces the decreasing liquid-phase mole fraction to produce the extremely large recession rates seen on the right side of Figure 4-3. These same trends are seen in the results of Figure 4-4 which apply to air-fuel combustion.

Figure 4-4 compares computed and observed surface recession rates for air-fuel combustion. It is very similar to the earlier Figure 4-3 for oxygen-fuel combustion and, as before, computed recession rates are somewhat greater than those generally observed. For air-fuel combustion, the computed recession rate for 75 ppm NaOH(g) is around 20 mm/year. Well-insulated crowns of air-fuel furnaces usually recede much more slowly than this. For comparison, Wereszczak et al. report recession of only 6 mm in 10 years of exposure at 1600 °C in a soda-lime-silica float-glass furnace and 13 mm recession in 6.5 years at 1600 °C in a TV-panel glass furnace. [25] Thus, we take 2.5 mm/year (~25 mm/10 years) as a typical air-fuel recession rate corresponding to the top of the gray box in Figure 4-4. Faber and Verheijen report considerably greater recession rates, ranging from 5–10 mm year at 1530–1580 °C, but the larger value is for a brick located over the batch area where NaOH(g) concentrations are expected to be greatest, probably greater than 75 ppm.[10] For comparison, the computed recession rate for 100 ppm NaOH(g) is around 40 mm/year, about four times greater than the observation. Moreover, the calculations in Figure 4-4 utilizes a mean speed of only 1.5 m/s, which is about a factor of two smaller than those measured by Webb near the crown of an air-fuel furnace. [26] Use of a larger velocity would increase the disparity between observed and computed recession rates.

Although computed recession rates based on gas-phase transport appear to exceed observations, the results are very sensitive to NaOH concentrations and crown surface temperature, which are not accurately known. Moreover, it is very encouraging to see that computed recession rates do decrease with crown temperature for sufficiently small values of the ambient NaOH(g) concentration. This result is consistent with industry experience showing that elevation of the crown temperature by addition of thermal insulation to the backside of the refractory greatly reduces corrosion. Thus, it is likely that the operative physics are correctly modeled, but that some of the inputs to the analysis may be inaccurate. For example, NaOH(g) concentrations in field operations may be a factor of two less than the conventional estimates of ~200 ppm for oxy-fuel and 40–80 ppm for air-fuel. Alternatively, our current estimates of NaOH(g) equilibrium values, $X_{eq}(T)$, may be low by 20-30%. Another possibility is that our estimates of the Na_2O concentration in the melt, $x_{eq}(T)$, are too low. Any of these explanations or some combination thereof could bring the predictions into better agreement with the data. Another possibility is that some other transport or kinetic limitation is controlling the corrosion rate. For that reason we explore some alternative rate-limiting mechanisms.

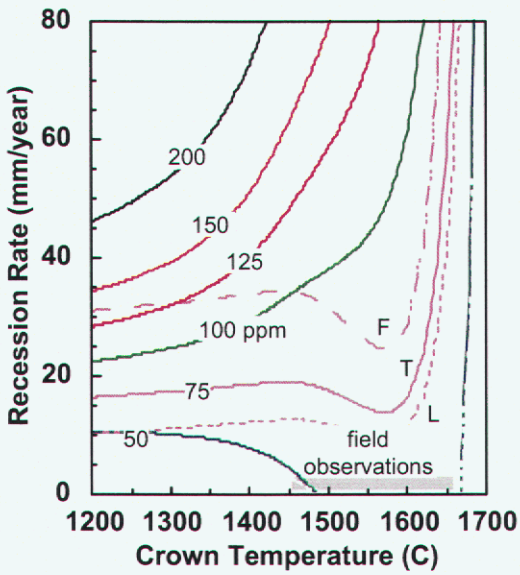

Figure 4-4. Computed recession rates for air-fuel combustion. Gas velocity and flow path length are *U* =1.5 m/s and *L*=5 m, the same as in the preceding plot for oxy/fuel combustion. The difference in recession rates between air and oxygen supported combustion is caused mainly by the difference in equilibrium thermodynamics resulting from different H_2O concentrations in the furnace gas. Solid lines indicate results for turbulent flow (T) model. Dotted and chain-dotted lines shown only for 75 ppm indicate results for laminar (L) and friction-based (F) models of mass transfer rate.

Kinetics of Reaction at Liquid/Grain Interface

In general, concentration differences for sodium-containing species are needed to drive the reactions occurring on both sides of the liquid product layer as well as the sodium transport through both the gas and the liquid. However, one of these processes is often much slower than the others and so consumes most of the available difference between the sodium concentration in the ambient gas and that associated with full equilibrium between the solid, liquid, and gas at a given temperature. In the analysis of the preceding section it is assumed that the reaction kinetics are fast and the diffusivity of Na_2O in the liquid is large. Under these conditions the liquid product layer will be nearly in equilibrium with the solid SiO_2 ($x \sim x_{eq}$) and with the gas immediately adjacent to the liquid. All of the NaOH concentration difference between the ambient gas and the gas immediately adjacent to the liquid is then available to drive the transport through the boundary layer.

To assess the influence of reaction kinetics let us accept that the Na_2O diffusivity is large (as will be demonstrated in the next section) and suppose that the reaction kinetics are slow. If this is the case, the silicate liquid layer would approach equilibrium with the ambient gas phase, and the Na_2O concentration in the liquid adjacent to the solid SiO_2 grains would exceed the value corresponding to equilibrium with the solid ($x > x_{eq}$); this concentration difference drives the silica dissolution reaction. The resulting increase in the sodium content of the melt, x, and the consequent reduction in the gas-phase concentration gradient, $\Delta X/\delta_g$, would then reduce the recession rate computed from Equation (4-4), bringing the predictions into better agreement with field observations. This hypothesis can be tested by comparing measured values of the Na_2O mole fraction in the silicate corrosion product with those predicted by modeling the equilibrium thermodynamics.

To make this comparison, the equilibrium Na_2O mole fraction in the sodium-containing liquid corrosion product was calculated as a function of the vapor-phase NaOH(g) mole fraction for two cases, using the ChemSage program[27, 28] and the SiO_2/Na_2O thermochemistry reported earlier by Allendorf and Spear.[16] In the first case, calculations for full equilibrium were performed (i.e., gas and liquid in equilibrium with crystalline silica). In the second case, the formation of stoichiometric crystalline phases (including all forms of SiO_2) was suppressed. This is the equivalent of placing an infinite kinetic barrier to the reaction of either the gas or the liquid with the silica grains. The Na_2O concentration was then determined at two fixed temperatures (1883 K and 1765 K) corresponding to specific experimental data (see below) and over a range of input NaOH(g) activities (the activity is fixed so that the NaOH(g) concentration does not vary). The input composition for these calculations in all cases simulates an oxy-fuel combustion atmosphere (O_2/CH_4 mole ratio = 2.05, yielding an H_2O mole fraction ~0.65).

The results in Figure 4-5 show that for a gas/liquid partial equilibrium, the amount of Na_2O in the liquid is often much higher than that expected at full equilibrium. For example, at 1765 K, full equilibrium predicts that the liquid product will contain 5.5% Na_2O, while gas/liquid partial equilibrium predicts values ranging from 5.6% at 100 ppm NaOH(g) to 18.1 at 200 ppm NaOH(g). Similarly, at 1883 K, full equilibrium produces a liquid product with 2.1% Na_2O, while gas/liquid partial equilibrium gives 1.6% at 100 ppm NaOH(g) and 9.5% at 200 ppm. Note that each point on the full equilibrium (dashed) curve in Figure 4-5 corresponds to a particular temperature; this curve is equivalent to the oxy-fuel NaOH(g) vs. temperature curve in Figure 4-2, but rotated clockwise by ninety degrees. Note that these Na_2O mole fraction exceeds the full equilibrium value ($x(T, X_{NaOH(g)}) > x_{eq}(T)$) whenever the gas-phase NaOH(g) concentration exceeds its value at full equilibrium ($X > X_{eq}(T)$).

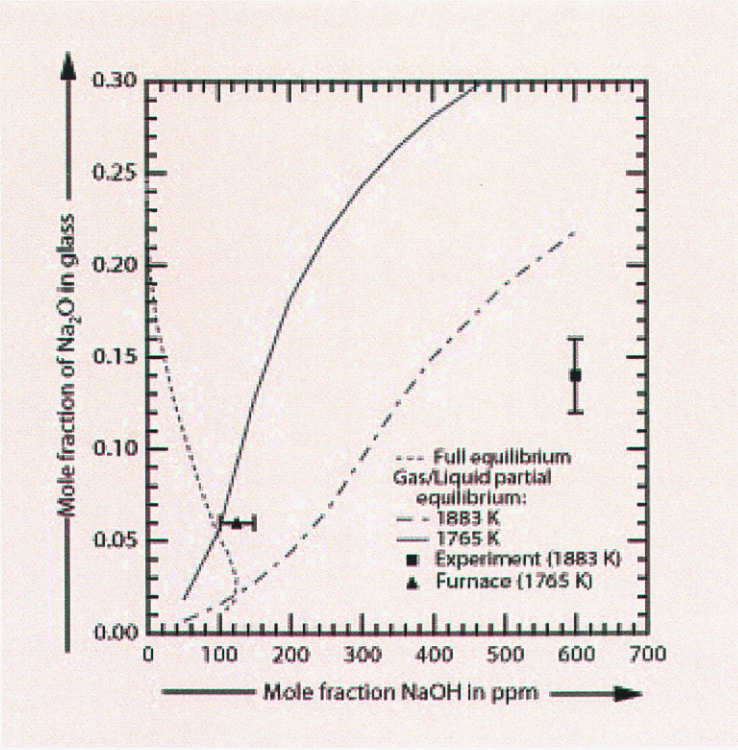

Figure 4-5. Comparison of measured and predicted concentrations of Na_2O in liquid corrosion product. Dashed line at left is a prediction based on complete equilibrium (gas + liquid corrosion product + silica). Solid and dash-dot lines sloping up to the right are predictions based on equilibrium between the liquid corrosion product and furnace gases only (i.e., no solid phases are allowed to form).

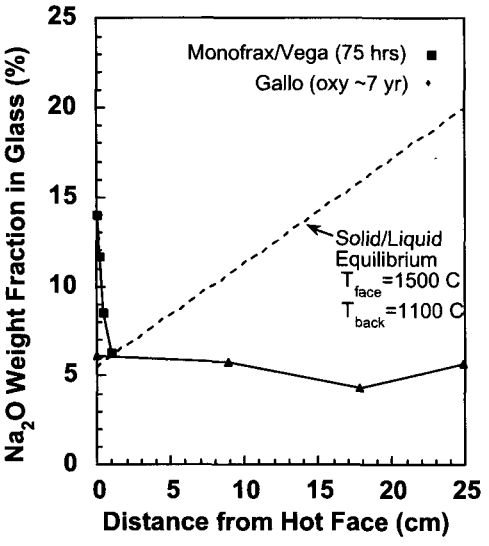

Figure 4-6. Na_2O content of glass corrosion product versus depth into worn silica bricks. Measured data (symbols) are from bricks extracted from a Gallo furnace (Moore, Neufeld and Wolfe;[29] Wolfe[56]) and from samples exposed in a Monofrax test furnace (Gupta;[33] Wolfe [52]). Na mole fraction in glass at Gallo brick surface is consistent with predictions (dashed line) based on equilibrium thermodynamics, but the data does not show the expected increase of Na content in the cooler brick interior. Na content at Monofrax brick surface exceeds prediction, perhaps because of relatively short duration of tests; interior Na content is consistent with Gallo data and with computed equilibrium.

These predictions can be compared with measured Na_2O concentrations found in post-mortem analyses of refractory samples recovered from glass-melting furnaces. We discuss one example in detail (shown in Figures 4-5 and 4-6 by filled triangles), since we are fortunate to have fairly complete information concerning furnace conditions and the sample properties provided by Moore et al.[29] Other data in the literature are in qualitative agreement, however (see below). The point shown in Figure 4-5 represents the Na_2O concentration (obtained by energy dispersive spectroscopy, EDS) of an amorphous phase that fills the pores of a brick[††] salvaged from an oxy-fuel container-glass furnace producing soda-lime glass and operated for seven years (referred to below as the Moore et al. sample).[29] The temperature of the brick, 1765 K (1492 °C), is assumed to be the same as that measured at a nearby breast-wall location using optical pyrometry.[30] As seen in Figure 4-6, the measured Na_2O content of the glass within the brick pores is 5.5 ± 0.5 wt% through most of the 25-cm thickness of the remaining brick (the length of an unused brick was 38.1 cm). This measurement is in good agreement with the computed full equilibrium value (also 5.5%) corresponding to a brick surface temperature of 1765 K, suggesting that the rate of reaction between Na_2O and the silica grains is not rate limiting. In contrast, gas-liquid partial equilibrium yields a much higher Na_2O concentration. Assuming an NaOH(g) concentration of 125 ± 25 ppm based on the measurements of Walsh et al.,[20] partial equilibrium predicts an Na_2O concentration in the liquid product of 9.0 mol %.

[††] Gen-Sil (RHI Refractories). Analysis of unused brick (weight percent): 95.9%, SiO_2, 2.8% CaO, 0.8% Fe_2O_3. Sample estimated to have come from approximately 5 m on centerline from the batch charger end wall of the furnace. For additional details on the furnace configuration, see Ref. 18.

Since the Na_2O concentrations obtained from the post-mortem analysis of the Gallo brick are fairly consistent with full equilibrium expectations, it appears that chemical-kinetic limitations are not limiting the long-term corrosion rates of silica bricks. An important qualification must be raised, however: the predicted equilibrium Na_2O concentration is rather sensitive to temperature, decreasing as temperature increases. For example, increasing the temperature 50 K from 1765 K to 1815 K decreases the predicted Na_2O concentration at full equilibrium from 5.5 to 3.9 mol %. This raises the possibility that the measured Na_2O concentration could exceed that at full equilibrium, suggesting that a moderate kinetic limitation could exist. Since the temperature used in the calculations actually corresponds to the breast wall of the furnace (albeit at the same distance down the furnace axis as the sample taken from the crown), an error of 50 K or even more does not seem unreasonable).

It is further seen in Figure 4-6 that the measured Na_2O content in the cooler interior and back side of the Moore et al. sample (~5.5%) is well below the predicted equilibrium Na_2O content (dotted line, Figure 4-6). The dotted line is based on an estimated back side temperature of around 1400 K, for which full equilibrium predicts 19% Na_2O in the liquid product (see Figure 4-2), in contrast with 5.5% at the much hotter front surface. Since we believe that most of the glass is formed at the hot face and drawn into the brick pores (as explained later), it appears that a kinetic limitation may prevent the precipitation of silica from the liquid corrosion product so that its Na_2O concentration cannot increase to the equilibrium value corresponding to the cool interior. This is consistent with the fact that crystallization of silica from a melt is very difficult,[31, 32] particularly at the temperatures encountered here (< 1738 K) in which tridymite is the thermodynamically favored phase. There is no evidence to indicate, however, that this kinetic limitation, if it in fact exists, limits the rate of front-surface corrosion.

Data from Faber and Verheijen (FV) further supports the hypothesis that reaction kinetics do not limit long-term furnace corrosion rates. FV report measurements of Na_2O concentration in corroded silica samples,[10] although the sample temperature during furnace operation is not given. Thus, we cannot perform equilibrium predictions corresponding to the operating conditions of the furnace. Nevertheless, the results are qualitatively consistent, showing a relatively constant Na_2O weight fraction throughout a 30-cm portion of the brick. If a porosity of 20% (typical of porous silica refractories) is assumed, the FV weight fractions convert to mole fractions (2.5–4.4 mol %) that are comparable to those corresponding to the Moore et al. sample.[29]

In contrast to the results of these long-term corrosion processes, laboratory measurements suggest that chemical-kinetic rate limitations may appear under experimental conditions in which the time scales are necessarily shorter than typical furnace campaigns. The square symbol in Figure 4-6 represents an EDS measurement of Na_2O content in an amorphous phase similar to the Moore et al. sample, but found within the pores of a silica refractory sample exposed to a controlled atmosphere containing a gas mixture intended to simulate oxy-fuel conditions in a laboratory-scale furnace.[‡‡]

[‡‡] Vega (RHI Refractories). Analysis of unused brick (weight percent): 96.4%, SiO_2, 2.9% CaO, 0.5% Fe_2O_3. Tests performed in laboratory furnace at Monofrax Inc. (Falconer, NY). Combustion gases are simulated by burning a stoichiometric natural gas/oxygen mixture (4.25 slpm total flow rate) in a separate chamber. Hot combustion products from this chamber then flow into an insulated, isothermal chamber containing a bath of molten glass. In this case, soda-lime cullet with the following composition (wt. %) typical of float glass was used: 72.7% SiO_2, 13.92% Na_2O, 0.5% K_2O, 8.6% CaO, 4.21% MgO. Refractory samples (5 cm x 5 cm x 11 cm) were suspended above the glass bath on slabs of α,β-alumina. NaOH concentrations were determined using extractive sampling and

The atmosphere contained 640 ± 65 ppm NaOH(g) and the test was conducted at 1883 K (1610 °C) for 75 hours.[33] The measured Na_2O concentration of ~14% lies roughly midway between the values of 2.5% and 23% that, respectively, apply for full equilibrium and gas/liquid partial equilibrium with 640 ppm NaOH(g). In this case, the liquid product is clearly not in equilibrium with crystalline SiO_2, since the Na_2O content is nearly six times greater than that predicted for full equilibrium. If such conditions persisted over extended periods of time in a full-scale furnace, the deviation from equilibrium would reduce the computed surface recession rate by a factor of about six, since the amount of NaOH(g) required to remove each mole of SiO_2 increases by that factor. However, it is seen in Figure 4-6 that the glass samples from the interior of the (25 mm x 25 mm cross section) test samples have much lower Na_2O concentrations (~6%) more typical of the Gallo measurements and the equilibrium calculations.

In summary, the available measurements suggest that the liquid corrosion product produced at the surface of silica bricks under typical furnace operating conditions is reasonably consistent with predictions based on a full equilibrium between silica in the crown and the furnace gases immediately adjacent to it. However, interior Na_2O concentrations are considerably less than equilibrium values, suggesting a kinetic barrier to tridymite precipitation. A corollary to these conclusions is that laboratory experiments, even when they attempt to reproduce realistic furnace atmospheres, may not produce corrosion products whose composition mimics that found from post-mortem samples because the duration of such tests is typically much shorter than the lifetime of a refractory in a full-scale furnace.

Diffusion of Na_2O through the Liquid Product Layer

Na_2O formed at the gas/liquid interface must be transported through the liquid product layer on the brick face to the liquid/solid contact by diffusion. Thus, in analogy with the previous analysis of gas-phase transport, the rate of recession is limited by the rate of diffusion through the liquid product layer.

$$\frac{dl}{dt} = \frac{\rho_{liq}}{\rho_{SiO_2}} \Delta x \frac{D_{Na2O}}{\delta_l} \left(\frac{1 - x_r}{2 x_r} \right) \tag{4-9}$$

Here, Δx is the difference between the Na_2O concentrations in the liquid at the gas/liquid and liquid/solid interfaces.

$$\Delta x = x_{g,l} - x_{l,s} \tag{4-10}$$

off-line wet-chemical analysis. Corroded samples were analyzed off line using scanning electron microscopy/EDS to determine the atomic composition of the corrosion products.

This difference is at its maximum when $x_{g,l}$ is in equilibrium with the furnace gas and $x_{l,s}$ is in equilibrium with the solid SiO_2. As noted earlier in Figure 4-5, $x_{l,s}$ is a function of temperature alone whereas $x_{g,l}$ is a function of temperature and NaOH concentration. The mole fraction x_r in Equation (4-9) is that of the melt being removed from the liquid layer. If the melt is dripping from the gas/liquid side of the layer, the melt being removed has a mole fraction of $x_r = x_{g,l}$ whereas the appropriate mole fraction is $x_r = x_{l,s}$ when the glass melt is being drawn into the pores of the brick. Note that in earlier discussion and in Equations (4-1) and (4-4) we did not subscript the symbol x because it had been previously assumed that the mole fraction was uniform across the liquid layer and so there was no need to distinguish the side of the layer from which the liquid was removed.

The maximum thickness of the liquid melt layer on the brick face can be estimated by application of the Rayleigh-Taylor criterion for stability of a thin film. Droplet formation is likely to occur when the thickness of the film exceeds a critical thickness defined by

$$\delta_{crit} = \left(B_n \frac{\sigma}{\Delta\rho\, g} \right)^{1/2} \approx 2 \text{ mm} \qquad (4\text{-}11)$$

where σ is the surface tension, $\Delta\rho$ is the density difference between the liquid film and the adjacent gas, g is the gravitational constant, and $B_n \sim 0.687$ is a constant determined by stability analysis.[34] A maximum stable layer thickness of 2 mm corresponds to a surface tension of 300 mN/m, typical of SiO_2 at 1500 °C. This is only a few times greater than the surface tension of water at room temperature; for that case the stability limit is slightly less that 1 mm. This layer thickness is well below the cutoff wavelength of the Kelvin-Helmholtz instability[35] that is driven by shear forces imposed by the external gas velocity of ~1 m/s, so Rayleigh-Taylor instability is the controlling consideration. The layer may, of course, be thinner than the critical thickness when most of the melt is being drawn into the brick face by capillarity or as a result of film flow down inclined portions of the crown. We will use the maximum thickness to show that diffusion through even the thickest possible layer cannot place a significant constraint on the rate of surface corrosion.

The maximum stable layer thickness is proportional to the square root of the surface tension which increases moderately with increasing temperature. For example, a temperature rise of 300 °C increases the surface tension by only 10%.[36] Increased water content in the layer reduces the surface tension, but again the changes appear moderate. An increase in water vapor mole fraction from 0 to 0.025 reduces the surface tension by only 10%.[36] Moreover, an exponential extrapolation of this measured trend to a mole fraction of 0.5 (similar to oxygen/fuel fired conditions) provides less than a factor of two total reduction in surface tension. Although some studies show a weak variation of surface tension with Na_2O content, Kucuk et al.[37] find that these variations are not statistically significant. In addition, the stability limit does not depend on viscosity; this property only affects the growth rate of disturbances that lead to droplet formation. Thus, it appears likely that the stable layer thickness will be quite similar for air- and oxygen-fired conditions and independent of layer composition.

To our knowledge the diffusivity of Na_2O in silicate melts has not been directly measured at the temperatures of interest. Nor is there data concerning the dissociation of Na_2O and the diffusivity

of all relevant ionic and molecular species. However, there is a great deal of information regarding the diffusivity of H_2O as well as Na, O, H, and OH ions. Much of this is found in the geophysical literature where there is considerable interest in silica rich magmas, and these studies appear consistent with recent measurements by Mesko and Shelby[38] for commercial float glass and TV panel glass. In general, sodium ions are known to diffuse very readily, having a diffusivity approaching 10^{-4} cm^2/s at 1600 °C.[39, 40] Oxygen species generally diffuse much slower because they bond to silicon in the glass and must diffuse from one bond to another in the silicate network. Thus, the diffusion of Na_2O is likely to be limited by diffusion of oxygen species, suggesting that estimates can be made on the basis of previous studies addressing H_2O, O, and OH.

Figure 4-7 illustrates measured diffusivities of oxygen species in glass melts within the temperature range of interest. Perhaps the oldest and best known data set, that of Moulson and Roberts,[41, 42] lies far below the bulk of the data. The other measurements for oxygen and water are relatively consistent with one another, though order of magnitude variations are seen in both sets, perhaps for reasons that differentiate the particular experiments. The data most relevant to the present study is that of Mesko and Shelby for float glass.[43] At 1600 °C their H_2O diffusivity is around 10^{-5} cm^2/s, similar to that measured for oxygen by Reid[44] and by Lesher.[45] Ignoring Moulson and Roberts, the lowest estimate of diffusivity at 1600 °C is obtained by an extrapolation of Pfeiffer's data[39] to a value of about $10^{-6}cm^2/s$, roughly tenfold less than Mesko and Shelby.

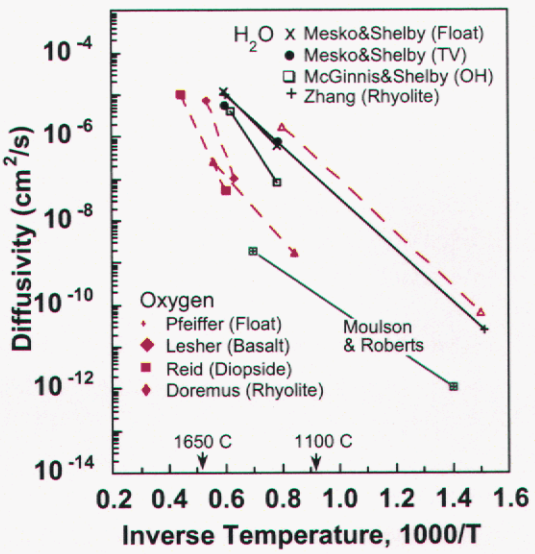

Figure 4-7. Measured diffusivities of oxygen species in silicate melts. Only the end points of the best fitting lines are shown. H_2O and O diffusivities are used to estimate the diffusivity of Na_2O through silicate melt layer on brick face. Recent data from Mesko and Shelby are most relevant to present study.[38, 43] Other sources of data include Moulson and Roberts,[42] McGinnis and Shelby,[58] Zang and Behrens,[59] Pfeiffer,[39] Lesher et al.,[45] Reid et al.,[44] and Doremus.[60]

Computed recession rates limited only by diffusion of Na_2O through a 2-mm liquid film are shown in Figure 4-8 for ambient NaOH concentrations of 80, 200, and 600 ppm. The upper and lower sets of calculations utilize the diffusivity estimates of Mesko and Shelby[43] and Pfeifer,[39] respectively. The upper set, thought to be the best estimate, is in reasonable agreement with recession rates observed by ORNL[46, 47] and Corning [48] in crucible tests. Although the chemistry of these tests[49] differs from the NaOH process that we are modeling the gas in the crucible contains high concentrations of the reactant species and the corrosion rates are very large.

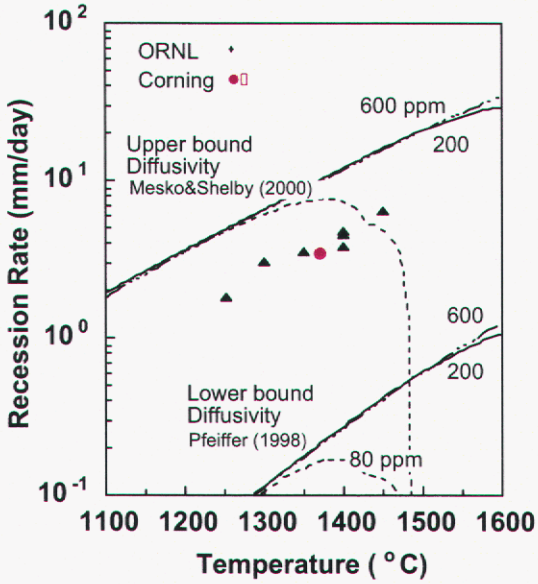

Figure 4-8. Computed recession rates limited only by Na_2O diffusion through a 2 mm silicate liquid layer on the brick face. Calculations (upper lines) based on diffusivity data of Mesko and Shelby[43] are similar to measured recession rates in crucible tests on standard silica bricks at Oak Ridge National Laboratories by Roberts and Pint[46] and at Corning by Brown, et al.[48] Diffusion limited recession rates greatly exceed those observed in field environment, even for lower bound estimates of diffusivity.

The most important conclusion to be drawn from Figure 4-8 is that diffusion of Na_2O through the liquid product layer is not a controlling consideration in full-scale furnaces. First, the fact that crucible corrosion rates are as large as those observed by ORNL implies that the upper bound estimate of diffusivity, based on the Mesko and Shelby H_2O diffusion data,[43] is substantially correct for diffusion of Na_2O in silicate melts. A smaller diffusivity could not support such high recession rates. Furthermore, based on the Mesko and Shelby diffusivity and an NaOH concentration of 100–200 ppm, maximum recession rates of 1 m/year would be attainable in the field. Since this greatly exceeds the earlier estimates based on gas phase transport, it follows that liquid phase diffusion is not the rate-controlling consideration in the corrosion process observed in the field.

The recession rates shown in Figure 4-8 are computed from Equations (4-9) and (4-10) using values of $x_{g,l}$ and $x_{l,s}$ shown in Figure 4-5. In addition it is assumed that most of the liquid corrosion product drips from the liquid layer at high reaction rates and hence $x_r = x_{g,l}$. Liquid dripping from the hot side of the liquid layer has a high sodium content and so removes fewer moles of silica for each mole of Na, as compared with the lower sodium content of the silicate on the cooler side of the liquid layer, though these differences are only significant when there is a large variation of sodium content across the liquid layer. It is somewhat surprising to see that the computed recession rates are relatively insensitive to the amount of NaOH in the vapor phase. This is because the quantity, $f(X,T)$ below, which contains all of the thermodynamic information in Equations (4-9) and (4-10) is relatively constant so long as the system is far from equilibrium.

$$f(X_{NaOH},T) = \left(x_{g,l} - x_{l,s}\right)\left(\frac{1-x_r}{2x_r}\right) \approx \left(x_{g,l} - x_{l,s}\right)\left(\frac{1-x_{g,l}}{2x_{g,l}}\right) \approx \left(\frac{1-x_{g,l}}{2}\right) \approx \frac{1}{2} \qquad (4\text{-}11)$$

The second to the last of these approximations holds whenever the NaOH concentration is well above the equilibrium value and hence $x_{l,s} << x_{g,l}$. Further since $x_{g,l} < 0.3$ for the full range of conditions shown in Figures 4-5 and 4-8, it follows that $f(X,T)$ never deviates substantially from 1/2, except in the immediate neighborhood of equilibrium. In this context, note that the predicted recession rate for 80 ppm dives abruptly to zero at a temperature of about 1480 °C where the gas approaches equilibrium with the solid.

The very comparable temperature dependence of the ORNL data[46, 47] and the calculations in Figure 4-8 suggest that liquid-phase diffusion is the controlling mechanism in their crucible tests. Further note that the slopes of most of the diffusivity data sets in Figure 4-7 are comparable, suggesting similar activation energies that are all relatively consistent with the ORNL crucible data. Gas-phase transport of reactant species is apparently not an issue in the crucible tests, as compared with float-glass furnaces, because the crucible is nearly full of undiluted reactant gases that are continually replenished. In contrast, the NaOH gas concentration is orders of magnitude smaller in full-scale furnaces, and these gases must be transported from the glass surface to the crown, resulting in much more restrictive transport limitations on the corrosion rate.

Capillary Suction of Silicate Melt into Brick Pores

The presence of silicate glass deep within porous bricks can be explained by two alternative mechanisms. The glass could be formed by chemical reaction of sodium with SiO_2 at the exposed brick face and the resulting liquid product subsequently drawn into the porous bricks, as we will argue here. Alternatively, sodium species could be transported to the brick interior where they react to form silicate glass. Some combination of these two mechanisms is also possible. However, it is unlikely that NaOH gas will have direct access to the interior of the brick since the surface pores are likely filled with silicate liquid and the brick surface is probably covered with a 1-2 mm liquid film for most of the life of the brick. NaOH can, of course, be dissolved in the liquid film to form Na_2O that is transported into the brick by liquid-phase diffusion. However since the equilibrium concentration of Na_2O in the melt increases with decreasing temperature, as apparent in Figures 4-2 and 4-6, the equilibrium concentration gradient opposes the inward transport of Na_2O.

This objection could conceivably be overcome by departure from equilibrium, but this would imply very slow reaction kinetics and the available measurements of Na_2O concentrations suggest very flat concentration profiles on the interior. For these reasons we are inclined to believe that most of the silicate liquid is formed at the surface and drawn into the brick. In support of this hypothesis we now present calculations of liquid infiltration induced by capillary suction.

Two alternative models are used compute the capillary suction of silicate liquid into a permeable brick. These may be viewed as bounding estimates as the first is based on a continuum description that emphasizes the role of the smaller pores while the second, a discrete capillary-bundle model, is dominated by the larger pores. In reality, the larger pores serve as conduits for transport of liquid that is drawn from these primary channels into surrounding pores of smaller size. So the expected behavior should lie within the bounds predicted by these two relatively simple models.

The continuum model outlined below is frequently applied to gas/liquid flows in oil fields and groundwater reservoirs.[50] Assuming for simplicity that no reactions occur on the brick interior, the mass of the liquid phase is conserved as it is transported inward, requiring that

$$\phi \rho_\ell \frac{\partial s}{\partial t} = -\frac{\partial}{\partial y}(\rho_\ell u_\ell) \tag{4-12}$$

Here, the liquid density, ρ_l, and the brick porosity, ϕ, are taken as uniform and the saturation, s, represents the fraction of the local pore volume that is occupied by liquid. The remaining pore volume contains gas. The liquid velocity, u_l, may be written in the following Darcian form

$$u_\ell = -\kappa_\ell \frac{\kappa}{\mu}\left(\frac{\partial p_\ell}{\partial y} + \rho_\ell g\right) \tag{4-13}$$

in which p_l is the liquid pressure, g is the gravitational constant, μ is the liquid viscosity, κ is the intrinsic permeability of the brick, and κ_l is the so-called relative permeability of the liquid. Lacking direct measurements of the intrinsic and relative permeabilities, we will utilize the commonly applied Karman-Cozney relationship and a relative permeability that increases as the square of the saturation (this latter variation is generally stronger than linear but weaker than cubic).[50, 51]

$$\kappa = \frac{d_p^2}{180}\frac{\phi^3}{(1-\phi)^2} \qquad \kappa_\ell = s^2 \tag{4-14}$$

Here d_p is the mean pore diameter, taken as 2 microns based on the measured pores size distribution of a Gen-Sil brick.[52] The liquid and gas pressures differ by the capillary pressure, p_c, which is related to the surface tension, σ, and the radius of curvature, r, of the gas liquid interface.

$$p_c = p_g - p_\ell \qquad p_c(s) = \frac{\sigma}{r(s)} \tag{4-15}$$

The capillary pressure decreases with increasing saturation because the radius of curvature of the gas/liquid interface increases as the pore space is progressive filled by liquid. Although it is possible to write an additional transport equation for the gas phase, this is usually unnecessary because the highly mobile gas phase generally flows so freely that the pressure variations within the gas are negligible compared to those in the liquid. Thus, we assume the gas pressure to be uniform and constant.

A single parabolic partial differential equation for the liquid saturation, $s(y,t)$, is readily obtained by combining Equations (4-9,-10,-12).

$$\phi\frac{\partial s}{\partial t} = -\kappa\frac{\partial}{\partial y}\left(\frac{\kappa_\ell}{\mu}\frac{dp_c}{ds}\frac{\partial s}{\partial y}\right) \tag{4-16}$$

Noting that the variation of capillary pressure with saturation is negative, this equation resembles the heat conduction equation except that the coefficients vary strongly with saturation and with temperature. Standard time-marching finite-difference methods are used to solve Equation (4-16) subject to a fixed saturation at the hot face of the brick, a back face which is impermeable to the liquid, and an initially dry pore space.

An alternative discrete-capillary model of liquid intrusion treats the pore space of the brick as a collection of independent capillary tubes.[50, 51] For each pore size, the instantaneous rate of intrusion, dl_{liq}/dt, is equal to the liquid speed, u_l, given by the well-known Poiseulle relationship for flow in a circular channel[53] of diameter d_p driven both by gravity and by the pressure gradient induced by capillary suction.

$$u_\ell = \frac{dl_{liq}}{dt} = -\frac{d_p^2}{36\,\mu}\frac{1}{}\left(\frac{\partial p_\ell}{\partial y} + \rho_\ell g\right) = \frac{d_p^2}{36\,\overline{\mu}}\frac{1}{}\left(\frac{p_c}{l_{liq}} - \rho_\ell g\right) \qquad (4\text{-}17)$$

Since the liquid speed along each capillary must be independent of axial position, the differential form of Equation (4-17) can be readily integrated to obtain the final algebraic form containing the mean viscosity, $\overline{\mu}$, and the overall difference in liquid pressure along the capillary, p_c. At each time step of a simulation, velocities are computed for all pore sizes in the selected pore size distribution and these are used to compute the new penetration depth for each pore. As the infiltration speed depends on the mean viscosity, $\overline{\mu}$, along the entire wetted length of a given capillary, the corresponding fluid speed is greatly reduced as the fluid advances into cooler regions of the brick. The fluid saturation at any given depth into the brick is obtained by summing the pore volumes of all of the pores that are full to that depth. A key input to this analysis is the pore size distribution indicating the fraction of the total porosity associated with each pore size.

A typical capillary pressure curve and the corresponding pore size distribution and are shown in Figure 4-9. The capillary pressure variation[52] for mercury injection measurements was adjusted to account the difference in surface tension between mercury and silicate liquids. The sample was taken from the back part of a brick that had been exposed for seven years in a Gallo oxygen/air furnace. Thus, the alterations of the pore structure are less than in other samples that were closer to the hot face. Although it is not clear how typical this brick might be, it should be useful as a guideline in demonstrating the probable liquid intrusion distance under typical operating conditions.

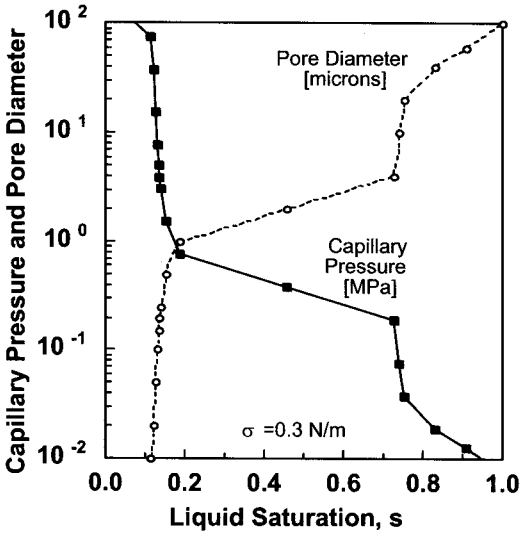

Figure 4-9. Variation of capillary pressure with liquid saturation derived from mercury injection measurements reported by Wolfe.[56] Values of the capillary pressure were measured as a function of incremental injection volume (equivalent to changes in saturation); corresponding values of pore sizes are computed. About 50% of the pore volume resides in pores having diameters of 1-4 microns; mean pore diameter is around 2 microns.

The fluid viscosity is another key input to both the transport models, continuum and discrete. The measured variation of viscosity with temperature and Na_2O mole fraction[54, 55] is well approximated by the analytical approximations (solid lines) shown in Figure 4-10. Two-parameter exponential fitting functions were developed for each of the five mole fractions displayed in the plot. Viscosities corresponding to mole fractions intermediate between these five curves are estimated by linear interpolation. Note that the viscosity increases by about four orders of magnitude as the temperature falls from the hot face (~1600 °C) to the cold face (~1100 °C), greatly reducing the intrusion speed of the glass melt as it approaches the back face.

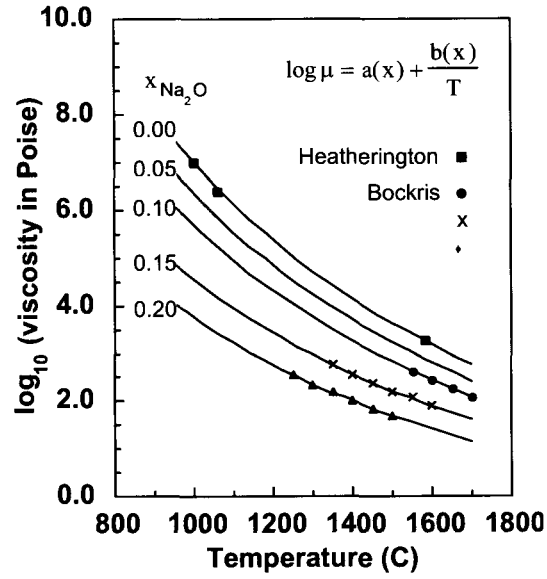

Figure 4-10. Variation of silicate liquid viscosity with temperature for Na_2O mole fractions ranging from 0.0 to 0.20. Experimental data of Heatherington and Jack[55] and Bockris et. al.[54] are well approximated by fitting functions that vary exponentially with absolute temperature.

Figure 4-11 compares the results of a typical liquid intrusion simulation with the measured intrusion in laboratory experiments by Gupta[33] and by Faber and Beerkins (FB98).[17] In both experiments the temperature and NaOH vapor concentration were around 1600 °C and 600 ppm. The samples used by Gupta were rectangular bars having a 50 mm x 50 mm cross section, while the simplified one dimensional models assumes symmetry about a midplane 25 mm from the exposed face. The FB98 samples were deeper but the infiltration depth observed after 20 hours was small enough to admit the same simplified model. Since Gupta's samples were essentially isothermal and the measured intrusion was small in the FB98 experiments, the calculation assumes a uniform brick temperature of 1600 °C.

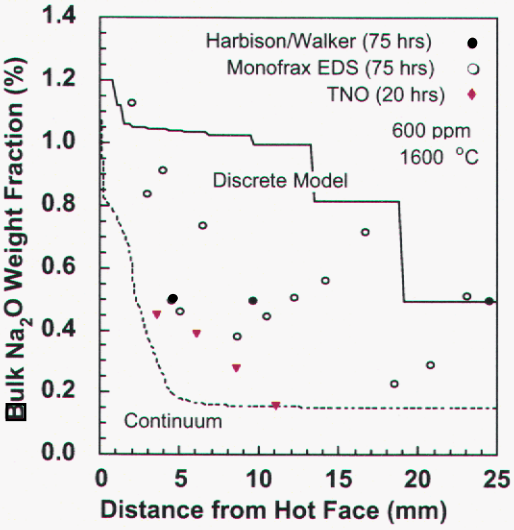

Figure 4-11. Comparison of measured (symbols) and computed liquid intrusion in a silica brick at a uniform temperature of 1600 °C. Corresponding experimental data are from a 20 hour test by Faber and Beerkens[17] and a 75 hour test reported by Gupta[33] and Wolfe.[56] Discrete and continuum model predictions are for 75 hours. Measurements are bounded by results of discrete capillary-bundle model and continuum model, suggesting that liquid can be drawn in to observed depths by capillary suction.

The two modeling results shown in Figure 4-11 bound the observations. The discrete capillary model predicts substantially greater intrusion than the continuum model. Each of the stair-steps in the discrete prediction corresponds to a particular data point in the pore size distribution shown earlier in Figure 4-9. The largest pores fill first because of their larger diameter reduces viscous friction, even though the driving capillary pressure decreases with increasing pore diameter. Conversely, the smallest pores fill first in the continuum model because dp_c/ds is greatest for low saturations corresponding to small pores. The discrete model is correct in predicting rapid intrusion into large pores, but the rate of advance is in reality curtailed by loss of fluid into the surrounding material with smaller pores. Thus, it is expected that the data should fall between the extremes of the two models.

The pore infiltration models predict the evolving distribution of fluid saturation whereas the measurements in Figures 4-11 and 4-12 indicate bulk weight fractions of Na_2O. To make the conversion, the weight of the Na_2O is computed as the product of the saturation (fraction of pore volume filled by liquid), the porosity, ϕ, the weight fraction of Na_2O in the liquid, x_r, (same as the mole fraction since molecular weights of Na_2O and SiO_2 are essentially the same), and the liquid density. The total weight includes the liquid and the SiO_2.

$$\frac{W_{Na_2O}}{W_{total}} = \frac{s\phi x_r \rho_{liq}}{s\phi\ \rho_{liq} + (1-\phi)\rho_{SiO_2}} \sim s\phi x_r \sim 0.012\, s \qquad (4\text{-}18)$$

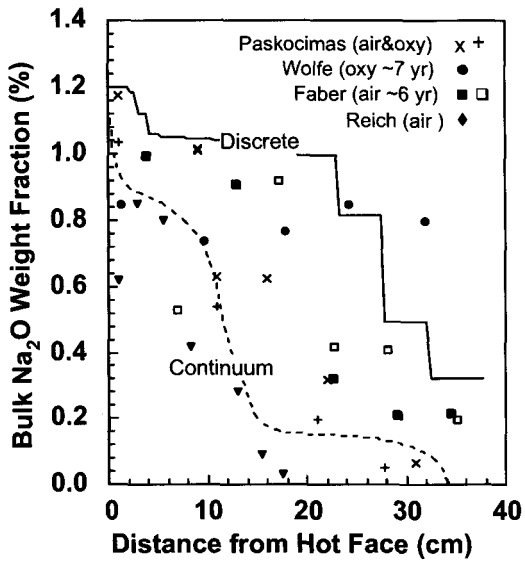

Figure 4-12. Comparison of measured (symbols) and computed Na_2O profiles in a silica brick having front and back face temperatures of 1600 °C and 1050 °C. Corresponding experimental data are from worn bricks from long campaigns examined by Reich,[1] Wolfe (Gallo furnace),[52] Faber and Verheijen[10] (open symbols 1580 °C, filled symbols 1530 °C) and Paskocimas et al.[6] (+ sidewall, x crown). Pore size distribution and viscosity used in calculation is the same as in Figures 4-9 and 4-10. Continuum (dashed line) and discrete (solid) models provide bounds on data similar to those observed for smaller scale short duration experiments.

The numerical value above is based on a typical porosity of 0.2 (20%) and the measured mole fraction of $x_r = 0.06$ (6%) in the silicate glass for both the Monofrax experiment[56] and for bricks exposed for 7 years in a Gallo oxygen/gas furnace.[52] As seen in Figure 4-6, this measured mole fraction was relatively uniform over glass samples at all depths except for higher contents of up 14% observed within 1-2 mm of the surface in the Monofrax experiments. Faber and Verheijen[10] also report 11-12% Na_2O in the glassy phases in the hot surface layers. Here we use a uniform 6% mol fraction, more typical of the interior, both in the conversion of Equation (4-18) and in calculating the viscosity of the intruding liquid. Note that a saturation of unity corresponds to a Na_2O weight fraction of 0.012 (1.2%) as seen at the brick surface in Figures 4-11 and 4-12. The agreement of the calculated bulk weight fraction with the data suggests that the measurements of Na_2O in the bulk (1.2%) and in the glass (6%) are consistent with a porosity of 20%, a reassuring check on all the data.

Figure 4-11 is analogous to Figure 4-10 except that the duration of the simulation is 7 years, the brick depth is 38 cm (15 inches), and the back face is cool enough (1150 °C) to substantially increase the fluid viscosity and retard the liquid penetration. Here the two models, discrete and continuum, are in somewhat better agreement with one another and with the measured data from a number of diverse sources. It is interesting note in Figure 4-12 that the bricks exposed to air/fuel combustion appear to have about 20% to 50% of their total porosity filled with liquid corrosion products. For a 38 cm brick with 15% to 20% porosity, this volume of liquid corresponds to a front face recession ranging from about 1 to 4 cm (3% to 12% of the length), roughly consistent with field observations. The pore volume of the Gallo brick[27] appears to be about 70% full, corresponding to a recession of about 5 cm. The observed recession was greater than this, suggesting that most of the corroded material dripped from the brick in late stages of the process.

The primary conclusion to be drawn from these comparisons of calculations with data is that capillary infiltration is the probable explanation for observed levels of Na_2O deep within worn bricks. Precise comparisons are not to be expected since the intrusion depends on the liquid and solid composition, chemical interactions, pore size distribution, capillary pressure, pore connectivity, and microstructural details that are difficult to measure and even more difficult to incorporate into brick-scale calculations that span years of operation. Fortunately, there is generally little need for such knowledge. The only observable or detrimental influence of liquid intrusion is that dripping will occur when the rate of intrusion is slower than the rate of liquid production at the surface. The onset of dripping and the drip rate could be estimated by application of the preceding models of surface recession and liquid intrusion.

CFD Methods

Gas velocities, temperature, and NaOH concentrations within furnaces are important input to the analytical models described in this paper. Since these data are often not available, it was necessary to compute them using a numerical furnace model developed by Air Liquide.[57,61] This model solves the governing Navier-Stokes, species transport, and energy-transport equations, yielding detailed three-dimensional distributions of gas velocity, temperature, and chemical composition. Calculations were first performed to provide contour plots of gas velocity and shear stress adjacent to the crown for typical cases of high-momentum and low-momentum burners.[57] A second set of calculations addresses a particularly well-documented furnace configuration, Gallo Glass Co. Tank 1 furnace, which uses oxygen to support combustion; this furnace is the source of the Moore et al. post-mortem samples discussed above.[29] It is heated by four pairs of burners that direct combustion gases from opposite sidewalls toward the furnace center.

As indicated schematically in the inset of Figure 4-13, the opposing burner jets produce a pair of counter-rotating convective rolls having inward velocities along the glass surface and outward velocities along the crown. Figure 4-13 also shows the maximum transverse or tangential velocity near the crown surface for a cross section through the furnace at an axial location that lies between burners. Each of the transverse velocities (solid symbols) shown in the plot represents the maximum transverse speed in the direction opposite to the jet at a given transverse position, x. The search begins on the crown surface and proceeds downward to the point where the horizontal velocity changes sign. Thus, these values represent speeds closer to the crown than to the glass surface. This maximum typically occurs about 0.2-0.3 m below the crown surface. The transverse speed approaches zero at the sidewalls and at the center plane of the furnace, as expected. Gas speeds along the crown are only moderately greater at cross sections taken through the burners. Although the maximum speed of the jets is on the order of 30 m/s, the induced transverse speed along the crown is only about 1-2 m/s, as seen in Figure 4-13. These gas velocities are used in Equations 4-2 through 4-7 to compute the rate of transport of sodium vapors from the furnace gas to the crown surface.

The axial speeds shown in Figure 4-13 are again maxima over elevation at a fixed transverse location, x. As with the transverse speeds, the search is only extended over elevations in the upper half of the convective roll cells induced by the jets. The axial flow is induced mainly by the flow of all the injected combustion gas toward the exhaust port located at one end of the furnace. For the most part, axial flow speeds are considerably smaller than the transverse speeds driven by the burner jets. Thus, the convective roll cells and associated transverse or tangential gas velocities are of principal importance in the furnace-scale transport of NaOH gas from the glass surface to the crown.

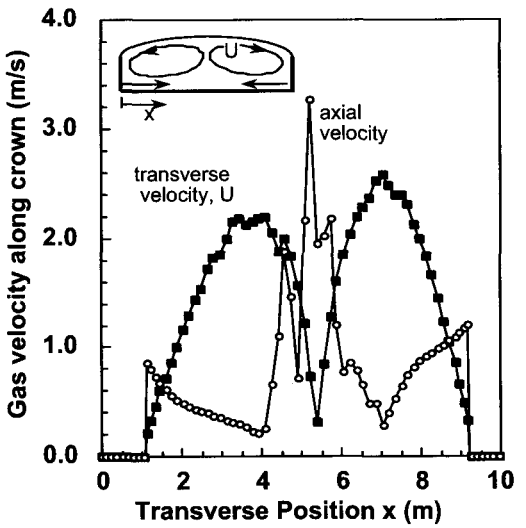

Figure 4-13. Computed transverse and axial speeds near the crown of a Gallo oxy/fuel furnace. Convective roll cells are driven by opposing combustion jets. Maximum tangential speeds typically occur about 0.2-0.3 m below the crown surface and are on the order of 1.5 m/s. Numerical values shown are obtained by post processing of numerical simulations performed by Air Liquide.

Computational Fluid Dynamic Modeling of Corrosion

It is desirable to predict the effects of furnace operating conditions on corrosion as a function of location on the crown. Due to the complexity of the heat transfer and fluid dynamics within furnaces, it is desirable to couple the front-face corrosion model developed above with a model that uses computational fluid dynamics (CFD) to determine spatial distributions of NaOH(gas), refractory temperature, and NaOH(gas) flux to the crown. To accomplish this, we used the *Athena* glass-furnace model[61] developed by Air Liquide to obtain maps of NaOH(gas) adjacent to the crown and the crown temperature, then post-processed these results through the corrosion model to predict the recession rate. Preliminary results are displayed in Figure 4-8.

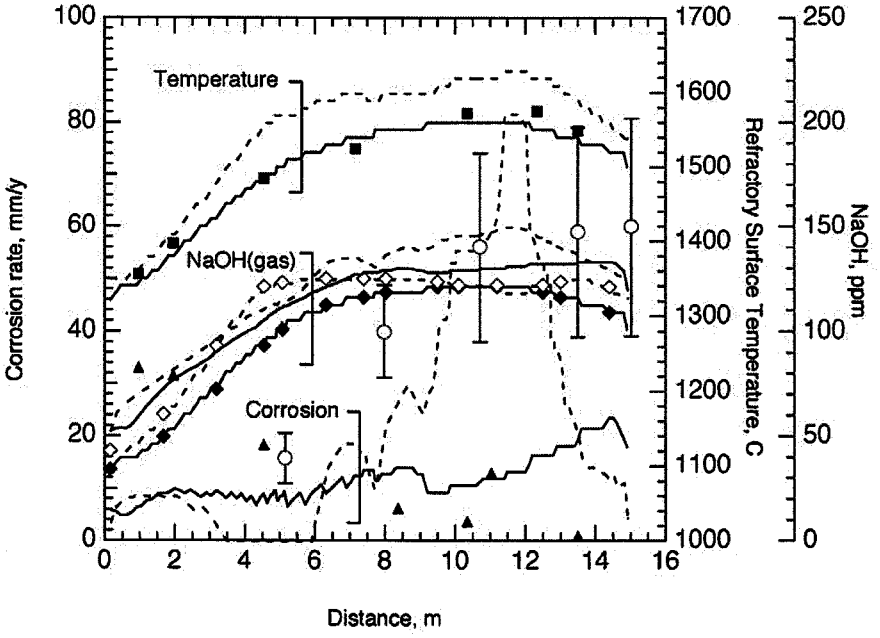

Figure 4-14. Comparison of measured temperatures, NaOH(gas) concentration, and corrosion rate in the Gallo Tank 1 furnace with model predictions. Solid lines: furnace centerline. Dashed lines: 4.1 m from the centerline, at the junction between the breast wall and the crown. Squares: measured breast wall temperatures (Ref. 62); circles: measured NaOH(gas) concentrations (Ref. 63); diamonds: NaOH(gas) predicted by equilibrium at the crown temperature; triangles: measured corrosion rates, post-mortem analysis (Ref. 62).

Predicted crown temperatures are in very good agreement with measurements made by optical pyrometry of breast wall temperatures. Initial results provided a profile whose shape was in good agreement with the measured profile,[64] but which was unrealistically hot (some temperatures were above the melting point of silica), even though the known thickness and thermal properties of the crown refractory and insulation were used. Consequently, we reduced the thickness of the insulation to bring the values of the temperature more into line with those thought to be typical in glass furnaces. This yields a temperature profile at the junction between the crown and the breast wall that agrees very well with the measured temperatures, and a centerline profile that is somewhat hotter. As will be seen below, the centerline temperatures in the ~9–13 m region are probably still too high, with the peak temperature at 1630 °C.

The predicted trend in the NaOH(gas) concentration as a function of axial position in the furnace also agrees well with the measurements of Buckley et al.[65], and even agree quantitatively in the 8–15 m portion of the furnace. They appear to be underpredicted in 0–8 m region, although there is only one data point at ~5 m for comparison. The underprediction may be a consequence of the adjustment in the furnace temperature described above, which also had the effect of lowering the glass temperature somewhat. However, it may also be due to incomplete knowledge of the precise conditions in the furnace at the time of the measurements. Later measurements performed in this furnace indicate higher NaOH(gas) concentrations in this region (~125 ppm at 1.0 m);[64] however, the burner design was changed in the interim, so it is difficult to determine at this point whether the model or the measurements are at the root of the disagreement. Importantly, in most portions of the furnace, the NaOH(gas) predicted by *Athena* exceeds that at equilibrium, which is a requirement in our model for corrosion to occur.

Combining the NaOH(gas) concentrations with the refractory temperatures and an average gas velocity of 1.5 m s^{-1} yields recession rates that are within the range of field observations for oxygen-fuel furnaces (0–30 mm/y). However, disagreement exists in specific regions of the modeled furnace environment. In the 0–5 m region, measured recession rates are a factor of 3–3.5 higher than the model predicts, even though the predicted NaOH(gas) concentrations appear to exceed the measured ones. One source of this disagreement may be the average gas velocities used in the calculation. In this furnace zone, the direction of flow along the side walls is toward the exhaust, which may result in higher than average NaOH(gas) mass transfer rates. Alternatively, high corrosion rates at the batch end of a furnace are often attributed to the presence of batch dust, the effects of which are not included in our model.

In contrast, a large peak in the centerline recession rate (dashed line, Figure 4-8) appears in the 9–13 mm region. These corrosion rates substantially exceed the measured rates in the furnace. In this case, the anomalous predictions are largely the result of the predicted crown temperature, coupled with a large difference between the NaOH(gas) predicted by the CFD code and equilibrium. The high surface temperature decreases the mole fraction of Na_2O in the corrosion product (x in Equation (4-2)), leading to increased corrosion rates, while increasing ΔX in Equation (4-2) also increases the rate. We find that the recession rate decreases by almost a factor of 2 (to 45 mm/y) if the maximum crown temperature is decreased only 30 °C to 1600 °C, an amount that seems likely to be well within the measurement uncertainties. This recession rate is still somewhat high; the remaining difference may be a result of inaccuracies in the two models responsible for determining the NaOH(gas) concentration gradient (the sodium volatilization model in *Athena* and the thermodynamic model). Small changes in the NaOH(gas) predicted by each of these models (on the order of 5-10%) would be sufficient to reduce the corrosion rate to a value consistent with the measurements. Thus, predicted recession rates are extremely sensitive to the NaOH(gas) concentration gradient.

Summary and Conclusions

This chapter presents the first comprehensive analysis of the transport and chemical mechanisms that are potentially active in the corrosion of porous refractories used to line the crowns of glass melting furnaces. The work focuses on low-density silica refractory because of its extensive use throughout the glass industry and because of the serious corrosion problems that are observed for this material under some conditions. However, the nature of the analysis is such that these results can be extended to any refractory, assuming that a thermodynamic model is available to describe the chemical reaction between a gas-phase reactant, such as NaOH or KOH, and the refractory surface.

The results can be summarized briefly as follows: of the four mechanisms examined, only gas-phase transport of reacting species (in this case, NaOH) through a concentration boundary layer adjacent to the refractory hot face and a chemical-kinetic limitation at the surface of a silica particle appear to be realistic rate-limiting steps. Diffusion of reactant sodium, presumably as Na_2O, through a liquid product layer is far too fast to be rate-limiting under furnace conditions. Similarly, the analysis of capillary suction indicates that liquid sodium silicates will rapidly fill the small pores deep within a porous silica brick and thus block the intrusion of gas-phase species from entering and reacting. Thus, the combination of thermodynamic analysis with analytical models of transport phenomena presented here strongly supports the notion that corrosion of silica refractories in gas melting furnaces occurs primarily at the front (hot) face of the crown, rather than by motion of fluids (liquid or gas) into the porous interior.

Although computed corrosion rates based on mass transport through a gas boundary layer are somewhat greater than those observed, the results are very sensitive to the gas-phase concentration of NaOH and to the refractory temperature, both of which contain significant uncertainties. Similarly, lack of precise knowledge concerning the refractory temperature, which is almost certainly somewhat cooler than the combustion gases near it, affects the accuracy of thermodynamic calculations used to predict the sodium content of the corrosion product, which again affects the predicted corrosion rate. Clearly, these results point to the need for improved measurements of both temperature and NaOH concentration in full-scale furnaces. Based on the (admittedly limited) laboratory data presented here, it appears that extrapolation of short-duration experiments to the determination of long-term corrosion rates is problematic. Time-dependent effects, possibly the result of finite-rate chemical kinetics, may alter the composition of observed corrosion products, yielding results that differ from equilibrium predictions that seem to be valid at the very long lifetimes experienced by refractory bricks in full-scale furnaces.

Despite these uncertainties, the foregoing analysis provides considerable insight into the corrosion process and should be helpful in furnace design and optimization. In particular, the analytical models developed here can be incorporated as submodels within full-scale furnace CFD codes (the code has already been transferred to our project partner American Air Liquide and may be obtained from the corresponding author of this report). Furthermore, since corrosion appears to occur mainly at the crown hot face, the presence of pores in the refractory should have relatively little effect on the corrosion rate while at the same time providing suction of corrosion products into the bricks, substantially reducing dripping into the glass melt. Hence, the desirable features of low-density refractory, in particular its low thermal conductivity and weight, could be retained in an improved brick whose chemical reactivity toward gas-phase alkali is lower than that of silica.

Substantial progress toward the goal of predicting detailed maps of crown corrosion has also been made by coupling the gas-transport model and corrosion thermochemistry with a sophisticated CFD furnace model. Clearly, a number of factors are at work in this system that affect the accuracy of the model and improvements in several areas are needed to increase prediction accuracy. In particular, the submodels predicting the crown temperature and NaOH(gas) concentrations are critical and could probably be improved by better knowledge of crown temperatures and actual NaOH(gas) concentrations. Use of more complete thermodynamic data to predict the equilibrium NaOH(gas) concentration would undoubtedly help as well (for example, using thermodynamic data for the refractory that account for the effects of calcium oxide in the brick,[66] see Chapter 2). The present thermodynamic model accounts for only the SiO_2 and Na_2O components of the corrosion product, whereas it is known that the presence of calcium increases the corrosion rate. In general, however, the results are encouraging and suggest that models capable of predicting corrosion across an entire furnace crown are within reach.

References

[1] Reich, H. F.: Uber einige Untersunchungen an Silika-Gewolbesteinen aus Glaswannen mit unterscheidlichen Arbeitstemperaturen. Glastechn. Ber. **34** (1961), p. 15-27.

[2] Morsanyi, A. V.: Silica brick in the superstructure of glass-melting furnaces. Part 2. corrosion of silica brick in the superstructure and crowns of glass-melting furnaces. Glass Technol. **7** (1966), p. 196-202.

[3] Morsyani, A. V.: Silica brick in the superstructure of glass-melting furnaces. Part 1. Corrosion of silica brick by the vapour of sodium salts. Glass Technol. **7** (1966), p. 193-196.

[4] LeBlanc, J.: Controlling Silica Attack on Soda Lime Oxy-Fuel Furnaces. Ceram. Ind. (June 1996), p. 27-29.

[5] Gridley, M.: Philosophy, Design, and Performance of Oxy-Fuel Furnaces. Ceram. Eng. Sci. Proc. **18** (1997), p. 1-14.

[6] Paskocimas, C. A.;Leite, E. R.;Longo, E.; et al.: Determination of Corrosion Factors in Glass Furnaces. Ceram. Eng. Sci. Proc. **19** (1998), p. 75-88.

[7] Kotacska, L. H.;Cooper, T. J.: Testing of Superstructure Refractories in a Gas-Oxy Atmosphere Against High-Alkali Glasses. Ceram. Eng. Sci. Proc. **18** (1997), p. 136-145.

[8] Boillet, J.;Kobayashi, W.;Snyder, W. J.; et al.: Corrosion of Silica and Mullite Refractories Use in Glass Furnaces Under 100% Oxy-Firing Process. Ceram. Eng. Sci. Proc. **17** (1996), p. 180-190.

[9] Boillet, J.;Paskocimas, C. A.;Leite, E. R.; et al.: The Influence of Oxy-fuel Combustion Atmosphere in Glass Furnaces on Refractory Corrosion. In: Corrosion of Materials by Molten Glass; G. A. Pecoraro, J. C. Marra and J. T. Wenzel, Eds.; American Ceramic Society: Westerville, 1996; Vol. 78; p. 217-237.

[10] Faber, A. J.;Verheijen, O. S.: Refractory corrosion under oxy-fuel firing conditions. Ceram. Eng. Sci. Proc. **18** (1997), p. 109-119.

[11] Godard, H. T.;Kotacska, L. H.;Wosinski, J. F.; et al.: Refractory Corrosion Behavior Under Air-Fuel and Oxy-Fuel Environments. Ceram. Eng. Sci. Proc. **18** (1997), p. 180.

[12] Duvierre, G.;Zanoli, A.;Boussant-Roux, Y.; et al.: Selection of Optimum Refractories for the Superstructure of Oxy-Fuel Glass Melting Furnaces. Ceram. Eng. Sci. Proc. **18** (1997), p. 146-163.

[13] Tong, S. S. C.;Brown, J. T.;Kotacska, L. H.: Determination of Trace Impurities in a Furnace Atmosphere at Operating Temperature. Ceram. Eng. Sci. Proc. **18** (1997), p. 208-215.

[14] Wu, K. T.;Kobayashi, H.: Three-Dimensional Modeling of Alkali Volatization/Crown Corrosion in Oxy-fired Glass Furnaces. In: Corrosion of Materials by Molten Glass; G. A. Pecoraro, J. C. Marra and J. T. Wenzel, Eds.; American Ceramic Society: Westerville, 1996; Vol. 78; p. 205-216.

[15] Misra, M. K.;Tong, S. S. C.;Brown, J. T.: Superstructure corrosion in glass tanks: comparison of mathematical model with field measurements. Ceram. Eng. Sci. Proc. **19** (1998), p. 137-143.

[16] Allendorf, M. D.;Spear, K. E.: Thermodynamic Analysis of Silica Refractory Corrosion in Glass-Melting Furnaces. J. Electrochem. Soc. **148** (2001), p. B59-B67.

[17] Faber, A. J.;Beerkens, R. G. C.: Reduction of refractory corrosion in oxy-fuel glass furnaces. In: XVIII Int. Cong. Glass1998. The American Ceramic Society (Westerville, OH), 1998.

[18] Walsh, P. M.;Moore, R. D.;Neufeld, J.; et al.: Sodium volatilzation and silica refractory corrosion in an oxygen/natural-gaso-fired soda-lime-silica glass melting furnace. In: XIX Int. Cong. Glass, Edinburgh, Scotland 2001. 2001. p. 134-135.

[19] Walsh, P. M.;Moore, R. D.: Na vapor and gas temperature measured in glass container furnaces. The Glass Researcher **10** (2000), p. 3-4.

[20] Buckley, S. G.;Walsh, P. M.;Hahn, D. W.; et al.: Measurements of sodium in an oxygen-natural gas-fired soda-lime glass melting furnace. Ceram. Eng. Sci. Proc. **2** (2000), p. 183-205.

[21] Rohsenow, W. M.;Choi, H. Y.: Mass and Momentum Transfer; Englewood, N.J.: Prentice-Hall, 1961.

[22] Bird, R. B.;Stewart, W. E.;Lightfoot, E. N.: Transport Phenomena; New York: Wiley, 1960.

[23] Hirschfelder, J. O.;Curtiss, C. F.;Bird, R. B.: Molecular Theory of Gases and Liquids; New York: Wiley, 1954.
[24] van Limpt, J. A. C.: Volatilisation in glass furnaces. An experimental tool to predict emissions of volatile species in industrial glass furnaces. In: Int. Conf. Glass, Amsterdam 2000. 2000.
[25] Weresczzak, A.;Wang, H.;Karakus, M.; et al.: Postmortem Analysis of Salvaged Conventional Silica Bricks from Glass Production Furnaces. Glass Sci. Technol. **73** (2000), p. 165-174.
[26] Webb, B. W.: Measuring and Modeling Combustion in Glass Melting Furnaces. Glass Researcher **6** (1997), p. 16-18.
[27] ChemSage™ 4.1; GTT Technologies, Herzogonrath, Germany:, 1998.
[28] Eriksson, G.;Hack, K. "SGTE Pure Substance Database, 1996 Version," produced by the Scientific Group Thermodata Europe and obtained through GTT Technologies (see Ref. 27).
[29] Moore, R. D.;Neufeld, J.;Wolfe, H. E., personal communication, 2000.
[30] Wu, K. T., Praxair Inc., personal communication, 2001.
[31] Hummel, F. A.: Introduction to Phase Equilibria in Ceramic Systems; New York: Marcel Dekker, 1984.
[32] Sosman, R. B.: The Phases of Silica; New Brunswick, NJ: Rutgers University Press, 1965.
[33] Gupta, A., Monofrax Inc., personal communication, 2000.
[34] Yiantsios, S. G.;Higgins, B. G.: Rayleigh-Taylor Instability in Thin Viscous Films. Phys. Fluids **A1** (1989), p. 1484-1501.
[35] Chandrasekhar, S.: Hydrodynamic and Hydromagnetic Stability; Oxford: Clarendon Press, 1961.
[36] Kucuk, A.;Clare, A. G.;Jones, L. E.: The Influence of Various Atmospheres on the Surface Properties of Silicate Melts. Glass Sci. Technol. **73** (2000), p. 123-129.
[37] Kucuk, A.;Clare, A. G.;Jones, L.: An Estimation of the Surface Tension for Silicate Melts at 1400 C Using Statistical Analysis. Glass Technol. **40** (1999), p. 149-153.
[38] Mesko, M. G.;Shelby, J. E.: Solubility and diffusion of water in melts of a TV panel glass. Phys. Chem. Glasses **42** (2001), p. 17-22.
[39] Pfeiffer, T.: Viscosities and Electrical Conductivities of Oxidic Glass-Forming Melts. Sol. State Ionics **105** (1998), p. 277-298.
[40] Schaeffer, H. A.: Diffusion controlled processes in glass forming melts. J. Non-Cryst. Sol. **67** (1984), p. 19-33.
[41] Moulson, A. J.;Roberts, J. P.: Water in silica glass. Trans. Br. Ceram. Soc. **59** (1960), p. 388-399.
[42] Moulson, A. J.;Roberts, J. P.: Water in silica glass. Trans. Faraday Soc. **57** (1961), p. 1208-16.
[43] Mesko, M. G.;Shelby, J. E.: Water solubility and diffusion in melts of commercial silicate glasses. Glass Sci. Technol. **73** (2000), p. 13-22.
[44] Reid, J. E.;Poe, P. T.;Rubie, D. C.; et al.: The self-diffusion of silicon and oxygen in diopside liquid up to 15 GPa. Geochim. Cosmochim. Acta **174** (2001), p. 77-86.
[45] Lesher, B. E.;Hervig, R. L.;Tinker, D.: Self Diffusion of Network Former (Silicon and Oxygen) in Naturally Occurring Basaltic Liquids. Geochimica et Cosmochimica Acta **60** (1996), p. 405-413.
[46] Roberts, C. D.;Pint, B. A., personal communication, 1998.
[47] Wereszczak, A. A.;Karakus, M.;Liu, K. C.; et al. "Compressive Creep Performance and High Temperature Dimensional Stability of Conventional Silica Refractories," Oak Ridge National Laboratories report ORNL/TM-13757, 1999.
[48] Brown, J. T.;Spaulding, R. F.;Whittemore, D. S.; et al.: New Silica Refractory of Oxy/Fuel Glass Melting. Int. J. Glass., Proc. XV A.T.I.V. Conf. Parma (1999), p. 120-128.
[49] Prior, H. D.;McIntyer, D. A.;Bonsall, S. B.: A test procedure to characterize refractories for oxy-fuel fired glass furnace crown applications. In: Proc. Sixth UNITCER99 (Unified Int. Tech. Conf. Refractories), Berlin, Germany 1999. 1999. p. 230-233.
[50] Scheidegger, A. E.: The Physics of Flow Through Porous Media; Toronto: University of Toronto Press, 1974.
[51] Dullien, F. A. L.: Porous Media: Fluid Transport and Pore Structure; New York: Academic Press, 1979.

[52] Wolfe, H. E. "Laboratory Report #PD-0398 on Gen-Sil Silica Brick (from Gallo 7-year oxygen/fuel campaign)," Harbison Walker Refractories Co., Garber Research Center report PD-0398, 2000.
[53] Schlichting, H.: Boundary Layer Theory; New York: McGraw Hill, 1968.
[54] Bockris, J. O. M.;Mackenzie, J. D.;Kitchener, J. A.: Viscous Flow of Silica and Binary Liquid Silicates. Faraday Society, London Transactions **51** (1955), p. 1734-1748.
[55] Hetherington, G.;Jack, K. H.: Water in Vitreous Silica: I. Influence of Water Content on the Properties of Vitreous Silica. Phys. and Chem. of Glasses 3 **3** (1962), p. 129-133.
[56] Wolfe, H. E. "Laboratory Report PD-0396 on Silica Brick and Castables: Vega, VegaO2, Visil, and H-W Crownseal I," Harbison Walker Refractories Co., Garber Research Center report PD-0396, 1999.
[57] Ammouri, F.;Champinot, C.;Béchara, W.; et al.: Influence of oxy-firing on radiation transfer to the glass melt in an industrial furnace: importance of spectral radiation model. Glass Sci. Technol. **70** (1997), p. 201-206.
[58] McGinnis, P. B.;Shelby, J. E.: Diffusion of Water in Float Glass Melts. J. Non-Crystalline Solids **177** (1994), p. 381-388.
[59] Zhang, Y.;Behrens, H.: H_2O diffusion in rhyolitic melts and glasses. Chemical Geology **169** (2000), p. 243-262.
[60] Doremus, R. H.: Diffusion of Water in Thyolite Glass: Diffusion-Reaction Model. J. Non-Cryst. Sol. **261** (2000), p. 101-107.
[61] C. Schnepper; O. Marin; C. Champinot; J.-F. Simon. "A modeling study comparing an air- and an oxy-fuel fired float glass melting tank"; Proc. XVIII Int. Cong. Glass, 1998, San Francisco.
[62] T. Pfeiffer. "Viscosities and Electrical Conductivities of Oxidic Glass-Forming Melts" *Sol. State Ionics,* 1998, **105**, 277-298, (1998).
[63] P. M. Walsh; R. D. Moore. "Na vapor and gas temperature measured in glass container furnaces" *The Glass Researcher,* 2000, **10**, 1, 3-4, (2000).
[64] P. M. Walsh; R. D. Moore; J. Neufeld; L. Lemings; J. T. Brown; K. T. Wu. "Sodium volatilzation and silica refractory corrosion in an oxygen/natural-gaso-fired soda-lime-silica glass melting furnace"; XIX Int. Cong. Glass, 2001, Edinburgh, Scotland.
[65] S. G. Buckley; P. M. Walsh; D. W. Hahn; R. J. Gallagher; M. K. Misra; J. T. Brown; S. S. C. Tong; F. Quan; K. Bhatia; K. K. Koram; V. I. Henry; R. D. Moore. "Measurements of sodium in an oxygen-natural gas-fired soda-lime glass melting furnace" *Ceram. Eng. Sci. Proc.,* 2000, **2**, 1, 183-205, (2000).
[66] K. E. Spear, T. M. Besmann, and M. D. Allendorf in E. Opila, J. Fergus, P. Hou, T. Mauyama, T. Narita, E. Wuchina, and D. Shifler High Temperature Corrosion and Materials Chemistry V, The Electrochemical Society Proceedings Series, in press 2005.

CHAPTER 5†

DETECTION OF NAOH VAPOR IN GLASS FURNACES USING EXCIMER LASER PHOTOFRAGMENTATION SPECTROSCOPY

Abstract

Corrosion of refractory silica brick and problematic air quality issues surrounding particulate emissions are two important glass manufacturing problem areas that have been tied to volatilized sodium and its transport throughout the melt tank. Although there is some understanding of the relationship between tank operating conditions and tank atmosphere sodium levels, until recently direct quantitative measurements of sodium levels has been limited to extractive sampling methods followed by laboratory analysis. Excimer laser induced fragmentation (ELIF) fluorescence spectroscopy is a technique that permits the measurement of volatilized NaOH in high-temperature environments on a timescale of less than one second. The development of this method and the construction of field-portable instrumentation for glass furnace applications are reported. Characteristics of the method are outlined, including equipment configuration, detection sensitivity, and calibration methodology. Results from a small batch furnace and two commercial float glass furnaces are used to show the potential impact and the existing limitations of the ELIF approach for real-time NaOH vapor monitoring. This method is shown to be effective in industrial settings and presents an approach to optimize burner settings.

Introduction

Over the past several years a number of reports have illustrated the use of various online analytical techniques to monitor metals in industrial process gas. Many of these are discussed in an excellent review that has been published recently[1]. One method that has been demonstrated to be particularly promising is photofragmentation fluorescence (PFF) of which Excimer Laser Induced Fragmentation Fluorescence (ELIF) is a version that uses the high-energy ultraviolet light from an excimer laser. To date, a number of authors have explored the use of ELIF in industrial applications specifically to determine alkali concentrations in solid fuel combustors[2-7]. That work has shown that this method is capable of detecting sodium hydroxide and sodium chloride concentrations in the ppb range at temperatures as high as 1000 °C. The general technical approach of the method is to illuminate the vapor that contains simple molecular metal-containing species, such as NaOH, NaCl, KOH, etc., with 193-nm laser pulses from an ArF laser. The subsequent photo-dissociation of these alkali species results in a population of excited metal atoms that emit easy-to-detect atomic fluorescence.

There are a number of potential applications of this nearly real-time analytical technique in addition to solid fuel combustion diagnostics. In the case presented in this paper, understanding the behavior of alkali metals in glass furnaces is an especially attractive application because of two important practical issues surrounding the role of sodium in the furnace atmosphere. Sodium volatilization from the melt to the vapor phase in the furnace and into the exhaust can (1) directly effect the formation of

† This chapter was originally published in *Glass Science and Technology* in 2005 and was edited for this report.

particulates[8,9], and (2) indirectly affect the durability of the furnace over time. Recent work based on thermodynamic calculations has shown the importance trace alkali vapor has on the degradation of the silica based or silica containing refractory material from which these furnace parts (crown and sidewalls) are constructed. This may be especially true for furnaces operating with pure oxygen in place of air in the burners[10-16].

Given the important role alkali vapor plays in practical operation of furnaces, it is desirable to make direct measurements of alkali metal concentration within the furnace atmosphere. All recent thermodynamic studies of the relevant chemistry of volatilized alkali metals indicate that greater than 99% of the sodium or potassium in a typical furnace atmosphere exists in the form of a metal hydroxide vapor, NaOH or KOH, when a slight excess of oxygen is used in the burners; $p(O_2) > 500$ Pa [17,18]. The presence of chloride as an impurity in the raw material may lead to NaCl as well[18]. With the exception of recent application of laser-induced breakdown spectroscopy (LIBS)[19] and direct atomic absorption[20], practical analytical methods for measuring sodium and potassium in glass furnaces have been dominated by extractive sampling approaches followed by analysis of either the hot vapor, the liquid condensate, or both[14]. The objective of the work presented here is to assess the practical applicability of this somewhat complicated, but very sensitive, spectroscopic method to provide real time data that could be used to optimize furnace operation.

In this paper, we illustrate the application of ELIF as a means to examine the concentration of alkali metals in the gas composition of glass manufacturing furnaces. This paper reports the development of a measurement method and the design and implementation of an apparatus that can measure in real time the concentration of NaOH in the vapor phase of an oxygen-fuel glass furnace in an industrial environment. The principle of operation of the spectroscopy-based sensor and several examples of the application of a field-ready unit are described. The paper shows that although precise and absolute quantitative measurements are difficult using the present instrument configuration, a sensor based on the ELIF approach has the potential to provide real time information when calibrated with extractive sampling.

ELIF Spectroscopic Method

A number of researchers have contributed to the development of ELIF for the particular application to sodium species over the past decade[2-4]. The basic physical mechanism of the detection of total sodium concentration via NaOH sensitive ELIF is illustrated by the potential energy curves in Figure 5-1. The technique relies on the detection of atomic fluorescence from electronically excited sodium atoms that are produced from the dissociation of NaOH by 193-nm ultraviolet light generated by an ArF excimer laser. Excitation of ground-state NaOH at 193 nm contains sufficient energy not only to dissociate the molecules, but also produce Na atoms in an excited $3p^2P$ state. The excited ^2P atoms subsequently emit light at 589 nm, which is in the middle of the visible spectrum. This fluorescence is actually composed of two lines separated by 0.6 nm and are known as the sodium "D" lines which have been used for centuries to identify the presence of sodium in a wide range of applications from alchemy to astrophysics. The method is selective to NaOH and does not detect atomic sodium in the vapor, since the laser does not excite atoms directly.

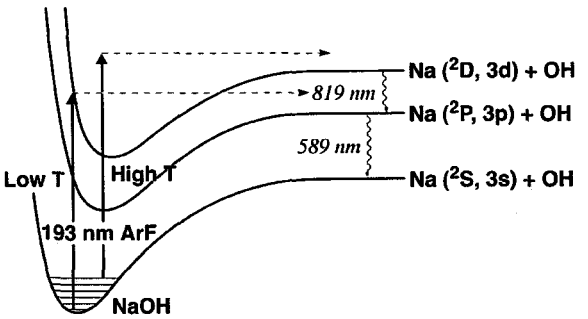

Figure 5-1. Potential curves showing the application of ELIF for the detection of NaOH in high-temperature environments.

In a high-temperature environment, a portion of the NaOH molecular population contains sufficient vibrational energy such that when excited by 193-nm light, sodium atoms can be produced in an excited atomic state identified as the $3d^2D$ state[4]. The figure shows this by indicating NaOH molecules occupy higher vibrational levels in the ground state and will retain this energy when excited. This $3d^2D$ state can transition to the $3p^2P$ state, emitting radiation at 819 nm. Depending on the furnace conditions, both the 589-nm and 819-nm lines can be observed. The 589-nm line is present in the ELIF spectrum of numerous simple Na-containing molecular species whereas the observation of 819 nm ^2D-^2P fluorescence is species and temperature dependent. The 819 nm line is not likely to be very useful as a diagnostic for NaOH in a furnace environment because of the pronounced temperature dependence of its intensity, overall weaker intensity, and susceptibility to quenching by CO_2. The remainder of this paper will focus primarily on the behavior of the 589-nm line.

A bench scale system was developed to characterize the ELIF method and to mimic the glass furnace environment. A 1-meter long, 5 cm OD, alumina tube is situated within a 1600 °C (max) tube furnace. The ceramic tube is equipped with UV fused silica windows that serve as optically transparent end-caps. The gas flowing through the tube is vented into a hood. An atomizer produces a flow of water vapor containing NaOH aerosol that is simultaneously introduced into the tube furnace with other gases from a mixing manifold. The atomizer was calibrated to establish the water vapor flow rate. This flow rate and the NaOH concentration in the reservoir is used to determine the mass flow rate of sodium into the cell. The temperature profile within the cell has been well characterized and is described elsewhere[21]. In addition to the NaOH carried by the water vapor, the composition of the gas in the flow cell can varied to include carbon dioxide, nitrogen, and oxygen to better mimic the furnace environment.

The excimer laser beam is directed into the ceramic cell that has an established slow flow of the desired gas mixture. The laser is operated at 100 Hz and produces a 12 ns pulse. The 193-nm ultraviolet light from the excimer dissociates the NaOH species in the vapor phase and produces sodium atoms that can subsequently fluoresce at several possible wavelengths in the visible part of the spectrum, as is explained above. This light is collected with a telescopic lens system, dispersed by a small spectrometer, and detected using an intensified (50 ns gate) multichannel diode array. The timing of the gate is chosen to collect light from –10 ns to +40 ns relative to the peak of the pulse. A Plexiglas window is positioned in front of the spectrometer to block the 193-nm light.

The keys to the design of a fieldable instrument capable of quantitatively measuring NaOH concentration rests on the characteristics of the ELIF signal as a function of laser power, laser penetration depth into the furnace, temperature, and gas composition in the furnace atmosphere. The laboratory-based high temperature cell was used to characterize the system with respect to these parameters.

The temperature conditions in an oxy-fuel float glass furnace outside the immediate burner flame can range as high as 1700 °C and typically have NaOH concentrations in the hundred-ppm range. Figure 5-2 shows an ELIF spectrum of a 130-ppm NaOH sample in air at approximately 1000 °C and at 1500 °C obtained in the tube furnace. The 589 nm lines and the 819 nm lines are closely spaced doublets that appear as a single line due to the limits of resolution of the spectrometer (1.9 nm). Note that the 819 nm line is very weak at lower temperature. The signal-to-noise on the 589 nm line is approximately 550:1, with a data collection time of 0.5 s.

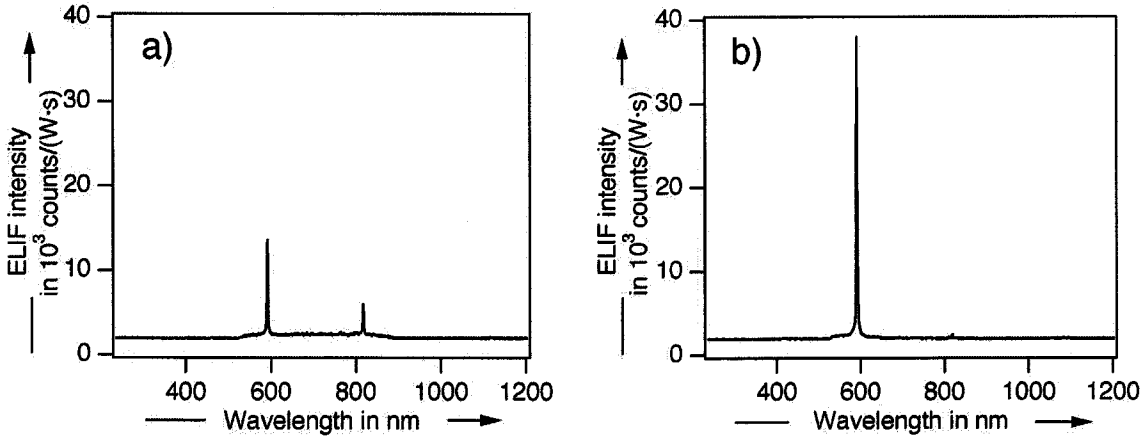

Figure 5-2. Typical ELIF signal at a) 1500 °C and b) 1000 °C.

Figure 5-3 shows a plot of the intensity dependence of the 589-nm line as a function of NaOH vapor concentration in the flow furnace. The response is nonlinear with a roll-off in the linearity of the response at higher NaOH concentrations. This curve is in excellent agreement with previously published data that describes the effect of radiation trapping at these high concentrations[22].

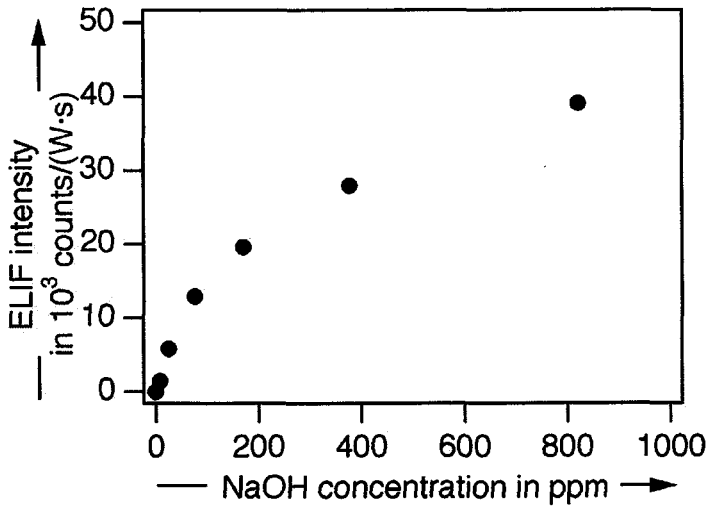

Figure 5-3. ELIF response at 589 nm as a function of NaOH concentration in nitrogen at 1500 °C.

The data obtained in the tube furnace calibrates the signal vs. concentration at a fixed pulse energy (100 μJ) and laser repetition rate in the well-controlled conditions of the laboratory tube furnace. The difficultly in developing a truly quantitative instrument is tied to the attenuation of the 193 nm laser beam by the intrinsic absorptivity of hot CO_2 (and to a lesser extent O_2) in the furnace atmosphere[21,23]. For example, the reduction in overall signal intensity in Figure 5-2 at 1500 °C relative to 1000 °C is due to the increased attenuation of the excimer laser by oxygen in air at elevated temperature. Although the oxygen concentration is low in a glass furnace, a typical gas composition in an oxy-fired furnace contains greater than 30 vol.% CO_2. At temperatures above 1200 °C, beam attenuation due to CO_2 is significant and prevents, in a practical sense, being able to determine accurately the laser beam intensity within the detection volume. The net result is that the effective laser probe penetration depth into a furnace is less than one meter and is a strong function of temperature. Accurate calibration is dependent on being able to quantitatively characterize the beam attenuation from these various effects and thus know the amount of UV light present in the imaged region to dissociate the NaOH molecules. For example, the ELIF signal at 1500 °C and 50 cm penetration into the calibration cell will be reduced by about a factor of three at 20 vol.% CO_2 relative to pure nitrogen.

The path length through the hot gases in the calibration tube furnace and the wall of the glass furnace or glass furnace vent in the experiments described in the next section were matched. However, as a result of this beam attenuation complication, unless both the carbon dioxide partial pressure and the gas temperature are known precisely, the ELIF signal cannot be accurately calibrated to make a quantitative determination of the NaOH concentration. However, the sensitivity and the stability of the ELIF approach make this method a very good candidate for a relative on-line measurement. That is, an instrument can be calibrated to a particular position in a furnace by taking a sample of the vapor and subsequently analyzing it. Such a measurement can then be used to show relative changes in NaOH concentration with very high time resolution as operating conditions within the furnace are tuned.

Portable System Design

A portable system was constructed to take this spectroscopic sensor method to oxy-fired glass furnaces to explore the ELIF approach as a real time sensor in industrial settings. The instrument needed to be portable and sufficiently rugged to be able to withstand the high ambient air temperature adjacent to a melt tank. The field unit consists of an optical table top (Sensor Module) supported by a wheeled hydraulic jack. The jack enables the Sensor Module to be positioned at elevations ranging from 1.2 m to has high as 2.3 m and tilted to point either up or down at an angle of up to ± 20 °. The Sensor Module consists of the excimer laser, the detector, and imaging optics enclosed in an insulated, air-conditioned compartment. It is supported by a pair of cabinets, or Support Modules, that house the electronics needed to operate the detector along with two air conditioners that cool the laser and detection electronics. The Sensor and Support modules are constructed from sheet metal panels that sandwich 2-cm thick insulation blankets.

The layout of the Sensor Module is shown in Figure 5-4. The output of the excimer laser is centered on a 5-cm diameter port that provides stand off from the intense heat emanating from a furnace port. This tube serves as both laser probe output and signal detection port of the sensor by permitting the pulsed laser output to exit through a UV fused silica window and collecting the ELIF signal off axis. Figure 5-5 shows a schematic of the light collection and focusing configuration. The simple single collection lens imaging scheme is configured with a turning mirror that images a point along the laser beam ranging from zero to more than four meters from the exit port. The probe volume is imaged onto a 0.025 mm fixed slit on the spectrometer. Figure 5-6 is an illustration of the overall portable system at a furnace port.

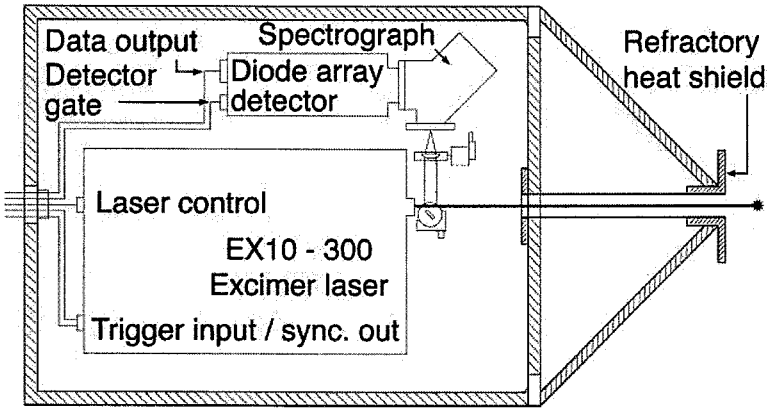

Figure 5-4. Schematic of the Sensor Module layout.

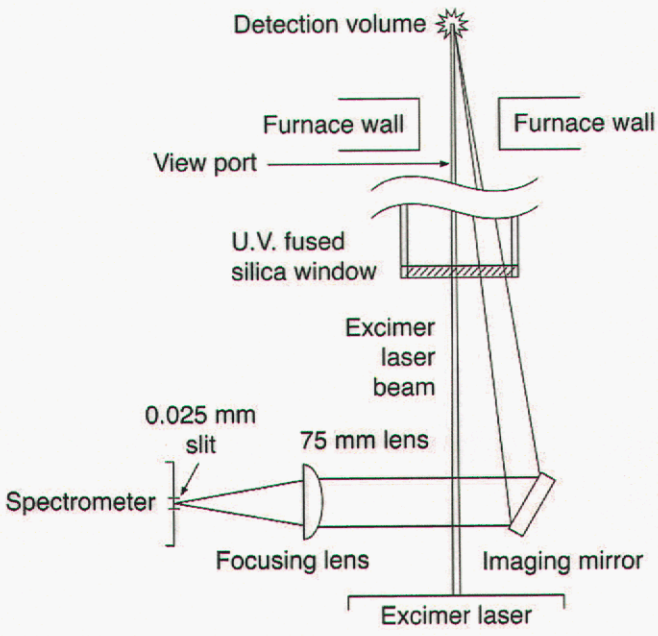

Figure 5-5. Geometry of the off-axis imaging of the NaOH ELIF signal.

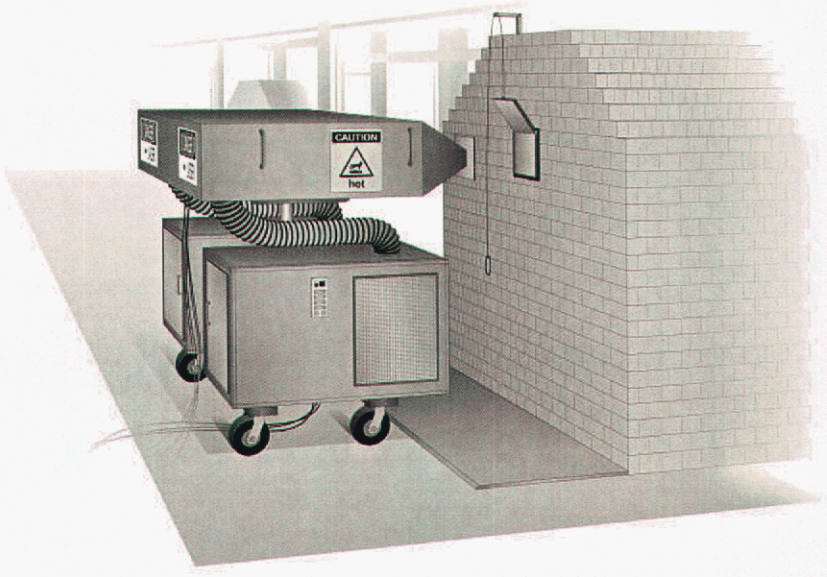

Figure 5-6. Illustration of the portable ELIF system at a furnace port. The upper module sensor contained the sensors platform shown in the schematic layout in Figure 5-5.

Batch Furnace Tests

The first field tests were conducted at a batch glass furnace at the University of Missouri at Rolla. That furnace is described in detail elsewhere[24]. For these tests, the single burner furnace was operated in an oxy-fuel mode maintained at 1500 °C. Feed mix including cullet was fed to the furnace in regularly added batches that contained measured amounts of sodium carbonate. Typical batch operation consisted of adding a1 kg bag of mix every 15 min: SiO_2 42 wt%, Na_2CO_3 14 wt%, $CaCO_3$ 3.5 wt%, dolomite 9.8 wt%, gypsum 0.7 wt%, cullet 30 wt%. Na_2CO_3 was added to increase the NaOH concentration in the chamber. Glass can be removed from the base of the tank, however, during this testing, the glass melt was simply allowed to accumulate.

These initial tests were used to evaluate the durability of the unit when operated adjacent to a furnace port. The instrument was calibrated using the tube furnace configuration for a focal point about 40 cm in front of the heat shield, locating the sample volume approximately 5 cm inside the inner wall of the furnace. The sodium hydroxide ELIF signal was recorded as a function of time following the addition of each batch. The evolution of the ELIF spectrum is shown in Figure 5-7. The conversion from ELIF signal to ppm (mole/mole) is from the calibration procedure conducted in the tube furnace. At approximately 16 seconds, a batch of feed mix (including the sodium carbonate) is added to the melt. The ELIF signal increases dramatically and then begins to taper off. Figure 5-7 compares a normal batch feed with feed that contained only cullet. The "cullet only" tests were conducted to determine if the ELIF system was truly detecting the presence of NaOH in the vapor or was erroneously measuring some other effect from the batching procedure such as a disturbance in the gas flow field indirectly resulting in a boost in the background NaOH signal.

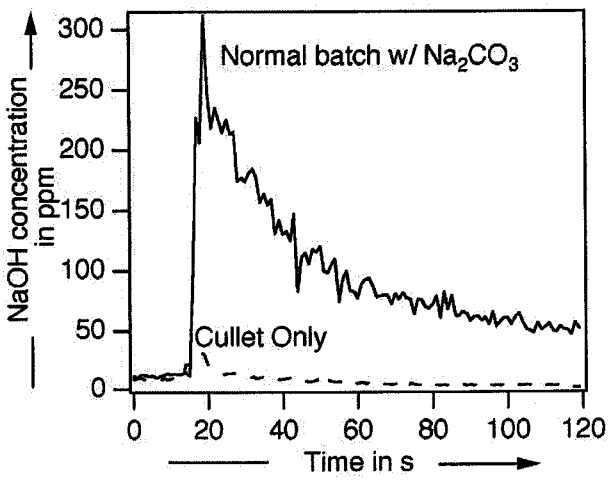

Figure 5-7. Comparison of the absolute sodium concentration in the batch furnace atmosphere after an addition of a normal 1 kg batch w/ 14% Na_2CO_3 and after "blank" batch containing only cullet.

Figure 5-8 shows a sample ELIF scan of a batch that contained both Na_2CO_3 and K_2CO_3. Note the prominent signal at 768 nm due to the ELIF from KOH. Although calibration curves for the KOH signal were not developed, it is clear that both sodium and potassium can be monitored simultaneously. The inset shows the KOH feature to be the pair of atomic lines in the potassium atomic spectrum $5p^2P_{3/2,1/2} - 4s^2S$) at 766.5 and 769.9 nm.

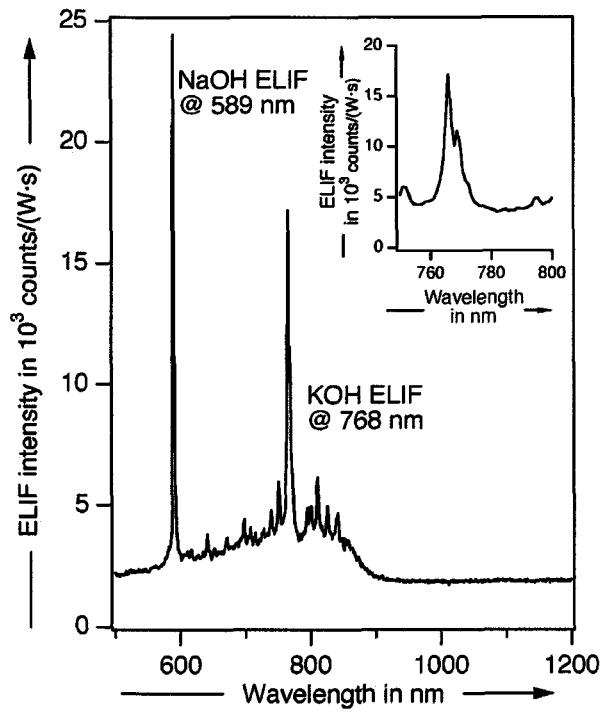

Figure 5-8. ELIF signal in the batch furnace from the addition of a mixture containing both sodium and potassium carbonate. The inset shows the resolution of the potassium doublet at 766.5 nm and 769.9 nm.

Industrial Furnace Tests

As a result of the batch furnace tests, the instrument underwent several modifications with respect to the cooling system and was taken to PPG Industries Inc. float glass furnaces. The purpose of this series of tests was twofold. The first goal was to assess the durability of the instrument in an actual industrial environment and the second goal was to compare the results of the ELIF method to a set of extractive atmospheric samples taken from the same ports.

From a durability standpoint there are two primary constraints. The laser cannot operate above 40 °C and the detector temperature must be maintained at -20 °C thermoelectrically. It is important to note that the air temperature one meter from the furnace wall is approximately 90 °C in an industrial furnace whereas at UM Rolla, the temperature was only 55 °C 20 cm from the furnace and 35 °C one meter away. In addition to the high ambient temperature, at 1500 °C, the radiant heat flux entering the sensor head through the 5 cm diameter optical port is approximately 60 W/cm^2, resulting in nearly 1200 W to be removed from the sensor by the air conditioning system. In general, the portable unit performed well, however, there was some difficulty with overheating if the sensor was directly in front of an open port for over twenty minutes.

Figure 5-9 shows three typical data sets recorded during these field trials. Figure 5-9a shows the background fluorescence signal recorded through a peephole, located about mid-tank, which permits visual access directly into the melt tank. Figure 5-9b shows the corresponding ELIF signal recorded at the same peephole. Figure 5-9c shows the ELIF signal recorded in an exhaust vent about 20 ft downtank from the position in Figures 5-9a and 5-9b. The background fluorescence is much greater than in the batch furnace at Rolla and contains additional features. This large background is present primarily because the peephole view is directly opposite a burner. Note the broad fluorescence in the region of the 589 nm sodium line and the very sharp dip in this fluorescence due to the absorption by ground state sodium atoms along the optical path from the burner flame to the detector. There is atomic emission from volatilized potassium as well. Although the ELIF signal at 589 nm peering directly into the tank is stronger than the signal in the exhaust, it is complicated by the broad feature in the background spectrum. The exhaust ELIF signal is cleaner and looks identical to the 589 nm spectra that were obtained in the lab and in the batch furnace at Rolla. That is, there is no interfering atomic sodium emission from the burners. This was also the case for ELIF data recorded directly above the fill end of the furnace. Clearly the ELIF method can be used to produce strong NaOH signals with the sensor unit adjacent to the melt tank, but it appears the analysis and conversion using a calibration curve will be much simpler when monitoring the exhaust.

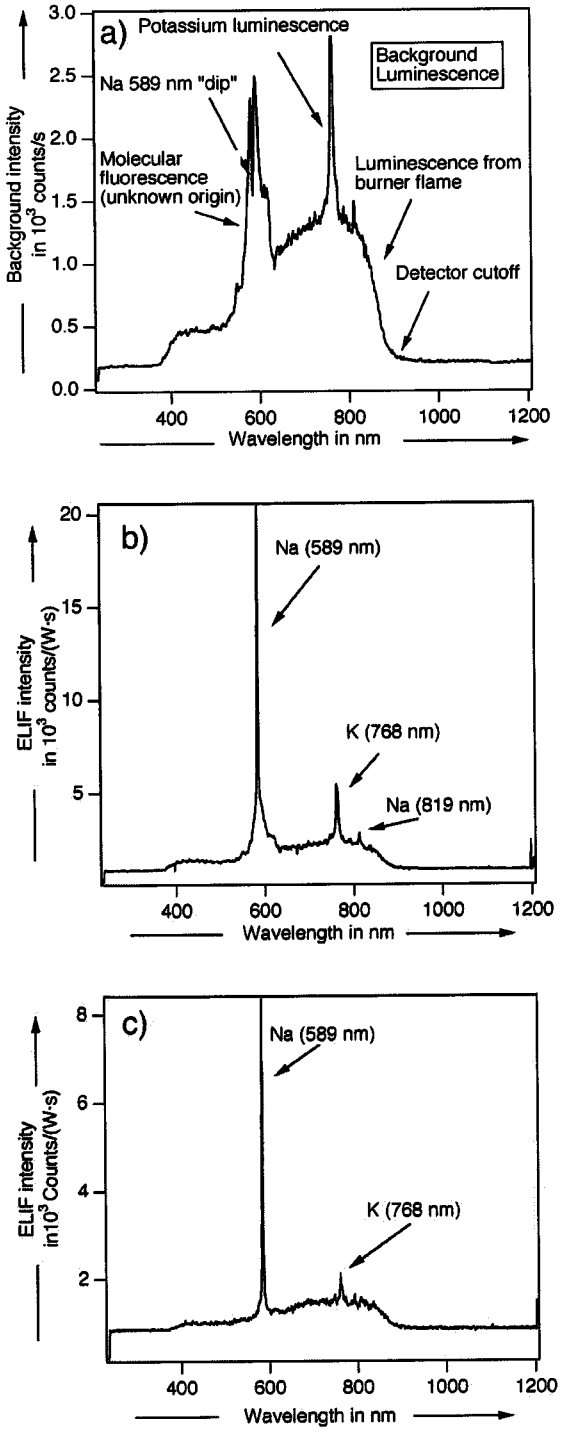

Figure 5-9. a) Background fluorescence in a melt tank, b) ELIF signal from a tank peephole, c) ELIF signal from an exhaust peephole.

An important part of the evaluation of the applicability of the ELIF technique is determining the quantitative accuracy of this method relative to direct sampling. Samples of the furnace composition were obtained using a commercial stack sampling system (Andersen Instruments MST). The technique consists of drawing approximately 0.3 m^3 of gas (dry) from the furnace and condensing out the water vapor in a series of chilled vessels. The water content of the samples was determined using EPA Method #4. The accumulated condensate is then subsequently analyzed for its composition using a direct current plasma emission technique. Based on the measured volume of vapor withdrawn and the total amount of sodium collected, the total sodium concentration in the furnace was determined directly, independent of speciation, to serve as a comparison to the ELIF measurements using the calibration shown in Figure 5-3. Table 5-1 shows these results. The time averaged ELIF concentrations are in the appropriate range with the exception of position 5. The missing data for the ELIF method on the refiner and for the extraction probe on the feeder are the result of the physical access constraints. Considering the beam attenuation uncertainties and the time dependent fluctuations of the actual concentration of NaOH itself (discussed below), this agreement should be considered to be fairly good for a "first generation" instrument, again with the exception of the position 5 measurement.

Table 5-1 - ELIF NaOH measurements and extractive sampling results

Furnace Port	Extraction Sample Na concentration (ppm)	NaOH concentration ELIF (ppm)[a]
1. Right side midtank port	185	125
2. Right side exhaust port	202	117
3. Right side uptank port	158	143
4. Fill end	n.a.	90
5. Left side downtank port	221	31
6. Left side refiner–entrance	17	n.a,

a- using calibration in Figure 5-3, n.a- not available due to access constraints

A second series of experiments was undertaken. The focus of this second set of tests was to determine whether the ELIF technique could be used as a direct diagnostic to provide real-time data regarding the effect of burner operation in the tank. The potential consequences of changing melt temperature, gas velocity, burner stoichiometry, etc. are discussed in detail by Beerkens and van Limpt in a recent paper that attempts to model volatilization processes[18]. These measurements explore the effects of burner stoichiometry and temporal concentrations dynamics.

The ELIF system was positioned to monitor at a particular point in an exhaust vent as in a fashion similar to Figure 5-6. Baseline data were recorded and calibrations for the optical sensitivity were recorded on site. Over a period of several hours, the tank burners were adjusted to change the fuel equivalence ratio first to more fuel lean conditions, then back to the "normal" configuration, and then to more fuel rich conditions. The operation or the burners was never sub-stoichiometric. The stoichiometry was changed by adding more or less oxygen to the oxy-fuel burners with the fuel flow rate held constant.

In the course of these tests, it became apparent that there are additional considerations when evaluating the quantitative aspects of the ELIF measurement. Figure 5-10 shows three records of the intensity of the 589 nm NaOH ELIF signal as a function of time. Figures 5-10a and 5-10b show the time dependence of the signal at furnace #1 sampling directly into the tank and sampling in the exhaust, respectively, using a 1 s time constant for the measurement. The signal from the tank is much less stable than the signal measured in the exhaust. Figure 5-10c shows the time variation in the exhaust at a furnace #2 with much higher time resolution. There appear to be a variety of timescales present, represented by both short bursts in the signal on the order of seconds and as well as longer term drifts.

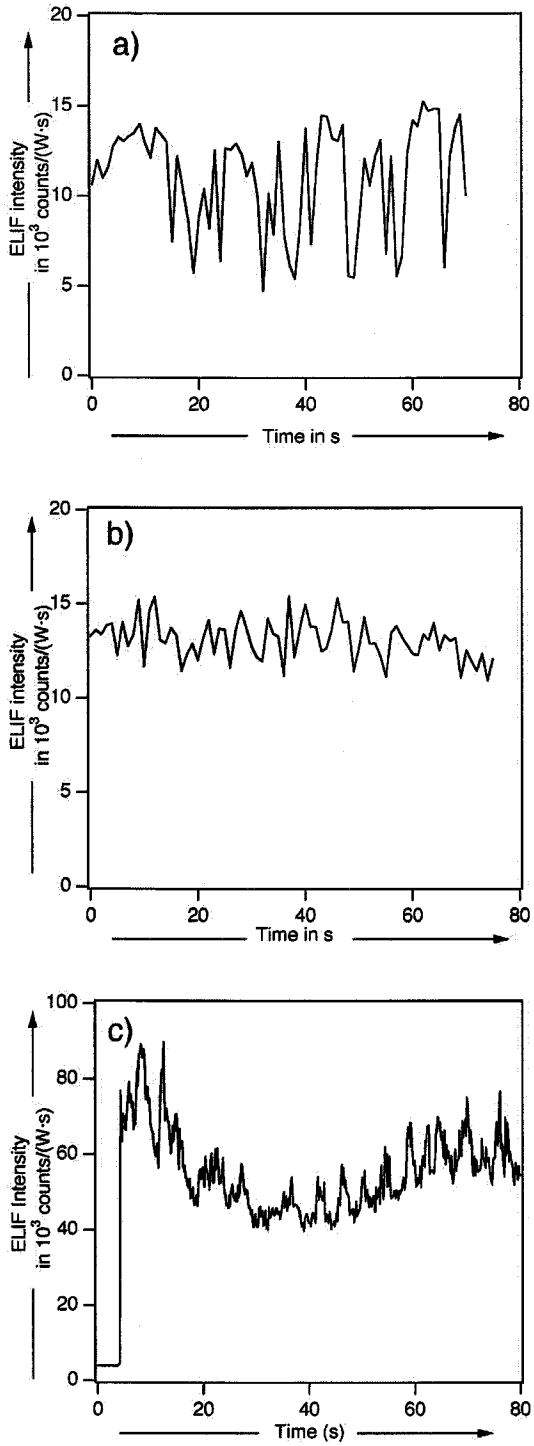

Figure 5-10. Time dependence of the NaOH ELIF signal as a function of tank position. a) Directly into the melt tank the first furnace, 1s sample time. b) Directly into exhaust stack the first furnace, 1s sample time. c) Directly into an exhaust stack at the second furnace, 0.067 s sampling time.

Despite these inherent drifts in the system, a series of brief time-averaged measurements with different burner stoichiometry was recorded and is shown in Figure 5-11. At first glance, it appears that the experiments are not particularly definitive. Although there are measurements where the signal is greater than in than others, there does not appear to be any well-defined trend that can be affiliated with the operating adjustments.

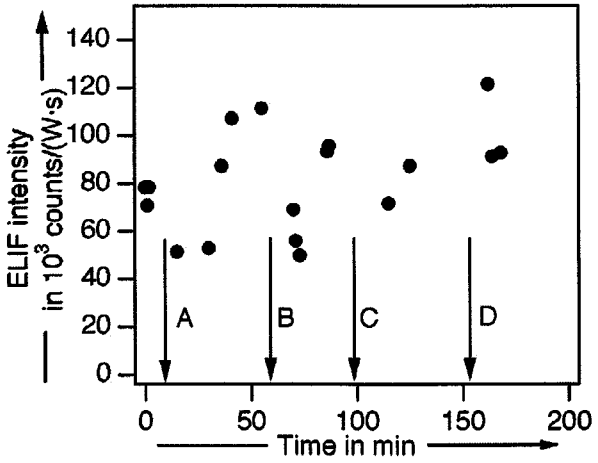

Figure 5-11. Time dependence of the NaOH ELIF signal as a function of burner gas mixture changes.

a) gas mixture was adjusted more fuel lean,

b) adjusted to normal,

c) adjusted rich, d) back to normal.

However, it is important to bear in mind that changing the stoichiometry in the way these tests were conducted simultaneously changes total gas flow into the tank, as well as flame geometry and temperature. A number of furnace characteristics will change on different time scales. For instance, if the mixture is made leaner by increasing the amount of oxygen, the gas will become cooler in a matter of seconds and the flow characteristics and volumes the burner puts across the melt will change. On a different time scale, perhaps minutes, the change in gas composition will affect the chemical equilibrium characteristics between the entire melt and the vapor. On a much longer time scale, the temperature of the melt will slowly adjust to the cooler furnace environment. Consequently, it is reasonable to expect to see both short-term and long-term changes to the NaOH ELIF signal as a function of what might appear to be a simple adjustment. Additionally, the measurements are complicated by the fact that at richer conditions the sodium atom concentration will increase, resulting in a greater reduction in the overall signal intensity due to the sodium atom radiation trapping process.

In light of the sparse data set in this initial series of tests, it clearly would have been valuable to have recorded more points and thus to have produced a continuous record. However, the present data do seem to represent some of these possible trends. Upon adjustment to leaner conditions, an immediate drop in the NaOH concentration is observed (dilution). On a longer timescale, the NaOH concentration increases (perhaps due to chemical equilibrium changes). Readjustment to a normal configuration results in a drop in signal followed by a recovery. Adjustment to richer condition, although still not sub-stoichiometric, also appears to produce an immediate drop again and then a recovery, but not to high levels. Adjustment back to normal from richer appears to result in a jump in signal followed by a downward trend back to the original signal levels. Note too, that the ELIF response at higher NaOH concentrations is not linear (see Figure 5-3). When the measurement corresponds to NaOH values in the range of hundreds of ppm range, a doubling of the ELIF signal represents a much greater change in the actual NaOH concentration.

Summary

This paper shows the application of a laser-based analytical technique for monitoring the NaOH content in a glass melt tank atmosphere. The method is based on Excimer Laser Induced Fragmentation fluorescence. The development of the method shows that the ELIF technique is abundantly sensitive to be used in actual industrial applications for monitoring the both NaOH and KOH in the tank atmosphere and exhaust. At this stage of development, however, precise quantitative measurements (e.g. ± 10%) have not been achieved. This is due to three factors primarily.

First, instrument calibration in the laboratory, as in the tube furnace, does not perfectly represent the fluctuating temperature or gas composition in the vicinity of a tank peephole or exhaust port. The uncertainty in carbon dioxide and water vapor concentration can be the source of these inaccuracies on the order of 30% of the signal. Second, inherent fluctuations in the tank itself lead to a variety of timescales and spatial scales within the melt tank. These fluctuations make it very difficult to translate the ELIF signal to an actual quantitative NaOH concentration based on a laboratory calibration. Third, this method can also simultaneously detect NaCl[8]. Although measurements during the course of this work indicate that interference from NaCl impurity is minimal, further work is required to quantify this effect.

Nevertheless, the results presented here show that a second-generation instrument has great promise. A more compact device can certainly be developed. With greater compactness and portability, multiple units could be easily calibrated against each other and for the specific characteristics of an assigned sample port by way of direct extractive sampling. These real time units could then be effective in reporting tank atmosphere fluctuations on a vastly finer time scale than the hours to days timescale of direct sampling.

Acknowledgements

The authors acknowledge the support of this project at various stages by the following individuals: Thomas Burns (U. of Missouri, Rolla); Greg Rolio, Vern Jensen, Robert Hernandez, Dave Girvan, Chris Kuppinger, John Conners, and Ray Mayer (PPG Industries Inc); Keith Kuhlengel and Dennis Morrison (Sandia National Laboratories).

References

[1] Monkhouse, P.: On-line diagnostic methods for metal species in industrial process gas. Prog. Energy Combust. Sci. **28** (2002) pp. 331-381.

[2] Rensberger Welland, K.J.; Wise, M.L.; Smith, G.P.: Laser-induced fluorescence detection strategies for sodium atoms and compounds in high-pressure combustors. Appl. Opt. **32** (1993) pp. 4066-4073.

[3] Hartinger, K.T.; Monkhouse, P.B.; Wolfrum, J.; Baumann, H.; Bonn, B.: Determination of flue gas alkali concentrations in fluidized-bed coal combustion by excimer-laser-induced fragmentation fluorescence. Proc. Combust. Inst. **25** (1994) pp. 193-199.

[4] Chadwick, B.L.; Domazetis, G.; Morrison, R.J.S.: Multiwavelength monitoring of photofragment fluorescence after 193 nm photolysis of NaCl and NaOH: Application to measuring the sodium species released from coal at high temperatures. Anal. Chem. **67** (1995) pp. 710-716.

[5] Greger, F.; Hartinger, K.T.; Monkhouse, P.B.; Wolfrum, J.; Baumann, H.; Bonn, B.: In situ concentration measurements in a pressurized, fluidized-bed coal combustor by excimer laser induced fragmentation fluorescence. Proc. Combust. Inst. **26** (1996) pp. 3301 –3307.

[6] Griffin, P.G.; Morrison, R.J.S.; Campisi, A.; Chadwick, B.L.: Apparatus for the detection and removal of vapor phase alkali species from coal-derived gases at high temperature and pressure. Rev. Sci. Instrum. **69** (1998) pp. 3674-3677.

[7] Gottwald U.; Monkhouse, P.: Single-port optical access for spectroscopic measurements in industrial flue gas ducts. Appl. Phys. B **69** (1999) pp. 151-154.

[8] Beerkens, R.G.C.; Kobayashi H.: Volitilisation and particulate formation in glass furnaces. Glastech Ber. Glass Sci. Technol. **68** C2 (1995) pp. 111-126.

[9] Jurcik B.; Philippe, L; Wayman, S; Ruiz R.: How oxy-fired glass furnaces reduce particulate emissions. Glass Industry (1997) May, pp. 14-23.

[10] Boillet J.; Paskocimas, C.A.; Leite, E.R.; Longo, E.; Varela, J.A.; Kobayashi, W.T.; Snyder, W.J.: The influence of oxy-fuel combustion atmosphere in glass furnaces on refractory corrosion. In: Pecoraro, G.A. et al. (eds.): Corrosion of materials by molten glass. Vol. 78 Westerville, OH: American Ceramic Society, 1996. pp. 217-237.

[11] Wu, K.T.; Kobayashi, H.: Three-dimensional modeling of alkali volatilization/ crown corrosion in oxy-fired glass furnaces. In: Pecoraro, G.A. et al. (eds.): Corrosion of materials by molten glass. Vol. 78 Westerville, OH: American Ceramic Society, 1996. pp. 205-216.

[12] Slade, S.J.: Glass furnace waste gas chemistry. In: Pecoraro, G.A. et al. (eds.): Corrosion of materials by molten glass. Vol. 78 Westerville, OH: American Ceramic Society, 1996. pp. 195-204.

[13] Faber, A.J.; de Heer, J.; Lankhorst, A.M.; Velthuis J.F.M.: Modeling of silica corrosion in the superstructure of oxy-fuel furnaces. In: Proc. International Congress on Glass. Annual Meeting, Amsterdam 2000. Westerville, OH: American Ceramic Society, 1998. (available on CD-ROM).

[14] Faber A.J.; Beerkens, R.G.C .; Reduction of refractory corrosion in oxy-fuel glass furnaces. In: Proc. XVIII International Congress on Glass, San Francisco, CA 1998, Westerville, OH: American Ceramic Society, 1998. (available on CD-ROM)

[15] Faber, A.J.; Verheijen O.S.: Refractory corrosion under oxy-fuel firing conditions. Ceram. Eng. Sci. Proc. **18** (1997) pp. 109-119.

[16] Nilson, R.H.; Griffiths, S.K.; Yang, N.; Walsh, P.M.; Allendorf, M.D.; Bugeat, B.; Marin, O.; Spear, K.E.; Pecoraro, G.: Analytical models for high-temperature corrosion of silica refractories in glass-melting furnaces. Glass Sci. Technol. **76** (2003) pp. 136-151.

[17] Allendorf, M.D.; Spear, K.E.: Thermodynamic analysis of silica refractory corrosion in glass-melting furnaces. J. Electrochem. Soc. **148** (2001) pp. B59-B57.

[18] Beerkens, R.G.C.; van Limpt, J.: Evaporation in industrial glass melt furnaces. Glastech. Ber. Glass Sci. Technol. **74** (2001) pp. 245-257.

[19] Blevins L.G.; Shaddix, C.R.; Sickafoose, S.M.; Walsh, P.M.: Laser-induced breakdown spectroscopy at high temperatures in industrial boilers and furnaces. Appl. Opt. **42** (2003) pp. 6107-6118.

[20] Buckley, S.G.; Walsh, P.M.; Hahn, D.W. et al.: Measurements of sodium in an oxygen-natural gas-fired soda-lime glass melting furnace. Ceram. Eng. Sci. Proc. **21** (2000) pp. 183-205.

[21] Rice, S.F.; Hanush, R.G.: Absorptivity of carbon dioxide and molecular oxygen at 193 nm at high temperature up to 1600 °C. Appl. Spectrosc. **56** (2002) pp. 1621-1625.

[22] Chadwick, B.L.; Morrison; R.J.S.: Monte Carlo simulation of radiation trapping and quenching of photofragment fluorescence after 193 nm photolysis of NaCl. J. Chem. Soc. Faraday Trans. **91** (1995) pp. 1931-1934.

[23] Hartinger, K.T.; Nord, S.; Monkhouse, P.B.: Temperature- and pressure-dependent absorption coefficients for CO_2 and O_2 at 193 nm. Appl. Phys. B **70**, (2000) pp. 133-137.

[24] Velez, M.; Carroll, L.; Carmody, C.; Headrick, W.L.; Moore, R.E.; Oxy-fuel simulator glass tank melter. Environmental Issues and Waste Management Technologies in the Ceramic and Nuclear Industries VI, Ceramic Transactions, **119**, (2001) pp. 47-54.

APPENDIX A:

ABSORPTIVITY OF CO_2 AND O_2 AT 193 NM AT HIGH TEMPERATURES UP TO 1600 °C

Abstract

The absorptivity of CO_2 and O_2 at 193 nm must be accounted for develop a quantitative ELIF method for the detection of NaOH(gas) in glass melting furnaces. In this appendix we describe measurements of CO_2 and O_2 at 193 nm absorbtivity over the temperature range of 900–1600 °C. The data were collected in a flow-type tube furnace using an ArF excimer laser at the light source. CO_2 was mixed at 5% by volume in N_2 and O_2 was examined at 5% and 10%. The internal transmittance of a 1-meter externally heated absorption cell was measured. The results establish a value for the absorptivity, α, for CO_2 ranging as high as 2.35×10^{-19} cm^2/molecule at 1600 °C. For O_2, the absorptivity is 1.81×10^{-19} cm^2/molecule at 1600 °C. The results partially agree with those reported in the literature recently by others at 1000 °C and 193 nm and extend those data to higher temperatures, however, the agreement is far from exact. The results are inconsistent with the higher temperature, 1500–2500 °C, values inferred by others from indirect measurements for these two species.

Introduction

Many laser-based diagnostics of combustion systems are in use today, employing the entire optical spectrum from the ultraviolet to the infrared. The goal of most of these techniques is to obtain quantitative measurements of specific chemical species at temperature conditions typically ranging from 1000 °C to 1700 °C. Key applications include engine and combustor optimization diagnostics and thermal waste treatment monitoring. Many potentially sensitive techniques are based on 193 nm ArF laser excitation, but are limited by difficulties associated with either excitation or detection efficiencies near this wavelength at high temperature. A major source of these problems is the temperature dependent absorptivity of high concentrations molecular oxygen and carbon dioxide, which are always present to some degree in a combustion environment. For example, these species are major constituents of the gas phase in glass melting furnaces, for which Excimer Laser Induced Fragmentation Fluorescence (ELIF) is under consideration as an in-situ method to detect NaOH(gas) (see Chap. 5).

Recently, Joutsenoja et al.[1] have reported detailed measurements of the absorptivity of these two species up to 1700 K and at wavelengths as short as 200 nm. Hildenbrand et al.[2] present CO_2 absorptivities as a function of temperature and wavelength to 2300K and 200 nm based on the work of Jensen et al.[3] The experiments in Ref. 2 highlight the need for this type of quantitative information. The trend in these 200 nm data indicates that the absorptivities are likely to be even greater at 193 nm, as would be expected.

One potential spectroscopic method for detecting trace species in a combustion environment that has received considerable attention recently is Excimer Laser Induced Fragmentation Fluorescence (ELIF) or Laser Induced Atomization (LIA). It has been shown that this technique can be very sensitive for detecting metals in high temperature vapor environments[4,5] and, in particular, a number of authors have explored the use of this method to determine alkali concentrations in solid fuel combustors.[6-10] The general ELIF technical approach is to illuminate the vapor containing simple molecular metal-containing species, such as NaOH, NaCl, KOH, etc., with a 193 nm laser pulse from an ArF laser. The subsequent photodissociation produces a population of excited metal atoms which produce atomic emission lines that are easy to detect.

In our work, the need to better understand the absorptivity of these gases stems from the application of ELIF as a means to examine the details of gas composition in glass manufacturing furnaces. In this instance, the vapor temperature can range from 1000 °C to as high as 1700 °C and recent work[11] has shown the important role trace alkali vapor can play in the rate of degradation of the refractory material from which these furnaces are constructed. ELIF represents a potential diagnostic method to access the spatial and temporal concentration dynamics of key alkali species.

The groups exploring ELIF as a combustor diagnostic have identified a number of practical considerations that must be addressed to obtain quantitative species concentrations from the atomic fragment fluorescence, include fluorescence quenching,[12] radiation trapping,[13] and probe beam absorption.[14] This last issue, the depth of excimer laser penetration into the hot gases, becomes more important at the higher temperatures experienced in a glass furnace. Clearly, the development of this photodissociation effect into an analytical technique for in situ measurements in furnaces and combustors relies on the ability to determine the intensity of the probe beam at a particular point in the combustion environment. The work of Hartinger et al.[14] provides the most recent and thorough examination of the absorption of 193 nm light by O_2 and CO_2, but only up to 1000 °C. However, they report that both species exhibit marked temperature dependence in their absorptivity at this wavelength. The absorptivity of oxygen at ambient and elevated temperature at this wavelength has been well studied,[15-20] but other than these data in Ref. 14, no other direct measurements have been reported on CO_2 at 193 nm.

Koshi et al.[21] report effective absorptivity values for O_2 and CO_2 at 193 nm in very dilute mixtures measured indirectly behind shock waves fin a temperature range of 1200–2400 °C. They report that $\alpha = 9 \times 10^{-20}$ cm^2/molecule for O_2 at 1500 °C and $\alpha = 4 \times 10^{-20}$ cm^2/molecule for CO_2 at 1500 °C. These CO_2 data are the only available in this temperature range and 193 nm prior the results we report here. They report that the $\alpha(O_2)$ is less than that reported by Davidson et al.[18] who place $\alpha(O_2)$ at 2.0×10^{-19} cm^2/molecule at 1500 °C. An extrapolation of the values that Hartinger et al.[14] report at 1000 °C to higher temperature is not consistent with the data on either species in Ref. 21, being higher at a given temperature, but lower than the results for O_2 in Ref. 18. The results reported by Joutsenoja in Ref.1, when extrapolated to 193 nm from 200 nm generally appear to agree with Ref 14, given the uncertainty in such an extrapolation. This paper reports the absorptivity of CO_2 and O_2 up to 1600 °C. Primarily, the results are intended to address the discrepancy between the 400–1000 °C data from Refs. 14, as well as the data in References 1 and 18 with the high temperature shock tube data of Ref. 21.

Experimental Method

Transmittance measurements of CO_2 and O_2 were conducted in a high temperature tube furnace designed to have a slow flow of a variety of gas mixtures. The apparatus is illustrated in Figure A-1. A 1600 °C (maximum) tube furnace (Carbolite STF) equipped with a 5 cm diameter alumina sample tube and capped with synthetic fused silica windows in Teflon holders, functions as the spectroscopic cell. The windows are 0.63 cm (0.25 in nominal) thick. The total cell length is 103 cm. The furnace consists of six SiC heaters that radiatively heat the sample tube. Each end of the tube is outside the heated region and there is a 10 cm length of alumina insulation within the furnace that is exposed to the radiative heaters, but prevents direct radiative transfer from the SiC rods to the sample tube. Gases are mixed at ambient temperature and are injected into the tube at one end and leave the tube at the other end, drawn out by the draft ventilation. The total flow rate in the tube is typically 3000 std cc/min yielding a flow pattern that is laminar with over the temperature range explored here. However, the large thermal gradients at the inlet and outlet of the furnace will disturb these flow conditions, enhancing the radial mixing of the gas. The average flow velocity ranges from 2.5 cm/s at the relatively cool injector to 15 cm/s in the center of the furnace. The laminar flow centerline velocity is as high a 30 cm/s.

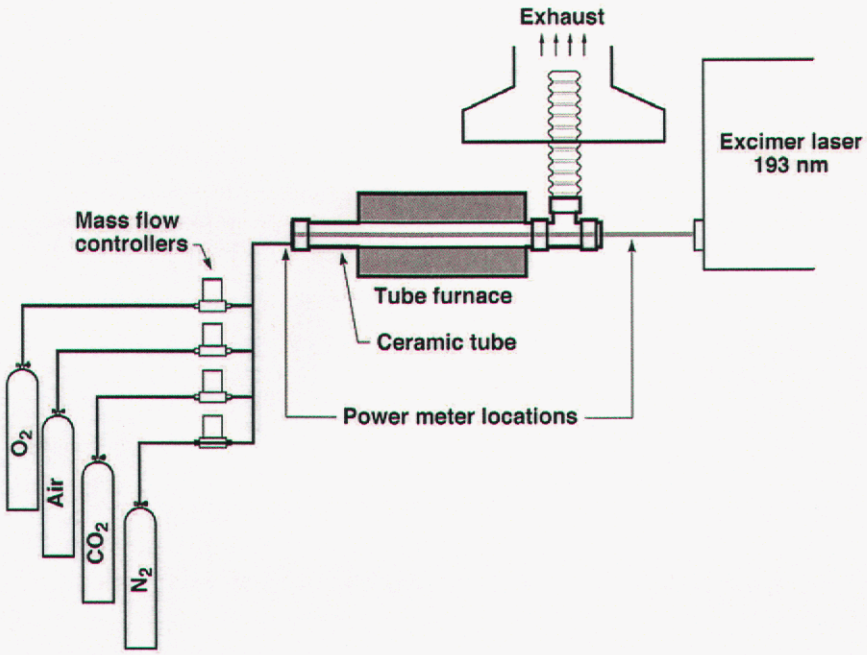

Figure A-1. Schematic of the high-temperature flow cell apparatus used to measure the absorptivity of O_2 and CO_2 or T≤ 1600 °C.

Axial temperature profiles at experimental conditions within the furnace were measured using an exposed 0.38 mm (0.015 in) Type "B" thermocouple that could be moved to any point along the centerline of the tube by way of an adaptor on the gas inlet end of the tube. The wire leads were confined within separate holes running the length of a two-holed alumina rod. The bare thermocouple junction was exposed with a length of wire of approximately 0.4 cm. Temperatures were measured on the tube wall and on the centerline. Temperatures were also measured on the centerline using a 0.075 mm (0.003 in) bead Type R thermocouple.

The measured centerline gas temperatures were corrected for radiation effects using the method outlined by Shaddix.[22] In this calculation, the emissivity of the Pt- Pt/Rh thermocouples ranged from 0.15 at 1000 °C and below to 0.19 at 1500 °C, following Ref. 1. In general, corrections were less than 100 °C for the large thermocouple and less than 20 °C for the small one. The corrected values for the two measurements are in good agreement, producing values for the true gas temperature within 20 °C of each other.

Figure A-2 shows a subset of the series of curves that relate the temperature profiles within the furnace to the nominal furnace temperature set point. The figure shows the measured temperature at the wall and the corrected temperature on the centerline of the tube. The wall temperature at a given position is used as the temperature of the radiative environment for the corrections to the measured gas temperatures. Axial profiles were recorded every 100 °C from 900 °C to 1600 °C. The temperature was measured at 2 cm intervals along the entire length of the tube with the probe being inserted from the downstream end to minimize disturbance on the flow due to the probe.

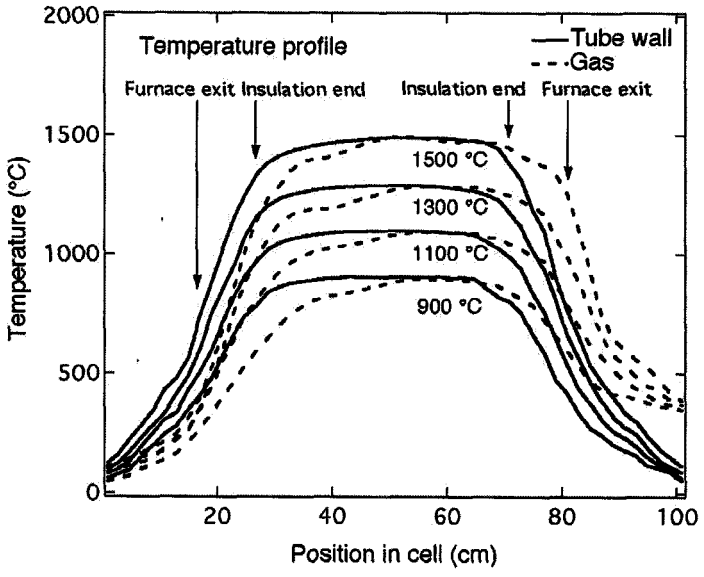

Figure A-2. Temperature profiles within the tube furnace of the tube wall (solid line) measured directly by a thermocouple and the gas temperature (dashed line) at the center of the tube corrected for radiation effects.

The internal transmittance measurements consist of several sets of data recorded in identical fashion. A 193 nm ArF laser (GAM Laser model EX10), operating at a nominal pulse energy of 12 mJ/pulse at 100 Hz and 0.5-nm line width, served as the source of the UV light. The beam was not focused and has an approximate cross section 3 x 8 mm. The average input power was measured using a factory-calibrated pulsed-laser power meter (Coherent Fieldmaster GS) placed 4 cm in front of the input window. To measure transmittance, the same meter was moved to a position 1 cm outside of the exit window. The gas mixtures examined were pure N_2, 5% CO_2 in N_2, and 5% and 10% O_2 in N_2. The fractional composition of the gas was determined by volumetric flow rate in the gas manifold measured by mass flow meters (Brooks Model 5850).

As both O_2 and CO_2 are known to dissociate upon excitation at 193 nm, some of the transmittance measurements were repeated with a laser pulse energy of 6 mJ/pulse and the laser pulse repetition rate was varied from 20 to 300 Hz. Changes in the internal transmittance are small relative to the overall experimental accuracy and do not appear to be systematic. If photolysis products contribute to the overall absorptivity at these conditions, a significant variation in the measurements as a function of these two parameters would be expected.

Results and Discussion

Figure A-3a presents a plot of the transmitted intensity of a 0.05 volume fraction mixture of CO_2 in N_2 as well as a curve representing the pure N_2 reference as a function of nominal setpoint temperature, Θ, in the flow furnace. Figure A-3b shows similar data for O_2 at both 0.05 and 0.10 volume fraction. The incident intensity of the 193-nm light is attenuated by the 4 cm of air in front of the window and reflection losses at the input and exit windows. We have measured these properties of our system directly. The attenuation by ambient air is <1%, the reflection losses at the uncoated fused silica window is 4.7% at each surface, and the absorption is about 6%, but appears to be temperature dependent. Thus, the transmittance of the apparatus at ambient temperature is 62.8% when filled with nitrogen and is represented by the data at ambient temperature in nitrogen in Figure A-3. As the input and exit windows can reach temperatures as high as 200 °C, the reduction in transmission of the reference N_2 sample, shown if Figure A-3, originates from the temperature dependence of the window reflection and absorption characteristics. For the analysis described below, the input and exit intensities are corrected for these losses.

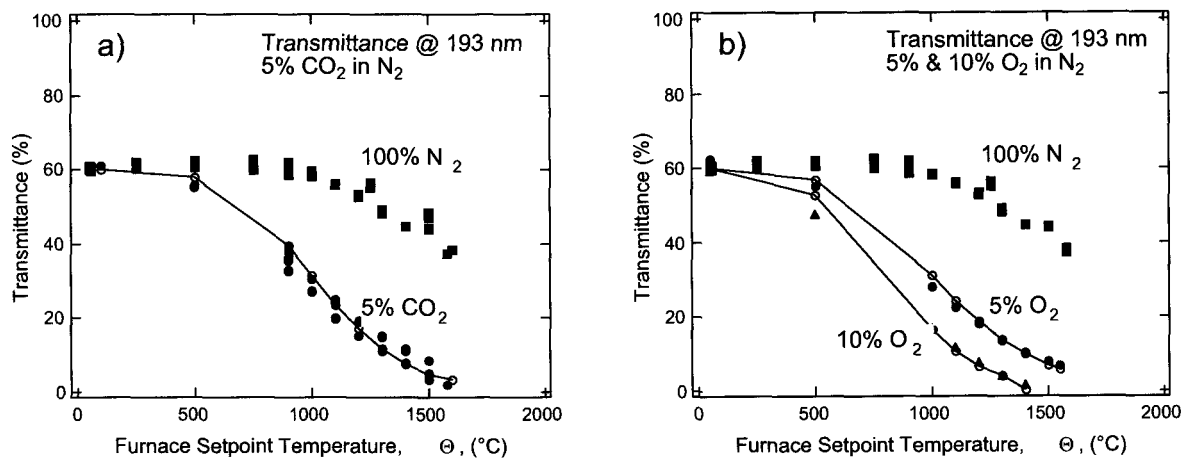

Figure A-3. a) Measured and fitted results for CO_2 transmittance in the high temperature cell vs. b) furnace setpoint temperature, Θ. Pure N_2: solid squares, 5% CO_2 in N_2: solid circles, results from fitted parameters from Table A-1: open circles/line. b) Measured and fitted results for O_2 transmittance in the high temperature cell vs. furnace setpoint temperature, Θ. Pure N_2: solid squares, 5% O_2 in N_2:solid circles, 10% O_2 in N_2:solid triangles; results from fitted parameters from Table A-1: open circles/line.

The data in Figure A-3 represent the transmission of the 193-nm light through the temperature profiles shown in Figure A-2 with temperatures on the abscissa being the nominal setpoint values of the furnace. Scatter in the data originates mostly from the precision of the mass flow meters. The error in these raw data carries over to the standard deviations reported for the fitted absorptivity parameters.

The raw transmission data are the result of the combination of the gas mixture absorptivity, which varies with temperature across the temperature profile, and the density profile within the furnace. Hartinger et al.[14] have suggested that the absorptivity for both O_2 and CO_2 follow an exponential functional form in temperature, at least up to 1000 °C. This is not surprising as the 193-nm absorption originates from thermal population of excited vibrational levels. Thus, for each molecule, if a parameterized exponential functional form for the absorptivity is assumed, the transmittance data in Figure A-3 can be fitted to the direct numerical integration of

$$dI_t(z) = - I_t(z)\alpha(T_\Theta(z))\rho(T_\Theta(z))dz \qquad \text{(A-1)}$$

where $I_t(z=0)$ is the input intensity after correction for the input losses at the window, $T_\Theta(z)$ is represented by the gas temperature curves in Figure A-2 for a given furnace setpoint temperature Θ, z is the axial position within the tube/cell, and α is the molecular absorptivity. The measured transmittance is $I_t(z = 103$ cm) corrected for the exit window losses. The function, $\rho(T_\Theta(z))$ is taken as the density of an ideal gas, $P/\mathrm{R}\ T_\Theta(z)$. The molecular absorptivity at a given point in the furnace is represented by

$$\alpha(T_\Theta(z)) = \alpha_o \exp(-\varepsilon/T_\Theta(z)) \qquad \text{(A-2)}$$

where ε, and α_o are fitting parameters, having no physical meaning themselves. The parameters, ε and α_o, are determined for both CO_2 and O_2 by a non-linear least squares fitting process to the transmittance measurements for each species recorded at the different values of Θ. The data is fitted to minimize the variance of the logarithm of the measured transmittance. This functional form best provides equal weighting of the individual temperature points in determining α_o and ε. The results to the fits are listed in Table A-1. Figure A-3a and A-3b show the results of the fits by plotting the calculated absorptivity curves from the fitted parameters along with the raw transmittance data.

Table A-1. Fitted parameters for absorptivity, $\alpha(T) = \alpha_o \exp(-\varepsilon/T)$ (cm^2/mol)

	ε(K)	$\sigma(\varepsilon)^a$	α_o (cm^2/molecule)	$\sigma(\alpha_o)^a$
CO_2	6327	429	6.89×10^{-18}	1.92×10^{-18}
O_2	5475	270	3.37×10^{-18}	0.63×10^{-18}

(a) – 1σ error from fit

It is well known that O_2 absorbs appreciably at 193 nm, even at ambient temperatures, and has an absorption coefficient that exhibits a direct dependence on the product of pressure and pathlength, *Pz*, such that the Beer-Lambert Law is not followed. Lee and Hanson[17] illustrate that the effect of elevated temperature is insufficient to smooth out the spectral structure within the 0.5 nm ArF laser bandwidth and thus, the absorptivity is not independent of the product of the pressure and pathlength over the range of temperature examined here. This is due to the complicated nature of the spectrum consisting of overlapping features of discrete predissociated transitions with individual linewidths much sharper than the laser line. In contrast to O_2, the absorption spectrum of CO_2 is diffuse and therefore the absorptivity is independent of *Pz*.[14] However, for the 5% measurements, the value of *Pz* is small. With the partial pressure of O_2 only 0.05 bar, and the effective high-temperature region, which contributes to the bulk of the absorption, only about 40 cm (see Figure A-2), the resulting *Pz* is near 2 bar-cm. Examination of the *Pz* dependence in Ref. 14 shows that the precision of data reported here cannot distinguish between a value of 2 and a value of zero for *Pz*. According to the results in Ref. 14, we would expect to see an effect on the absorptivity at the 0.10 bar partial pressure. Here, however, the same absorptivity values reproduce the data in the measurement at both concentrations.

The functions $\alpha(T)$ for CO_2 and O_2 are plotted in Figures A-4 and A-5 respectively. The results are compared with those reported by Hartinger et al.[14] in the relatively simple case of CO_2 using Eq. A-5 in that paper for k and converting to α through the relationship $\alpha = kRT$ and $R = 1.38 \times 10^{-22}$ bar-cm^3/molec-K. In the case of O_2, we have used their $Pz = 0$ equation (Eq. A-6) for comparison, similarly.

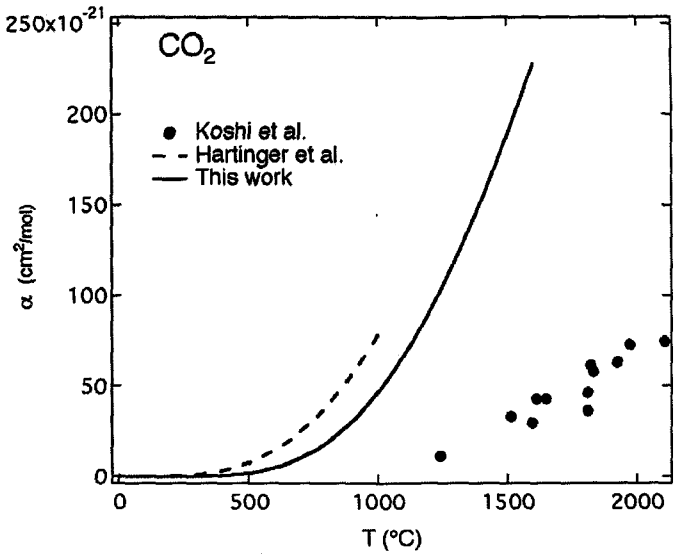

Figure A-4. Absorptivity of CO_2 determined from the data in Figure A-3 using the method described in the text and the parameters in Table A-1 (solid line). Included in the figure are the results reported by Hartinger et al.[14] (dashed line) and data take from Koshi et al.[21] (solid circles).

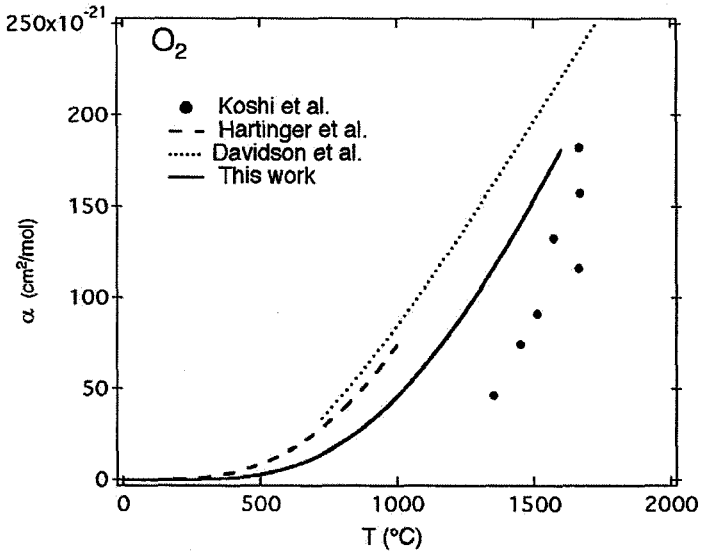

Figure A-5. Absorptivity for O_2 determined from the raw transmittance data using the method described in the text. Included in the figure are the results reported by Hartinger et al.[14] (dashed line) and data take from Koshi et al.[21] (solid circles). The dotted line is the function Davidson et al for k in atm^{-1}-cm^{-1} converted to α in cm^2/molecule.

The results presented in Figures A-4 and A-5 place the absorptivity of both O_2 and CO_2 at a value somewhat less that that reported by Hartinger et al.[14] at for the region of overlap. Extrapolation of the Ref. 14 CO_2 curve to higher temperature produces an offset between these two measurements of about 45 x 10^{-21} cm^2/molecule. The results in Ref. 1, extrapolated to 193 nm, yield approximately 250 x 10^{-21} at 1400 °C, which is greater than the formula in Ref. 14 would predict by nearly a factor of two. Thus, there remains some discrepancy among the various studies.

The situation for O_2 is similar. Again, the results presented here indicate an absorptivity that is somewhat lower than that observed and extrapolated in Ref. 14, which agrees well with Ref. 18. An extrapolation of the results in Ref. 1 to lower wavelength will produce an absorptivity that is nearly twice that reported in Ref. 14. The disagreement between these new results presented here and those in Ref. 1 is even greater.

Conclusion

Parameters for exponential-type functions that represent the absorptivity of CO_2 and O_2 at 193 nm from an ArF laser over the temperature range of 900-1600 °C are determined from transmittance measurements in a high temperature cell. The results indicate that the combined set of measurements on O_2 and CO_2 at 193 nm using this work and the data in Ref. 14 and Ref. 1 provide an evaluation of the absorptivity of these molecules at high temperature conditions, but the agreement among the data sets is not ideal. The new data indicate that the earlier reported values in Ref. 21 are too low, especially for CO_2. These new results contribute to the quantitative spectrometric knowledge of these two key combustion gases for the development of excimer laser-based probes of furnace environments.

References

[1] T. Joutsenoja, A. D'Anna, A. D'Alession and M.I. Nazzaro, Appl. Spectrosc. **55**, 130 (2001).

[2] F. Hildenbrand, C. Schultz, Appl. Phys. B **73**, 173 (2001).

[3] J.R. Jensen, R.D. Guettler, J.L Lyman, Chem. Phys. Lett. **277**, 356 (1997).

[4] S.G. Buckley, C.P. Koshland, R.F. Sawyer, D. Lucas, Proc. Comb. Inst. **26**, 2455 (1996).

[5] S.G. Buckley, C.S. McEnally, R.F. Sawyer, C.P. Koshland, D. Lucas, Combust. Sci. Technol. **118**, 168 (1996).

[6] K.J. Rensberger Welland, M.L. Wise, and G.P. Smith, Appl. Opt. **32**,4066 (1993).

[7] K.T. Hartinger, P.B. Monkhouse, J. Wolfrum, H. Baumann, and B. Bonn, Proc. Comb. Inst. **25**, 193 (1994).

[8] B.L. Chadwick, G. Domazetis, R. J.S. Morrison, Anal. Chem. **67**, 710 (1995)

[9] F. Greger, K.T. Hartinger, P.B. Monkhouse, J. Wolfrum, H. Baumann, and B. Bonn, Proc. Comb. Inst. **26**, 3301, (1996).

[10] P.G. Griffin, R.J.S. Morrison, A. Campisi, B.L. Chadwick, Rev. Sci. Instrum. **69**, 3674 (1998).

[11] M.D. Allendorf, K.E.Spear, J. Electrochem. Soc. **148**, B59 (2001).

[12] K.T. Hartinger, S. Nord, and P.B. Monkhouse, Appl. Phys. B, **64**, 363 (1997).

[13] B.L. Chadwick and R.J.S. Morrison, J. Chem Soc. Faraday Trans. **91**,1931 (1995).

[14] K.T. Hartinger, S. Nord, and P.B. Monkhouse, Appl. Phys. B **70**, 133 (2000).

[15] M. Ogawa, J. Chem. Phys. **54**, 2550 (1971).

[16] M.W.P. Cann, J.B. Shin, and R.W. Nichols, Can. J. Phys. **62**, 1738 (1984).

[17] M.P. Lee and R.K. Hanson, J.Quan. Spectrosc. Radiat. Transfer **36**, 425 (1986).

[18] D.F. Davidson, A.Y. Chang, K. Kohse-Höinghaus, and R.K. Hanson, J.Quan. Spectrosc. Radiat. Transfer **42**, 267 (1989).

[19] M. Shimauchi, T, Miura, and H. Takuma, Jpn. J. Appl. Phys. **33**,4628 (1994).

[20] J. Vattulainen, L. Wallenius, J. Stenberg, R. Hernberg, and V. Linna, Appl. Spectrosc. **15**, 1311 (1997).

[21] M. Koshi, M. Yoshimura, and H, Matsui, Chem. Phys. Lett. **176**, 519 (1991).

[22] C. R. Shaddix, Proceedings of the 33rd National Heat Transfer Conference FTD99-282 August 15-17, Albuquerque, NM (1999).

DISTRIBUTION LIST

External Distribution

R. G. C. Beerkens
TNO TPD
P.O. Box 595
5600 AN Eindhoven
The Netherlands

Dr. John T. Brown
GMIC
455 West Third Street
Corning, NY 14830

Dr. M. Usman Ghani
American Air Liquide
Chicago Research Center
5230 S. East Avenue
Countryside, IL 60525

Michael A. Greenman
Glass Manufacturing Industry Council
735 Ceramic Place
Westerville, OH 43081

Mr. Amul Gupta
Monofrax Inc.
501 New York Avenue
Falconer, NY 14733-1797

Mr. William Horan
Techneglas
66 Old Boston Road
Pittston, PA 18640

Dr. Hisashi Kobayshi
Praxair, Inc.
Applications and Research Dept.
777 Old Saw Mill River Road
Tarrytown, NY 10591-6799

Elliot P. Levine
EE-2F, Industrial Technologies Program
Department of Energy
1000 Independence Ave SW
Washington DC 20585

John Neufeld
Gallo Glass Co.
P. O. Box 1230
Modesto, CA 95353

Dr. Dilip Patel
North American Refractories Co.
8361 Broadwell Road, P.O. Box 44040
Cincinnati, OH 45244

Dr. George A. Pecoraro
429 Dakota Drive
Lower Burrell, PA 15068

Dr. Pavol Pranda
American Air Liquide
Chicago Research Center
5230 S. East Avenue
Countryside, IL 60525

Dr. Greg Prusia
BOC Gases
1720 Indian Wood Circle, Bldg. E
Maumee, OH 43537

James A. Shell
Shell Glass Consulting, Inc.
77 Saint Martin Court
Gahanna, OH 43230-3122

John Sopko
Glass Technology Center
PPG Inc.
P.O. Box 11472
Harmar Township, PA 15238-0472

Prof. Karl Spear
44 Tidnish Head Road
Amherst, Nova Scotia B4H 3X9

Dr. Peter Troell
ANH Refractories
600 Grant Street
Pittsburgh, PA 15219

Prof. Mariano Velez
MO-SCi Corporation
4000 Enterprise Dr.
Rolla, MO 65402-0002

Prof. Peter Walsh
University of Alabama at Birmingham
BEC 257
1530 3rd Avenue South
Birmingham, AL 35294

Edward Wolfe
ANH Refractories
600 Grant Street
Pittsburgh, PA 15219

Internal Distribution

5	MS 9953	M. D. Allendorf
2	MS 9052	S. F. Rice
3	MS 9018	Central Technical Files, 8945-1
1	MS 0899	Technical Library, 9616
1	MS 9021	Classification Office, 8511 for Technical Library, MS 0899, 9616 DOE/OSTI via URL